UNIVERSITY OF CALIFORNIA, SAN DIEGO

Properties of Heterogeneous Energetic Materials under High Strain, High Strain Rate Deformation

A dissertation submitted in partial satisfaction of the

requirements for the degree Doctor of Philosophy

in

Materials Science and Engineering

by

Jing Cai

Committee in charge:

Professor Vitali F. Nesterenko, Chair
Professor David J. Benson
Professor Yu-Hwa Lo
Professor Vlado A. Lubarda
Professor Marc A. Meyers

2007

The dissertation of Jing Cai is approved, and it is acceptable in quality and form for publication on microfilm:

_____

_____

_____

_____

_____

Chair

University of California, San Diego

2007

TABLE OF CONTENTS

LIST OF FIGURES

LIST OF TABLES

ACKNOWLEDGEMENT

This work would not have been possible without the continuous guidance of Dr. Vitali F. Nesterenko. I sincerely appreciate his constant support and help on the research in the past five years. His attitude towards science, being enthusiastic, curious, and careful, has deeply influenced mine. I also would like to thank the members of my dissertation committee, Dr. Marc A. Meyers, Dr. David J. Benson, Dr. Prabhakar Bandaru, and Dr. Yu-Hwa Lo, for their comments and suggestions. I am especially indebted to Dr. Marc A. Meyers, not only for use of his laboratory equipment, materials, and facilities, but also for his genius input on the subject and inspiration on the research.

Special thanks would be given to the former colleague, Dr. Yabei Gu, for his training and advice at the beginning of the research, and the colleague, Eric Herbold, for his discussion and numerical modeling on a part of the research. I also would like to express my appreciation to Dr. Kenneth Vecchio and Dr. Fengchun Jiang for providing data on a part of Hopkinson bar tests of my samples, Dr. Yuejian (Eugene) Chen for bringing me an opportunity to work on the Carbon Fibers Filled Al Alloy project and corresponding suggestions, Dr. Anuj Mishra for help in quasi-static and ECAP tests, Yasuaki Seki and Albert Yu-Min Lin for help in quasi-static tests, Ryan Anderson in CalIT2 and Evelyn York in Scripps Institute of Oceanography for SEM training and micrographs-taking, and Ralf Brunner for Raman spectroscopy analysis. A special acknowledgement is extended to the fellow Materials Science and Engineering Program graduate students for encouragement and company.

Finally, my sincere gratitude goes to my parents, my sisters and their families, and my friends who have always been with me and extremely supportive of my work.

Funding for the research was provided by ONR under Contract No. N00014-02-1-0491, N00014-06-1-0263, and MURI ONR N00014-07-1-0740.

Chapter 4 incorporates results from the following publications: (1) “Effect of Strain Rate on the Mechanical Properties of Aluminum Alloy Matrix Composite Filled with Discontinuous Carbon Fibers”, Jing Cai, Yuejian Chen, Vitali F. Nesterenko, Marc A. Meyers, Materials Science and Engineering A, submitted.; (2) “High-Strain, High-Strain-Rate Flow and Failure in PTFE/Al/W Granular Composites”, Jing Cai, Steve M. Walley, Richard J.A. Hunt, William G. Proud, Vitali F. Nesterenko, Marc A. Meyers, Materials Science and Engineering A, in press; (3) “Collapse of Hollow Cylinders of PTFE and Aluminum Particles Mixtures Using Hopkinson Bar”, Jing Cai, Vitali F. Nesterenko, Proceedings of the Conference of the American Physical Society Topical Group on Shock Compression of Condensed Matter-2005, 2006, 793-796; (4) “Shear Localization and Patterning of Shear Bands In PTFE and Its Mixtures with Metals”, Yabei Gu, Vitali F. Nesterenko, Jing Cai, Proceedings of the Conference of the American Physical Society Topical Group on Shock Compression of Condensed Matter-2003, 2004, 775-778. The dissertation author was the primary investigator and author of these papers.

VITA

1999	Bachelor of Engineering, Metal Forming University of Science and Technology Beijing, Beijing, China
2004	Master of Engineering, Materials Science and Engineering University of California San Diego, San Diego, USA
2007	Doctor of Philosophy, Materials Science and Engineering University of California San Diego, San Diego, USA

PUBLICATIONS

Jing Cai, Eric B. Herbold, David J. Benson, Vitali F. Nesterenko, "The influence of particle size on the mechanical properties of PTFE-Al-W composite materials", Applied Physics Letter, in preparation.

Jing Cai, Yuejian Chen, Vitali F. Nesterenko, Marc A. Meyers, "Effect of Strain Rate on the Mechanical Properties of Aluminum Alloy Matrix Composite Filled with Discontinuous Carbon Fibers", Materials Science and Engineering A, accepted.

Jing Cai, Fengchun Jiang, Kenneth Vecchio, Marc Meyers, Vitali Nesterenko, "Mechanical and Microstructural Properties of PTFE/Al/W System", Proceedings of the Conference of the American Physical Society Topical Group on Shock Compression of Condensed Matter-2007, submitted.

Eric B. Herbold, Jing Cai, David Benson,Vitali Nesterenko, "Simulation of Particle Size Effect on Dynamic Properties and Fracture of PTFE-W-Al Composites", Proceedings of the Conference of the American Physical Society Topical Group on Shock Compression of Condensed Matter-2007, submitted.

John Addiss, Jing Cai, Steve Walley, William Proud, Vitali Nesterenko, "High Strain, Strain Rate Behavior of PTFE/Al/W", Proceedings of the Conference of the American Physical Society Topical Group on Shock Compression of Condensed Matter-2007, submitted.

Jing Cai, Steve M. Walley, Richard J.A. Hunt, WillamG. Proud, Vitali F. Nesterenko, M.A. Meyers, "High-Strain, High-Strain-Rate Flow and Failure in PTFE/Al/W Granular Composites", Materials Science and Engineering A, in press.

Jing Cai, Vitali F. Nesterenko, “Collapse of Hollow Cylinders of PTFE and Aluminum Particles Mixtures Using Hopkinson Bar”, Proceedings of the Conference of the American Physical Society Topical Group on Shock Compression of Condensed Matter-2005, 2006, 793-796

Paul Gefken, Donald Curran, Vitali F. Nesterenko, Jing Cai, “The Explosive Spherical Cavity Expansion for Characterization of SiC-N Ceramic Dynamic Behavior and Post Shock Damage Using RUS Method”, Proceedings of the Conference of the American Physical Society Topical Group on Shock Compression of Condensed Matter-2005, 2006, 619-622.

Yabei Gu, Vitali F. Nesterenko, Jing Cai, “Shear Localization and Patterning of Shear Bands In PTFE and Its Mixtures with Metals”, Proceedings of the Conference of the American Physical Society Topical Group on Shock Compression of Condensed Matter-2003, 2004, 775-778.

CONFERENCE PRESENTATIONS

Jing Cai, Fengchun Jiang, Kenneth S. Vecchio, Marc A. Meyers, Vitali F. Nesterenko, “Mechanical and Microstructural Properties of PTFE/Al/W Composite”, 15th American Physical Society Topical Conference on Shock Compression of Condensed Matter, June 24-29, 2007, Kohala Coast, Hawaii

Marc A. Meyers, Vitali F. Nesterenko, Jing Cai, Steve M. Walley, William G. Proud, Richard J. A. Hunt. “High Strain, High Strain Rate Flow and Failure in PTFE/Al/W Granular Composites”, 2007 Society of Experimental Mechanics Annual Conference & Exposition, June 3-6, 2007, Springfield, Massachusetts

Jing Cai, Fengchun Jiang, Eric B. Herbold, John Addis, Steve M. Walley, William G. Proud, Kenneth S. Vecchio, David J. Benson, Vitali F. Nesterenko, “An Analysis of Mechanical and Microstructural Properties of PTFE-Al-W System”, 2007 Society of Experimental Mechanics Annual Conference & Exposition, June 3-6, 2007, Springfield, Massachusetts

Jing Cai, Eugene Chen, Vitali F. Nesterenko, Marc A. Meyers, “Carbon Fiber on the Mechanical Properties of Aluminum Matrix Composite”, 2007 Society of Experimental Mechanics Annual Conference & Exposition, June 3-6, 2007, Springfield, Massachusetts

Jing Cai, Vitali F. Nesterenko, “Collapse of Hollow Cylinders of PTFE and Aluminum Particles Mixtures Using Hopkinson Bar”, 14th American Physical Society Topical Conference on Shock Compression of Condensed Matter, July 31–August 5 2005; Baltimore, Maryland

Fields of Study

Major field: Engineering (Materials Science)

ABSTRACT OF THE DISSERTATION

Properties of Heterogeneous Energetic Materials
under High Strain, High Strain Rate Deformation

by

Jing Cai

Doctor of Philosophy in Materials Science and Engineering

University of California, San Diego, 2007

Professor Vitali F. Nesterenko, Chair

Heterogeneous energetic materials have many applications. Their dynamic behavior and microstructural evolution upon plastic deformation have remained not fully understood. The following heterogeneous materials were investigated in the this study: the pure PTFE (usually a mixture of crystalline and amorphous phases), PTFE-Sn, PTFE-Al, PTFE-Al-W, and carbon fibers filled Al alloy.

Sample manufacturing processes involving ball milling and Cold Isostatic Pressing were employed. Quasi-static and Hopkinson bar tests were carried out to obtain the compressive strengths of composites. The Conventional Thick-walled Cylinder

(TWC) method and newly developed small-scale Hopkinson bar based TWC experiments were conducted to investigate single shear bands and their assembly. Conventional and "soft" drop-weight tests were performed to examine the mechanical properties and the initiation of chemical reactions. Scanning Electron Microscopy was used to detect the details of the microstructures and failure mechanisms of heterogeneous materials.

New features in the dynamic behavior of heterogeneous materials were observed. They include the following:

- Strain softening, instead of thermal softening, is the main mechanism in the initiation of shear bands in explosively driven TWC tests of solid PTFE.
- Cold isostatically pressed PTFE-Sn samples were more stable with respect to shear localization than solid PTFE.
- The dynamic collapse of solid PTFE-Al samples with different particle sizes was accomplished with the shear localization bands and cracks.
- Force chains in the fine W and Al particles were attributed to the high strength of the porous PTFE-Al-W composite containing fine W particles in comparison with composites with coarse W particles.
- Debonding of metal particles from the PTFE matrix and the fracture of the matrix were identified to be two major mechanisms for the failure of the PTFE-Al-W composites.
- The formation of PTFE nano-fibers during high strain flow was detected.
- The orientation of carbon fibers did not influence the strength and reaction of carbon fibers filled Al alloys, but the strength of carbon fibers did.

CHAPTER 1

INTRODUCTION

Energetic materials have been intensively studied from the safety and performance viewpoints depending on the mechanical, physical, chemical and thermodynamical properties. Energetic materials are generally referred to as materials that exhibit a dramatic release of the stored chemical energy. The primary difference between an energetic material and any material that undergoes a chemical decomposition process is the rate at which the decomposition occurs. For explosives, the rate and amount of energy released is normally sufficient to establish a self-sustaining shock driving chemical reactions. Heterogeneous energetic materials have recently gained popularity thanks to the excellent combination of properties from a mixture of materials. Nevertheless, the complexity of a mixture presents a challenging task to understand not only the individual constituent's contribution to the performance but also the influence of interaction between them on the overall properties and performance of a composite system.

Among numerous heterogeneous energetic materials, the mixtures of metals and a polymer [1,2] represent one category, in which the reactions between constituents are expected upon impact under specific conditions. Polytetrafluoroethylene (PTFE) is one of main candidates among all polymers to be employed. It has many desirable properties:

a low friction coefficient, high thermal stability, high electrical resistance, high chemical inertness, high melting point, high melt viscosity, high thermal energy release when decomposed, and is easily deformable [3]. In this research, the dynamic behavior of the mixtures of PTFE powder and Sn powder, of PTFE powder and Al powder, and of PTFE powder and Al powder and W powder are investigated.

Aluminum is one of most studied materials on the earth. It is also widely used in daily life, medical appliances, all fields of engineering, and defense applications. It possesses a superior combination of many excellent properties: as the third most abundant element, it is widely available; it has a high strength-to-weight ratio, a important characteristic for the weight-sensitive applications; its low melting point (660C) makes it easily participate in chemical reactions; when reacting with other chemical components, it would release a high amount of heat to assist the reaction propagating without external aids. Thanks to these excellent properties, Al alloys and Al composites are of great interest. In this research, the carbon fiber filled Al alloys are investigated to understand the influences of the type and orientation of fibers on the mechanical properties and chemical reactions of the Al alloy and Al composites.

Chapter 2 contains the literature reviews on polymeric composites, thermites, and the energy release of energetic materials. The focuses are on the influence of filler size on the strengths of the polymeric composites consisting of a polymer matrix and fillers, the dynamic behavior and general applications of thermites, and the chemical reactions of energetic materials at high speed impact. This background knowledge is related to different aspects of my research.

Chapter 3 presents the introduction of experimental techniques applied in the research. Ball milling was employed to break down the agglomeration of powder particles before they were pressured into solids. To prepare high-density high-accurate-dimension samples, Cold Isostatic Pressing (CIPing) was used. Quasi-static compression tests were carried out to understand the samples' strain-rate sensitivity and acquire samples' response to low-strain-rate deformation, while high-strain-rate deformation of samples were investigated by Hopkinson bar and drop-weight tests. Equal Channel Angular Pressing (ECAP) was conducted to examine the samples' microstructural response to high-shear-strain deformation. Thick-walled Cylindrical (TWC) tests were carried out to observe the formation of shear bands, which could be the major contributor to the initiation of chemical reactions in the materials. Scanning Electron Microscopy (SEM) was employed to observe the microstructural evolution of samples before and after deformation. Raman Spectroscopy was employed to recognize the products of chemical reactions.

The experiment results and discussion are given in Chapter 4. The testing of the PTFE-Sn composites revealed that cylindrically symmetrical collapse of samples in the Hopkinson bar based TWC test resulted in high-strain-rate plane-strain (pure shear) deformation with negligible axial strain and the samples were more stable with respect to shear localization than solid PTFE. The choice of glycerol liquid in the Hopkinson bar based TWC test boosted the deformation of the PTFE-Al composite samples into totally collapsed and shattered condition with preservation of cylindrical symmetry. The 2-μm Al particles in the composites led the reaction occurring inside the shear zone or on the sliding sides of cracks during collapse of hollow cylindrical samples. The small size of W

particles in the PTFE-Al-W composites increased the strength of the composites. The phenomenon that the porous PTFE-Al-W samples containing fine W particles had a higher strength of the densified PTFE-Al-W samples containing coarse W particles is explained by the formation of force chains among fine W particles. The local adiabatic heating in the PTFE-Al-W samples generated PTFE nano-fibers which influenced the crack propagation. The stronger carbon fibers led to the stronger carbon-fiber-filled Al-Mg alloy, but the orientation of carbon fibers (placed along or perpendicular to loading direction) did not make significant different on the strength of the C/Al-Mg composites.

Finally, Chapter 5 briefly outlines the summary of this research.

CHAPTER 2

BACKGROUND

It is a complicated task to analyze the dynamic behavior of composite materials. The strain-rate response of a composite depends on that of the matrix, the fillers and interface between them. The failure mechanism of a composite relies on the volume fraction and the geometry (size, configuration, and orientation) of the filler, on the type of the matrix (rigid, brittle, elastic, or viscoplastic), and on the mechanism of force transfer between the matrix and the filler. The most common failure mechanisms (energy absorption modes) include matrix failure (matrix shear failure, matrix cracking, and matrix buckling), filler pull-out, filler/matrix debonding, and delamination [4-6]. For example, Figure 2.1 shows a schematic diagram of the energy level related to various parameters (impact velocity, failure modes) of a ballistic test of a composite consisting of woven glass fibers and a epoxy matrix. It can be observed that when the energy level was low, fiber fracture, matrix cracking, and debonding of the filler from the matrix dominate in the failure of the composite. High energy level could change the failure mechanism of the composite to delamination. So, it can be concluded that under a curtain circumstance (depending on the available amount of energy), one failure mechanism may dominate in the failure of a composite.

Section 2.1 reviews the literature with regards to the influence of filler size on the strengths of the polymeric composites. Section 2.2 introduces the dynamic behavior and general applications of thermites, a class of materials which may release huge amount of heat when reacted. Section 2.3 briefly outlines the chemical reaction and important parameters of reaction of energetic materials at high velocity impact, especially the metal/PTFE compounds. All these background knowledge is related to different aspects of the research.

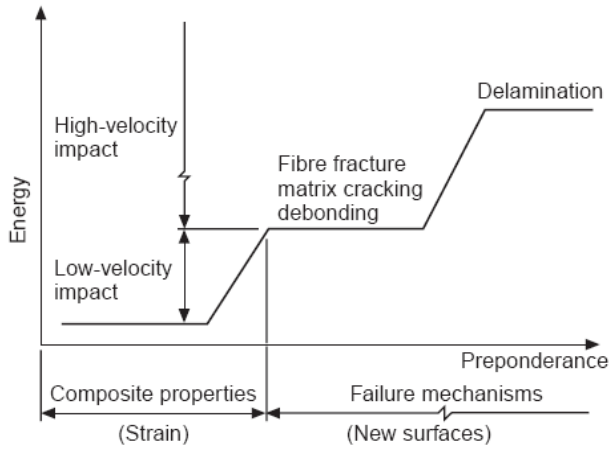

Figure 2.1. Schematic showing the tendency of composite energy behavior with composite and projectile parameters, and with the failure mechanisms [7].

In summery, this chapter outlines the theories and knowledge of heterogeneous energetic materials and helps the author delve deeply into the subject of the current research.

2.1 Influence of Fillers on the Strength of Polymeric Composites

The inclusion of fillers, such as glass beads, glass fibers, silica particles and metal particles, in a polymeric system is widely studied and used in medical applications [8-10], the integrated circuits industry [11,12], and the defense industry [13,14]. Their inflence on density, strength and thermal stability makes these materials desirable. Many studies have focused on the influence of fillers on physical and mechanical properties of composites, such as tensile and compressive strengths, wear resistance, and water absorption. For the most part, these investigations have been concerned with the effects of filler content, size, shape, distribution, aspect ratio, and treatment in a solid composite.

The interfacial adhesion has been known to have an important impact on the overall mechanical properties of polymeric composites. A silane coupling agent has been applied to the filler surface to improve filler-matrix adhesion in composites [15-17]. This approach has proved valid in improving composite properties [8] on flexural strength, flexural modulus, and shear strength. Rare-earth modifiers were studied [18] to determine the optimum amount and type of modifier applied on fiber-glass, which could best benefit the mechanical properties of the glass fiber-PTFE composite.

Many researches have evaluated the effect of filler particle size. The experimental results presented by Germain et al.[19] indicate that at varying silica particle contents (25% ~ 35%), the composite resins filled with smaller (20 nm) silica particles had a higher compressive yield strength than those filled with larger particles (40 nm agglomerate) if the content of silica particles remained the same.

Li et al. [20] examined the size effect of boro-silicate glass particles on a polyphenylene polymethacrylate resin matrix and concluded that 15-μm filled resins tended to have superior mechanical and physical properties in terms of depth of cure, water absorption, compressive strength, and resistance to toothbrush abrasion than the 2-μm filled resins. This is an opposite tendency in behavior of compressive strength with various particle size observed [19]. But particle size did not have a strong impact on hardness, stiffness, and wear resistance to hydroxyapatite. It also has been reported that a decrease in the size of spherical particles in resins led to a increase in flexural strength, tensile strength, impact-absorbed energy [12], and in mechanical strength (hardness and compressive) and wear resistance [21].

Chen et al. [11] reported that 5-μm SiO_2-filled PTFE composites showed a slightly lower tensile strength than 25-μm SiO_2-filled PTFE composites, probably because composites filled with 5-μm SiO_2 have a higher SiO_2 filler surface area, which might absorb much more water and reduce tensile strength. It was also reported that the tensile strength tended to decrease with the increasing filler content is due to not only the decrease in the deformation area of the matrix upon increasing the fraction of the filler but also lack of adhesion between SiO_2 and PTFE.

A number of scientists proposed the relationship between the size of particles and tensile strength of the composites. Most researchers have agreed that the strength could a linear function of particle diameter or of the reciprocal of the square root of particle diameter.

The result of experiments of Landon et al. [22] on the tensile strengths of a particulate-filled rigid polyurethane resin validated Baldwin's proposal [23] that the tensile strength is a linear function of the mean particle diameter at a given filler content. The equation representing this function is given [22]:

$$\sigma_c = \sigma_m(1-\phi) - k(\phi)d \quad , \tag{2.1}$$

where σ_c is the tensile strength of composites, σ_m the tensile strength of matrix materials, ϕ the filler volume fraction, k a function of the filler volume function, and d the mean particle diameter. The particle size influence on tensile strength of the composite was attributed to the increase of Griffith flaw size with the increasing particle size [24].

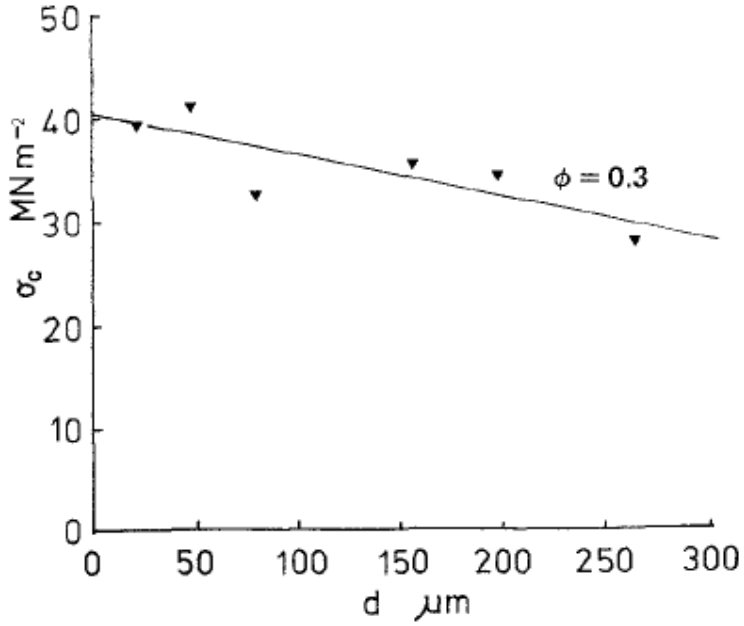

Figure 2.2. Tensile strength as a function of mean particle diameter d at a given filler volume 0.3 [22].

Hojo et al. [25] found that the strength of silica-filled epoxy had a linear relationship between tensile strength and the reciprocal of the particle diameter. The tensile strength increases as the size of the particles decrease following a relationship of the form:

$$\sigma_c = \sigma_m + kd^{-1/2} \quad , \tag{2.2}$$

where σ_c is the tensile strength of composites, σ_m the tensile strength of matrix materials, k a constant, and d the mean particle diameter.

Generally speaking, in most approaches the strength of composites is related to the strength of matrices and the particular geometric model of composites. The inclusions improve the strength of composites by increasing the fracture energy of a crack propagating through particles [26]. The increase in the strength of composites filled with small size particles could be attributed to a few factors. One important factor is considered the enhanced interfacial bonding provided by the increasing interfacial area [27]. Another factor was explained [24,28,29] by assuming that a crack front meets a dispersed phase and are pinned down in a similar way (Figure 2.3) to dislocations pinned in a crystalline material. Then the crack front would bow out until the front split by the particle met the other counterpart in the other side of the particle. Once two parts meet, the crack front would break away. As the distance between two particles decreases, either by increasing the volume fraction or decreasing the particle size, the radius of the crack front bow decreases and the arc at which the crack front breaks away increases. The force

required to bend the arc increases as a consequence. This procedure would continue until it becomes energetically unfeasible compared to other cracking propagation modes [22]. It should be noted that at low values of the volume fraction the influence of small particle tends to be consistent, but at a higher volume fraction it can be complicated [30,31].

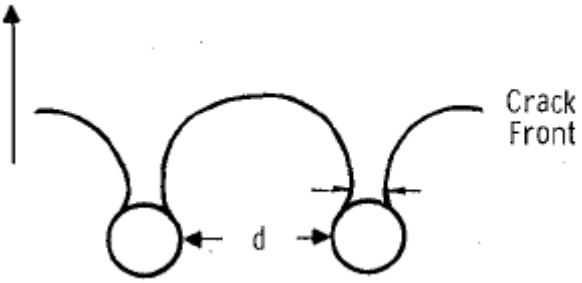

Figure 2.3. Breakaway position of crack front from one pairs of pinning positions, each separated by distance d. Once the arcs indicated by two small arrows meet, the crack front break away. Large arrow is direction of crack propagation. [24]

2.2 Dynamic Behavior and Applications of Thermites

Wang et al. [32] pointed out that Goldschmidt [33] in 1908 coined the word "thermite" to describe an exothermic reaction between Al and Fe_2O_3: $2Al + Fe_2O_3 = 2Fe + Al_2O_3$ (ΔH = -851.5 kJ/mol). Thermite reaction later was defined to involve a metal reacting with a metallic or a non-metallic oxide to form a more stable (less reactive) metal oxide and the corresponding metals or non-metal with a large heat release. Usually this heat generated in the reaction could increase the temperature higher than the melting points of both products. For example, the temperature in the above reaction is approximately 3000C, it could melt both Fe and Al_2O_3 (melting point of Fe is 1535C and

of Al_2O_3 2059C). Thanks to this high heat, a thermite reaction usually occurs in a local spot and could be energy self-sufficient to propagate in the bulk. It's an energy efficient reaction that is widely utilized in a variety of applications. Also owing to the unique characteristics of this exothermic reaction, the mechanisms of ignition becomes the point of special interest for enormous studies.

Despite the huge amount of heat released in reactions, thermites are generally safe to mix and store, but still some accidents happened. Undesirable ignition should be prevented. At the same time mechanisms of ignition control the performance of thermites and corresponding thresholds on mechanical stimulus.

In Section 2.2.1 the ignition mechanisms and processes of thermites are discussed, followed by Section 2.2.2, in which a brief introduction of the general applications of thermites is presented.

2.2.1 Dynamic Behavior of Thermites

Enormous efforts have been focused on the mechanisms of ignition (local heating) and roles of compositions and experimental conditions.

The most common ignition of thermite reactions is due to the temperature-induced combustion of one or both components in the mixtures [34-36]. But some researchers also studied other sources of ignition, such as mechanical impact [37]and a laser beam [38,39].

Field et al. [40,41] examined the hot-spot (local heating) formation mechanisms prosposed by a number of researchers over the years. The main mechanisms presented in the articles include (1) cavity collapse consisting of adiabatic compression of trapped gas pores and/or viscous or plastic heating of the surrounding matrix material; (2) friction between the impacting surfaces, the thermite materials and/or inside grit particles; (3) localized adiabatic shear of the material during mechanical failure; (4) various heating processes, such as viscous heating of material rapidly extruded between the impacting surfaces of grains, heating at crack tips, and heating at dislocation pile-ups; (5) spark discharge or triboluminescent discharge; (6) decomposition followed by Joule heating of metallic filaments. The above processes all involve the conversion of mechanical or electrical to thermal energy to form a hot-spot.

The effects of hot spot geometry and surrounding temperature on the critical hot spot conditions were investigated [42]. It was found that the smaller diameter of the hot spot, the higher the critical temperature for the hot-spot formation. Also, the critical time to ignition increases rapidly as the hot spot temperature decreases. Therefore, it was required to provide sufficient heat for a large volume of materials over relatively long time for a hot-spot ignition mechanism. Bowden et al. [43] have presented convincing evidence that the formation of critical hot spots required a dimension of typically 0.1 to 10 μm, a duration of $l0^{-5}$ to 10^{-3} s, and a temperature of greater than approximately 700 K to lead to ignition of reactions.

Walley et al. [37] studied a series of thermites using a drop-weight apparatus to investigate their respective sensitivity to mechanical impact and considered that the

impact energy released in the adiabatic shear band lead to the hot-spot formation. In Table 2.1, the compositions of thermites investigated in [37] are shown.

Table 2.1. Composition of thermites investigated by Walley et al. [37]

name	composition
SR 40	20% aluminium (heavy, grade 1, special type B) 20% silicon (4 μm or less) 60% potassium nitrate (125 μm)
SR 41	20% boron powder (amorphous, *ca.* 90%) 10% silicon (*ca.* 8–12 μm) 70% potassium nitrate (all pass 63 μm BSS)
SR 812	50% aluminium (heavy, grade 1, special type B) 50% potassium perchlorate (125 μm)
SR 813	40% aluminium (heavy, grade 1, special type B) 60% potassium perchlorate (125 μm)
Cu(III)O+Al	

Loose powders and pressed disk-form of the thermites in Table 2.1 were examined. Generally speaking, the loose powders had less sensitivity than the disk form of pressed thermites under the same impact condition. To sensitize the loose powders, two types of grits were added. The first type of grits was powdered borosilicated glass, a hard high-melting-point material, which was believed to create hot-spots by frictional rubbing [44]. Another type was polycarbonate, a tough but brittle amorphous material,

which was intended to create hot-spots at crack tips and shear bands [45]. It was found that the embedded polycarbonate disks in the loose powders contributed to the appearance of deflagration.

Probably because the pressed disk had a higher strength than the loose powders, they could absorb more energy from deformation to assist hot-spot formation. Disk samples of the thermites were examined by three setups of the drop-weight apparatus. One was to test uniaxial compression response with a normal drop-weight approach (Figure 2.4 a), the second was to test the shear response of right-circular samples by placing the anvils inclined 30^0 (Figure 2.4 b), the third was to test pre-shear samples (Figure 2.4 c).

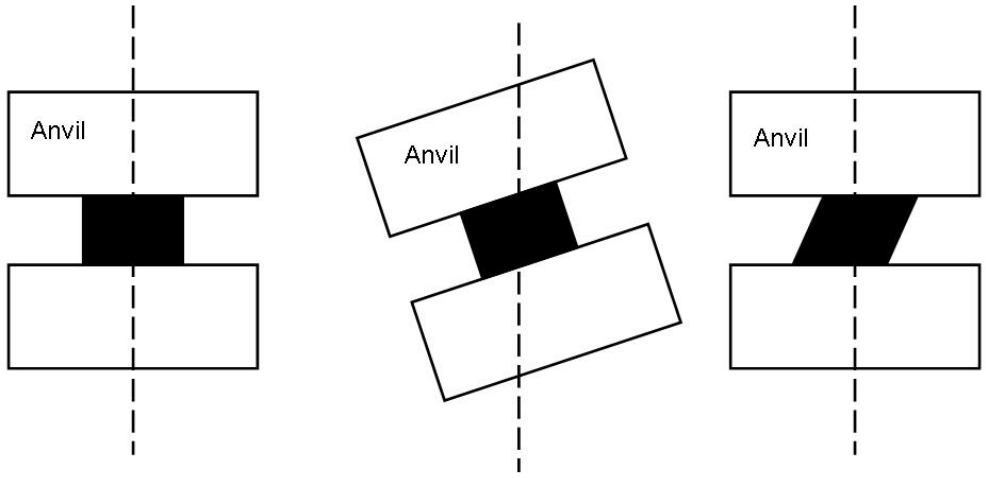

(a) (b) (c)

Figure 2.4. Schematic drop-weight testing setup (black regions represent samples): (a) normal approach; (b) inclined anvils to introduce shear; (c) the samples were pre-sheared.

According to the definition of sensitivity in this experiment, i.e. the proportion of deflagration events in all tests, it could be concluded that different thermites had different responses to the various drop-weight setups: (1) SR 41 was the most sensitive in the normal drop-weight tests, followed by SR 40, SR 812, SR 813 and Cu(III)O+Al in this order; (2) SR 41 was the most sensitive in the inclined-anvil drop-weight tests, followed by SR 812 and SR 813. But SR 40 and Cu(III)O+Al did not have deflagration events at all; (3) SR 41 and SR 813 had the greatest proportion of deflagration events in pre-sheared tests, followed by SR 40 and SR 813. But Cu(III)O+Al did not have deflagration events at all; (4) Generally speaking, materials tested under pre-sheared condition showed more sensitivity than under other conditions.

Figure 2.5 shows an example of the dynamic response of Cu(III)O+Al and SR 813 to the different test conditions. The reactants were placed in the center of the glass anvils. It is obvious that there was no deflagration for the Cu(III)O+Al. In figure 2.5 b, the black region in the center was unreacted SR 813 material, and the dark region close to the periphery of the glass anvil represents the reaction products. It could be seen that the reaction was fairly symmetric. In Figure 2.5 c, the inclined-anvil testing resulted in an asymmetric reaction, leaving a great portion of reactants unreacted. In Figure 2.5 d, the pre-sheared sample had a symmetric reaction.

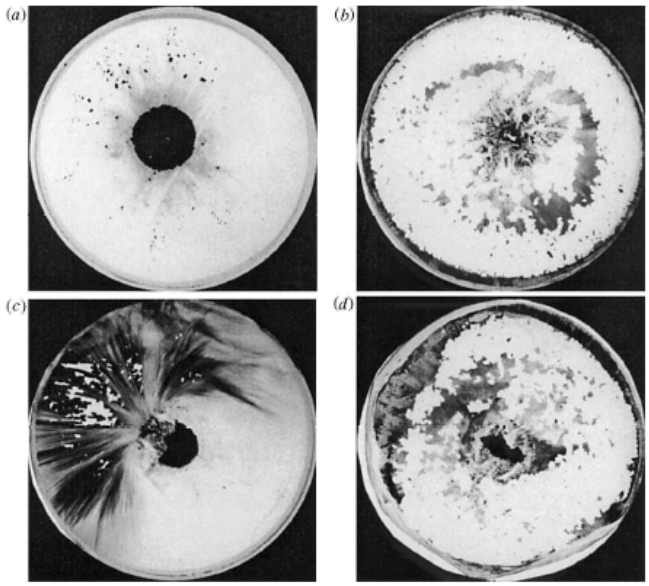

Figure 2.5. Photographs of glass anvils recovered from the drop-weight apparatus after testing pressed disks of (a) A 72 mg sample of Cu(III)O+Al composition under conventional impact test conditions. (b) A 79 mg sample of SR 813 under conventional impact test conditions. (c) A104 mg sample of SR 813 with inclined anvils. (d) A 75 mg sample of SR 813 'pre-sheared'. The glass anvils are 50 mm in diameter. [37]

2.2.2 Applications of Thermites

There are a variety of thermite applications in industry. One of the early applications is in metallurgy, because this type of reactions produces new metals and alloys [46-49], which can be easily separated in the molten condition. The heavier metallic products can be removed from the lighter oxide products solely by gravity. In all metals (Al, Mg, Ca, Zr, Zn and Ti) that can serve as a possible oxide reducing agent, Al is so far the favorite one for the following reasons [32]: (1) Al has a very high negative Gibbs free energy of oxide formation over a range of temperatures, though lower than CaO and MgO [50] to provide a more stable oxide; (2) Al_2O_3 has a lower melting point

than those of CaO (T_m=2580 C) and MgO (T_m=2800 C) to facilitate the separation process; (3) Al has a lower vapor pressure and does not boil when reacted at the atmospheric pressure so that it does not require a pressure-tight reaction vessel as Ca and Mg do; (4) Al is the most abundant metal in the Earth's crust and the third most common element in the Earth System by weight, so it’s a economy-friendly element; (5) its physical properties are well known. Another application of thermite reaction in metallurgy is welding [51,52]. Once the reaction is completed, the molten products can flow in the gap between two metal pieces; when products are solidified, the two metal pieces are jointed.

The utilization of thermite reactions in the synthesis of ceramic and composite materials [53-56] has received much attention in the past couple of decades. They are often categorized as self-propagating high-temperature synthesis (SHS). Table 2.2 gives a list of composites fabricated using SHS. Because the oxides of metals are more available than pure metals, thermite reactions represent cost-efficiency approach in SHS. Generally speaking, owing to the involvement of thermite reactions, the SHS usually involves two chemical reactions [32]: (1) reduction of the oxides to form metals; (2) then newly formed metals react with other ingredients to produce the desirable compounds.

Table 2.2. Thermite reactions in self-propagating high-temperature synthesis (SHS)[32]

Reaction
1. $Cr_2O_3 + 2Al \rightarrow 2Cr + Al_2O_3$
2. $2ZrO_2 + 2SiO_2 + 16/3Al \rightarrow 8/3Al_2O_3 + ZrSi_2 + Zr$
3. $TiO_2 + B_2O_3 + 10/3Al \rightarrow TiB_2 + 5/3Al_2O_3$
4. $TiO_2 + 4/3Al + C \rightarrow TiC + 2/3Al_2O_3$
5. $3Fe_3O_4 + 8Al \rightarrow 4Al_2O_3 + 9Fe$
6. $SiO_2 + 4/3Al + C \rightarrow SiC + 2/3Al_2O_3$
7. $2B_2O_3 + 4Al + C \rightarrow B_4C + 2Al_2O_3$
8. $2MoO_3 + 4Al + C \rightarrow Mo_2C + 2Al_2O_3$
9. $3TiO_2 + 4Al + 3/2C + 3/4N_2 \rightarrow 3Ti(C_{0.5}N_{0.5}) + 2Al_2O_3$
10. $3TiO_2 + 4Al + 1.5NaCN \rightarrow 3TiC_{0.5}N_{0.5} + 2Al_2O_3 + 1.5Na$
11. $6Mg + 2B_2O_3 + C \rightarrow 6MgO + B_4C$
12. $SiO_2 + Al \rightarrow Si + Al_2O_3 + N_2 + heat \rightarrow$ β-sialon, 15R-sialon, Al_2O_3, AlN
13. $Al + SiO_2 + C + N_2 \rightarrow$ SiC, AlN, AlON, Al_2O_3

In 1982, Odawara invented “Method for Providing Ceramic Lining to a Hollow Body by Thermit Reaction” [57]. In a centrifugal-thermite process (Figure 2.6) with A1-Fe_2O_3 powders [58,59], a mixture of reactants were placed in the pipes. After the thermite reaction was ignited while the pipes rotating along the axis, the released huge amount of heat melted the products so they could be centrifuged to the interior periphery of the pipes to form a homogeneous lining. Because Fe was heavier than Al_2O_3, the iron layers were the layer that bonded to the interior surface of the pipes and the ceramic (Al_2O_3) layers were the outside layer of the lining. Such a lining is an ideal solution to the requirement for a corrosion-resistant and abrasion-resistant layer next to a stronger metal layer.

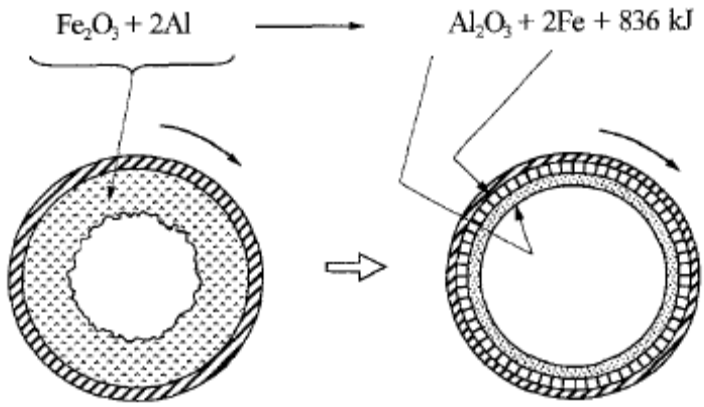

Figure 2.6 Schematic representation of the centrifugal-thermite process [60].

2.3 Reaction at High Velocity Impact of PTFE-Based Composites

The requirements for non-detonating reactive materials that have been intensively studied for projectile applications are a high density and exothermic reaction initiation upon impact. Many of these materials are granular materials. While granular materials are widespread, extensive research on their physics just started a few decades ago and the properties of complex granular materials remain unexplored so far. The considerable interest in granular materials is due to phenomena they exhibit in applications: segregation, fluidization, stress propagation, etc. [61-63]. For granular powder mixtures, the primary focus is on the kinetics of chemical reactions. Two classes of reactions were proposed by Thadhani [64] to explain the dynamic effects: shock-assisted reactions have been defined as those occurring in the time scale of thermal equilibration (tens of microseconds to milliseconds), while shock-induced reactions are those occurring in the time scale of pressure equilibration (nano- to micro-second duration) in shock-loading.

Meyers et al. [65] and Vecchio et al. [66] investigated Mo-Si and Nb-Si mixtures subjected to shock compression and proposed a mechanism for reaction initiation. This shock reaction was modeled by Eakins et al. [67].

A special class of energetic materials that are formulated to release high energy under high-velocity impact has been intensively studied to understand the mechanisms and the conditions for such reaction. These materials share a common feature: inert under quasi-static or static loads; but active under dynamic loads. So, generally speaking, they are safe to be carried and transported under regular transportation approaches. But high-strain-rate plastic deformation supplies sufficient energy to initiate and maintain reaction of these materials [1]. Traditional initiation methods, such as exploding bridge wires or flame initiation, are not able to provide adequate energy to support the consequent reaction.

These impact-initiated energetic materials generally consist of a polymer binder, metal powders, and binderless materials (primarily intermetallics and thermites). The dynamic properties and shock behavior of a few polymers, such as PTFE, Estane^{TM}, Kel-F-800^{TM}, polychloroprene, PMMA and epoxy resin, have been investigated to serve as the binder materials [68-71]. PTFE and Kel-F-800^{TM} exhibited constant shear strength behind the shock front, while other polymeric systems showed increased shear strength, a characteristic attributed to the viscoelastic/viscoplastic properties. The shear strengths of PTFE and estane^{TM} increased with the increase of impact stress, while that of Kel-F-800^{TM} had a constant strength. Teflon (PTFE) was also studied as an inert granular material under dynamic compaction [72] and explosive loading [73,74].

Polytetrafluoroethylene (PTFE) is an outstanding candidate as the binder material due to a favorable combination of properties: a low friction coefficient, high thermal stability, high electrical resistance, high chemical inertness, high melting point (327C), high melt viscosity (about 10^{11} poises at 380C), high thermal energy release when decomposed, and the easiness to deform [3]. But the application of PTFE is limited by a number of factors: the low mechanical strength, high thermal expansion, and excessive viscoelastic deformation under loading.

PTFE has at least four known phases depending on temperature and modest pressure [75] (Figure 2.7). At atmospheric pressure, below 19 °C, PTFE has a triclinic crystalline structure [76]. Above this temperature, it undergoes a first-order phase transition into a hexagonal structure with a 1.8% volume increase. A second transition occurs at 30 °C and it transits into pseudohexagonal. The thirdr transition occurs at the melting point 327 °C. Such an interesting phenomenon initiated extensive research on the failure mechanisms and microstructual evolution of PTFE at varying impact pressure and temperature conditions triggered a phase transition. It should be mentioned that the manufactured PTFE articles contain both amorphous and crystalline regions. It is not possible to manufacture fully amorphous or fully crystalline PTFE, even under laboratory conditions.

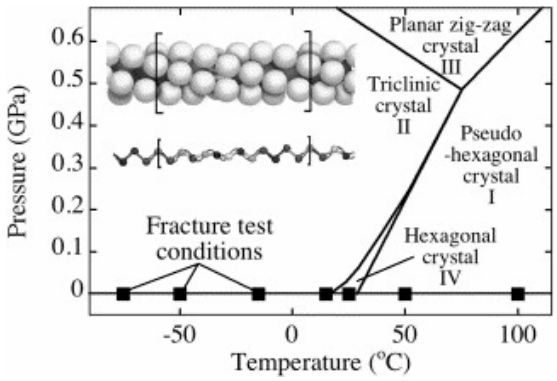

Figure 2.7. Temperature–pressure phase diagram for PTFE and crystalline structure of PTFE in phase II [77].

Ames [1] investigated four impact-initiated energetic materials (Al-PTFE, Zr-THV, Ta-THV, and Hf-THV) to understand how the materials formulations, initiation phenomena, reaction efficiencies, and the material properties (binder strength, material density, and sample mass) affect the energy release characteristics. All these materials were manufactured from the mixture of a fluoropolymer and a metal powder via a pressing/sintering process to achieve 96% and above of the theoretical maximum density. Sintering here is considered a critical step for the strength development in these composites, because it could improve the interparticle coalescence and diffusion of polymer chains across the interfaces [78]. PTFE was replaced with THV (a mixture of three different fluoropolymers: tetrafluoroethylene, hexafluoroethylene and vinylidene fluoride) because of the processing limitation. Taylor impact tests were performed to detect the initiation of reaction by the visible signs (such as light emission) and to link this information with the impact properties (such as impact speed and impact stress). It was observed that the initial blast occured in the first 1-10 μs and has an abrupt spatial gradient. This blast consumed only a small percentage of the materials. The remaining

unreacted materials continued to react with the oxidizer in the materials and the ambient oxygen in the following 10 ms. The afterburn reaction produced a slower and more global “quasi-static” pressure with little spatial gradient.

Reaction efficiency is based on the estimated energy release compared to the theoretical energy content, which is calculated based on the assumption that the initial metal-fluorine reaction is complete and the remaining hydrocarbon are reacted with the ambient oxygen [79]. As shown in Figure 2.8, the reaction efficiency is related to the impact speed for all the investigated materials. The higher the impact speed, the higher the reaction efficiency. The mechanical work associated with the fracture energy contributes to the difference of reaction efficiencies. It is apparent that the reaction efficiency is not linearly related to the impact speed, i.e. the mechanical work. It is likely that there is one reaction efficiency threshold for each material. Once the threshold is reached, further increase in fracture energy, i.e. the increase in the impact velocity, would not lead to much improvement on the reaction efficiency.

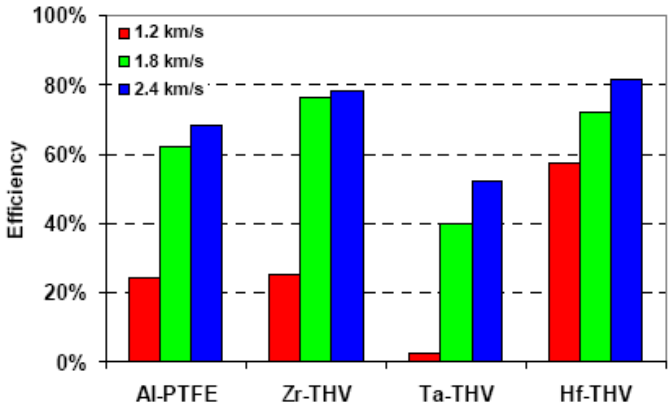

Figure 2.8 Reaction efficiency of different materials at varying Taylor impact velocity. [1]

The material properties, including binder strength, material density, and sample mass, effect on the energy release characteristics were investigated [1].

It has been observed that the binder strength inversely affected the reaction efficiency of materials. Two binder materials were selected to make a comparison [1]: THV500 and THV200. They had essentially same chemical formulation but go through different processing routes. THV500 had a higher compression yield strength (12MPa) and a higher melting point (165^{o}C) than THV200 (5.0 MPa, 124 ^{o}C). Figure 2.9 shows that the composite with a weaker binder material (THV200) has a higher efficiency than the composite with a stronger binder material (THV500). It could be due to the weaker binder material flowing easily between the metal particles to generate more initiation/reaction locations. To an extreme extent, an infinitely strong material would never exhibit such a mechanism. As expected, the composites with the weaker binder (THV220) exhibit a higher reaction efficiency at the same impact speed. It should be pointed out that the weaker binder has a low melting point, which could lead the easily-melting binder to a better mixture with the fuel to create more initiation/reaction locations. Therefore, a portion of the increase in reaction efficiency should be attributed to the low melting point of THV200.

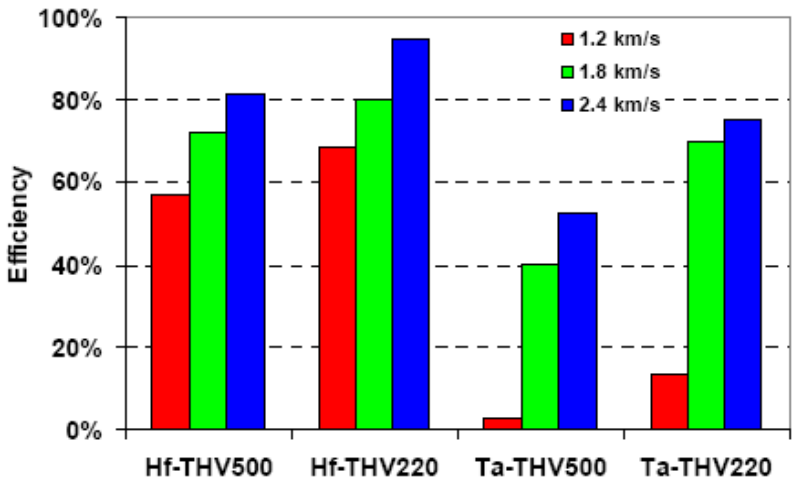

Figure 2.9 The influence of binder strength on the reaction efficiency of impact-initiated materials. [1]

It has been observed that a low density of a material could positively lead to higher reaction efficiency. Effects of material density on reaction efficiency were examined through the comparison of more than 20 various materials which have very different constituents (different binders, different metal powders, different thermites and so on) [1]. The results in the Figure 2.10 show that a lower density leads to high reaction efficiency. The reaction efficiencies of these more than 20 materials have been normalized to PTFE-Al. It can be seen that the reaction efficiency has a strong dependence on material density than the material constituents. For this reason, a PTFE-Al composite is particularly of strong interest among scientists.

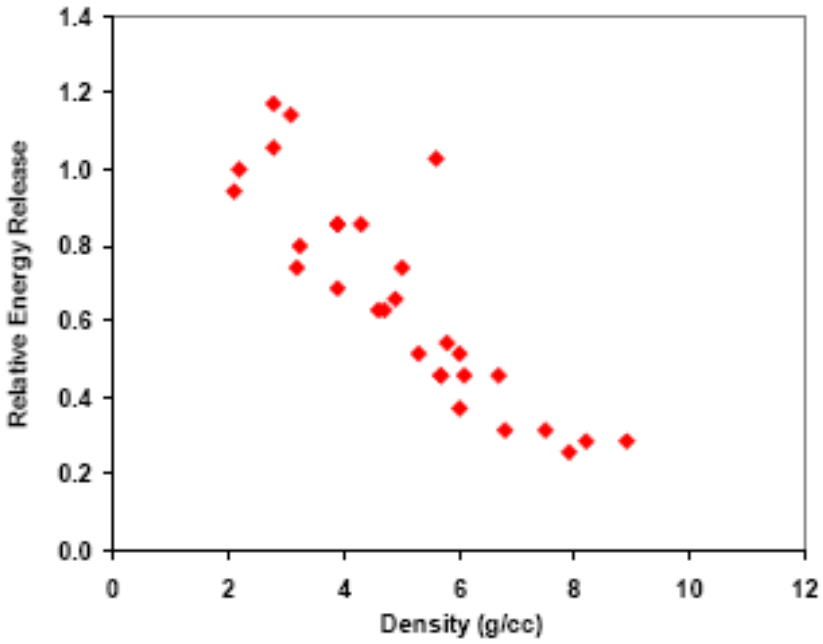

Figure 2.10 The reaction efficiency as the function of material density at the 6000 ft/s impact speed. [1]

It seems that there is a threshold for the sample mass to be a linear function of energy release, at least in the PTFE-Al case. The sample mass was considered as a possible factor on reaction efficiency of impact-initiated materials because these materials require a certain amount of energy release during high-strain-rate plastic deformation and the sample mass could have effect on the deformation process [1]. To investigate this effect, Ames utilized PTFE-Al samples weighing from 6.5 g to 52.4 g. The effect of sample mass can be seen from Figure 2.11. In this plot, the results for the sample were normalized to the standard 19.4 g sample (Reference line). If the energy release ratio is independent of sample mass, a linear function is expected and all data should be on the straight line. However, only samples that are less than 19.4 g

demonstrate such a behavior with the exception that all materials tested at 1.2 km/s impact speed are independent of sample mass. It is apparent that sample mass has an influence on the energy release ratio for the samples that weigh more than 19.4 g. It is reasonable to speculate that large samples require large amount of energy to maintain further reaction compared to small samples at the same-speed impact.

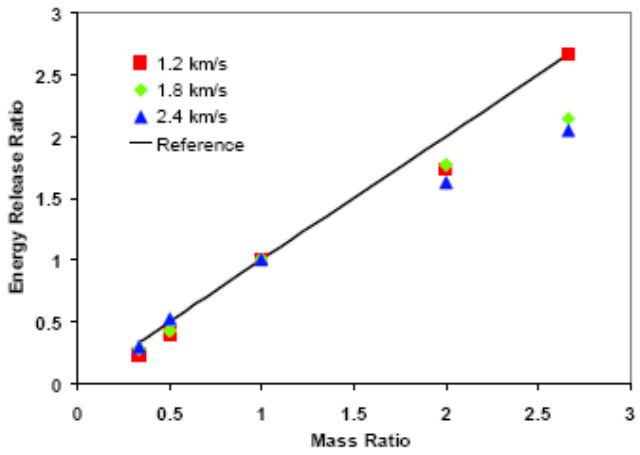

Figure 2.11. The effect of sample mass effect on reaction efficiency [1]

The relationship between the impact stress and the sample deformation and reaction process has also studied. The sequence of photographs (Figure 2.12) shows the evolution of the direct impact process of a sample rod, consisting of 26.5 wt% Al and 73.5 wt% PTFE [80]. The impact stress was 10.4 kbar. Impact occurs at 0 microsecond. The time after impact was given at the top left of each frame in microsecond. 0, 12, and 24 microseconds frames show the rod shape before initiation. Rod deformation was observed away from the impact surface leading to a curtain amount of energy relax. Increasing impact stress should improve this situation. At 36, 48, and 60 microseconds

the frames show the light after initiation. Light grew from discrete points, possibly from cracks, to a single glowing source. An expansion cloud was observed after reaction initiation (first light) and went to the surface of the sabot. It is suggested that the scattered particles from the impacted/fractured rod reacted with the sabot it was hit.

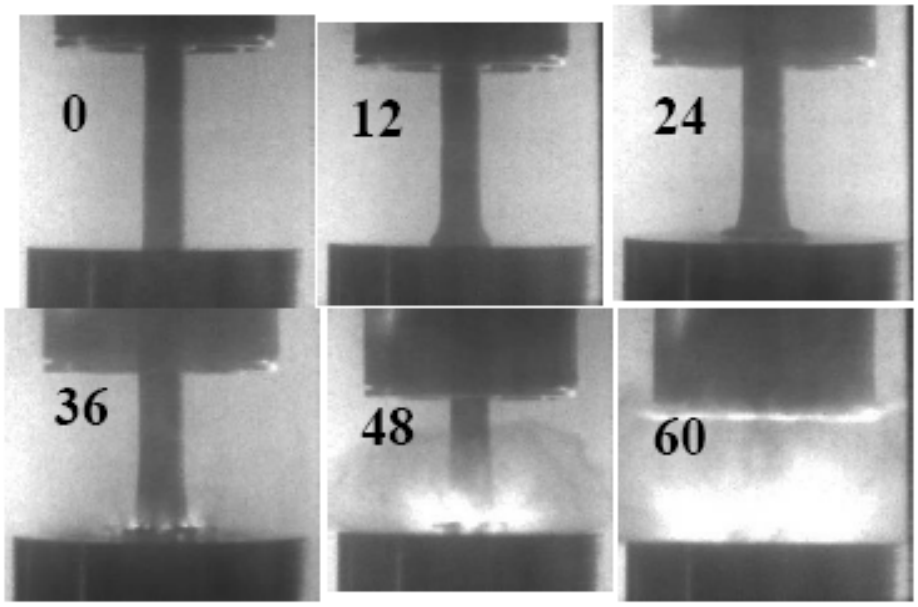

Figure 2.12 Evolution of the rod comprising 26.5 wt% Al and 73.5 wt% PTFE sample impacting steel anvil. [80]

The plot in Figure 2.13 reveals first light (initiation) as the function of calculated impact stress for the Al-PTFE rod experiments. It indicates that no initiation would occur given the impact stress less than 7.3 kbar. Once impact stress is higher than the threshold 7.3 kbar, the initiation time drops dramatically from 70 microseconds to about 20 microseconds at about 15 kbar. The further decrease of initiation time corresponds to the further increase in impact stress in a slower fashion. The data above the threshold of 7.3

kbar fitted with the curve $T(\sigma - 7.3)^{0.5} = 48$, where T is in microseconds and σ in kbar. In the direct impact tests, the sabot was in contact with the back of Al-PTFE rod all the way through the entire impact progress. To ensure that the presence of the sabot did not influence the initiation time, the authors utilized the reverse ballistic testing technique. The result of reverse ballistic testing fitted the above mentioned curve. This fact indicates that the attachment of the rod to the sabot did not change the overall initiation time. Another indication was that the back of the rod did not move in the direct impact test until the time of interest passed. It means that even if an impact compression wave propagated from the impact interface to the end of the rod, it did not cause the end to move; therefore this behavior suggests that the sabot did not have an effect on the initiation time.

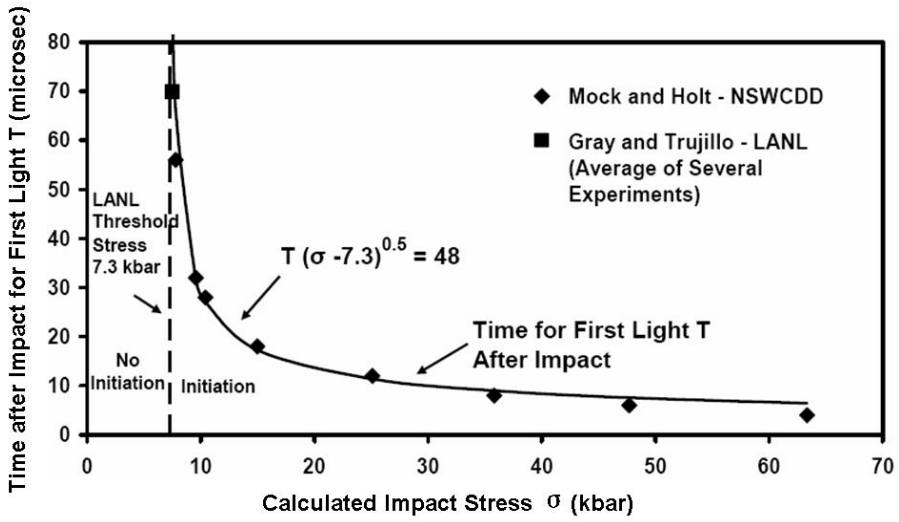

Figure 2.13 Time after impact for first light as the function of impact stress [80].

CHAPTER 3

EXPERIMENTAL TECHNIQUES

In this chapter, the materials of samples, the preparation of samples, and sample testing techniques will be introduced. A variety of techniques have been employed to investigate the mechanical and microstructural properties of materials. Mechanical testing techniques can be classified into four categories according to the deformation strain-rate: creep and stress relaxation, quasi-static, dynamic, and impact (Figure 3.1). The techniques utilized in this research include quasi-static and dynamic testing.

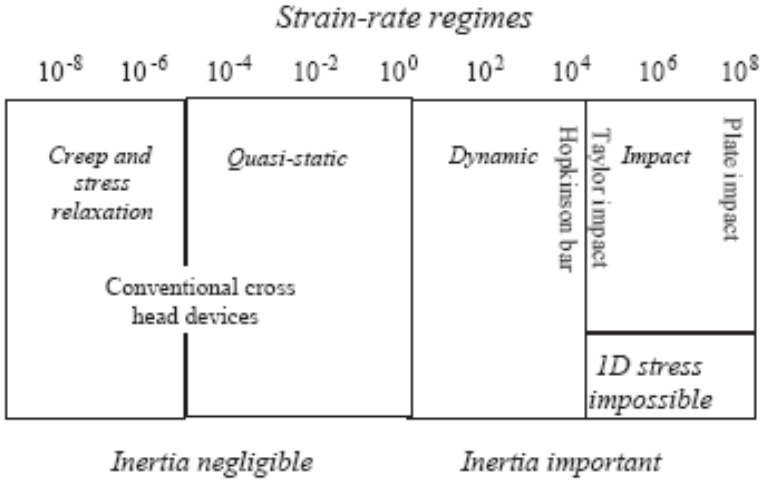

Figure 3.1 Schematic diagram of strain rate regimes (in reciprocal seconds) and the techniques that have been developed for obtaining them. [81]

3.1 Sample Preparation

The composite samples were prepared in our lab. The mixture of powders were mixed in a SPEX 800 ball mill and densified in an ABB Cold Isostatic Press (CIP). Table 3.1 summarizes the characteristics of as-received powder materials used in PTFE-based composites.

Table 3.1 Characteristics of commercial powders used in the research

Powder	Particle Size (μm)	Purity (wt. %)	Manufacturer
Sn	-325 mesh (<44)	99.8	Alfa Aesar
H-95 Al	-100 mesh (<170)	99.7	Valimet
H-2 Al	2-3	99.7	Valimet
Coarse W	-325 mesh (<44)	99.5	Teledyne
Fine W	<1	99.5	Alfa Aesar
MP 1500J PTFE	Ave. 100 nm		Dupont

3.1.1 Ball Milling

The objectives of milling include particle size reduction, mixing or blending, particle shape change, and microstructure transformation. High-energy ball milling has been extensivly applied [82-85] in mechanical alloying to initiate chemical reactions along the self-propagation path since it was developed by Benjamin and coworkers at the International Nickel Company in the late 1960s [86,87].

In this research, ball milling was employed to break down the agglomeration of powders. The powders were mixed, corresponding to the pre-determined ratio, and ball milled in an alumina vial set in the SPEX 800 for about 2-10 minutes using alumina balls with a 1:5 mass ratio of balls to powder. To increase the density of the sample consisting of fine W powder, Al powder, and PTFE powder, the fine W powder was separately ball milled before it was mixed with the other two powders to break down the agglomeration.

3.1.2 Cold Isostatic Pressing

To obtain high-accuracy cylindrical and hollow sample, a cold isostatic pressing technique was adopted. The corresponding device used to fabricate the samples of the well-mixed powders was designed for our needs. Figure 3.2a illustrates the setup for this device. The base was screwed to the slightly tapered (the diameter of the entry is 10.55mm, the slop to the larger bottom of tube is 1^{o}) stainless steel tube. One hollow/solid stainless steel plug was place to the bottom of the tube, the base. To make a hollow sample, a slightly tapered stainless steel rod (the bottom diameter is 5 mm, and

the slope to the larger top of the rod is 1^{o}) was inserted into the plug. Then, the mixed powders were carefully added into the tube. Another hollow/solid stainless steel plug was placed at the top of the powders. The whole setup was then placed into a rubber jacket with two rubber plugs placed at the both ends. Metal clamps surrounded the rubber plugs to fasten them to avoid the pressure transmitted medium in this research, oil, oozing into powders and contaminated them. After that, the whole assembly was placed in the high pressure chamber filled with oil in Cold Isostatic Press (CIP) (Figure 3.2b).

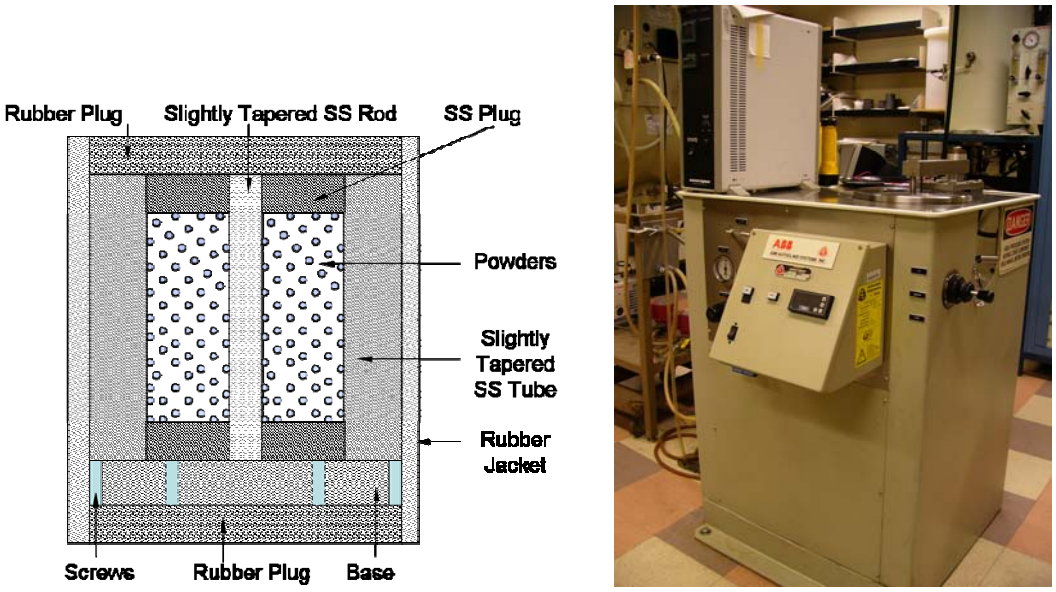

(a) (b)

Figure 3.2 (a) Experimental set up to prepare high accuracy samples from powders; (b) ABB Cold Isostatic Press (CIP).

This equipment is typically employed to pressurize powders into solid samples under room or elevated temperature (up to 150C) and pressures up to 350 MPa. In this

research, the pressure in CIP usually went to the highest limit, 350 MPa to fully compress the powders. After the pressure ramped to 350 MPa, it would be held constant for about 20 mins before it gradually reduced to the atmosphere through slowly venting for about another 10 minutes. It should be mentioned that under high pressure conditions during cold isostatic pressing the top rubber plug (except its central part facing the stainless steel (SS) rod) “flows” freely into a stainless steel tube following the displacement of the top stainless steel plug.

After the pressing cycle, the assembly (Figure 3.2 a) was taken out and disassembled. The sample was gently pushed out towards the increasing diameter of the stainless steel tube. The stainless steel rod was designed with a slightly smaller diameter bottom (the inner diameter of the stainless steel tube tapers from 10 mm to 10.40 mm from the top to the bottom); the stainless steel was designed with a slightly larger diameter bottom (the rod diameter tapers from 5 mm to 4.80 mm from the top to the bottom end). Both designs provided a smooth, easy way to take out the samples without damaging. After CIPing, the sample height was reduced from 45 mm (at most) to 3-12 mm depending on the size and initial height of the loose powder. The shape of the prepared samples is shown in Figure 3.3. The samples made by CIPing had the following geometries: (a) the diameter of the solid cylinders was 10.44 mm and heights vary from 3 mm to 10 mm; (b) the inner diameter of the hollow cylinder is 4.76 mm and the outer diameter is 10.44 mm and the heights varied from 3 mm to 10 mm. The height of the samples was controllable and affected by the mass of powder and the porosity of samples. Thus, these samples had precise dimensions.

(a) (b)

Figure 3.3 Typical shapes of samples prepared by CIPing.

The compositions of the investigated polymeric composites are listed in Table 3.2. The ratio of PTFE and Al corresponded to the stoichiometric composition of compound AlF_4 in this research. The densities of the samples were estimated based on the geometry of the high-accurate-dimension samples. The porosity was estimated based on the theoretical density of samples.

Table 3.2 shows the density of various CIPed samples. Note that under the same pressing conditions (sample size, pressure and time) and the same volume content of components, the PTFE-Al-W sample with fine W particles reached a density of ρ= 6 g/cm^3, while PTFE-Al-W samples with coarse W particles could reach a density of ρ= 7.05 g/cm^3, which is close to the theoretical density. To investigate the behavior of materials with the same porosity but different particle sizes of W powder, porous coarse PTFE-Al-W was intentionally introduced with the increased porosity to the level similar to the porosity of sample with fine W particles. This goal was accomplished by significantly reducing the CIPing pressure to 20 MPa. One of the initial hypotheses for

this unusual behavior was “closed” porosity of agglomerated fine W particles resulting in porous space between them where PTFE did not penetrate and subsequently smaller density of the mixture.

Table 3.2. Parameters of CIPed samples processed at different conditions.

Name	Materials	Pressure (MPa)	Theoretical Density (g/cm3)	Experimental Density (g/cm3)	Porosity (%)
Dense Pure PTFE	100 nm PTFE, 100wt%	350	2.22	2.20	1.0
Dense PTFE-Sn	<44 microns Sn, 46wt%; 100 nm PTFE, 54wt%	350	3.24	~3.20	1.2
Dense PTFE-coarseAl	95-micron Al, 24wt%; 100 nm PTFE, 76wt%	350	2.30	~ 2.23	3.0
Dense PTFE-fineAl	2-micron Al, 24wt%; 100 nm PTFE, 76wt%	350	2.30	~2.23	3.0
Dense PTFE-Al-coarseW	<44 microns W, 77wt%; 2-micron Al, 5.5wt%; 100 nm PTFE, 17.5wt%	350	7.17	~7.05	1.6
Porous PTFE-Al- fineW	<1 micron W, 77wt%; 2-micron Al, 5.5wt%; 100 nm PTFE, 17.5wt%	350	7.17	~ 6.00	14.3
Porous PTFE-Al- coarseW	<44 microns W, 77wt%; 2-micron Al, 5.5wt%; 100 nm PTFE, 17.5wt%	20	7.17	~ 6.00	14.3

A large scale PTFE-Al-W (length 116 mm, inner diameter 9.9 mm and outside diameter 30 mm) (Figure 3.4) sample containing fine W particles was also prepared for an explosively driven thick walled cylinder test to examine if explosively driven high

strain-rate deformation develops into pattern of multiple shear bands with subsequent reaction initiation as in the case of Ti-Si mixture (Nesterenko, 2001).

(a) (b)

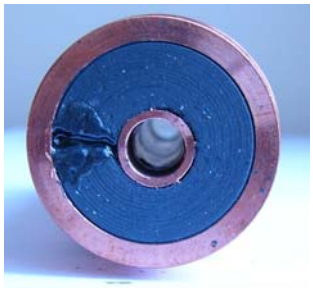

(c)

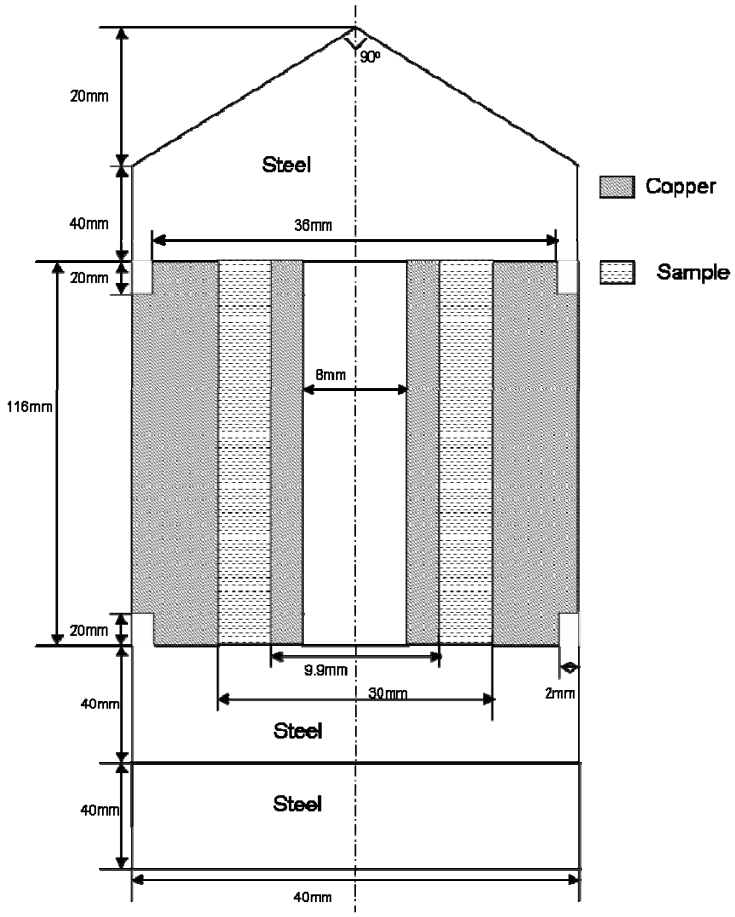

(d)

Figure 3.4 Sample for explosively driven TWC test: (a) the tubular sample inserted between two copper tubes, inner stopper tube and driving outside tube; (b) the whole assembly with bottom (including momentum trap steel cylinder) and top steel plugs attached; (c) the cross-section shows the inner copper stopper and the outer copper driver; (d) the geometry of the assembly.

In this research, all mixtures (PTFE+Sn, PTFE+Al, PTFE+Al+coarseW) except one (PTFE+Al+fineW) could be practically fully densified into their respective

theoretical density, leaving just 0.5~1% porosity. However, the densification of the mixture of PTFE, Al, and fine W presented a challenge and could not be achieved in this CIP instrument. It might be fully densified with a higher pressure.

3.2 Quasi-static Compression Testing

Quasi-static compression tests were performed using the SATECTM Universal Materials Testing Machine (Instron; Canton, MA) with a 5,000 lb loading capacity. The load was applied at a rate of 10^{-3} s^{-1} and was stopped when the sample was fractured. The load-displacement data were recorded and converted to true stress-strain data.

3.3 Equal Channel Angular Pressing (ECAP)

Equal channel angular pressing (ECAP) developed by Segal [88] was applied successfully to metals [89-91], such as aluminum, magnesium, and copper alloys, and to carbon composites [92,93] for increasing their strengths by refining the grain size. But little attention has been paid to its application to polymers.

In this research, a 90^{o} ECAP die was used. A unique horizontal split was designed to facilitate the replacement of the lower block with channels of different angles while the top piece block could remain unchanged, making the device more versatile to be applied for various needs [94]. The outer arc (ψ) of the channel curvature is a smooth 20^{o}.

Except at the entry and exit points, the channel diameter is uniformly 0.95 cm. The diameter of the channel at the entry and exit points was slightly increased to decrease friction between samples and the channel and avoid unnecessary deformation or fracture. Pressing was carried out using H-13 tool steel plunger guided by a hydraulic press. The tolerance of the plunger was kept extremely low to prevent the sample material from flowing between the walls and the plunger. The hydraulic press provided a 2.54 GPa load to the plunger to pass the stress onto the samples. Both the samples and the plunger were well lubricated using vacuum grease before pressing. Figure 3.5 shows the design of the ECAP die.

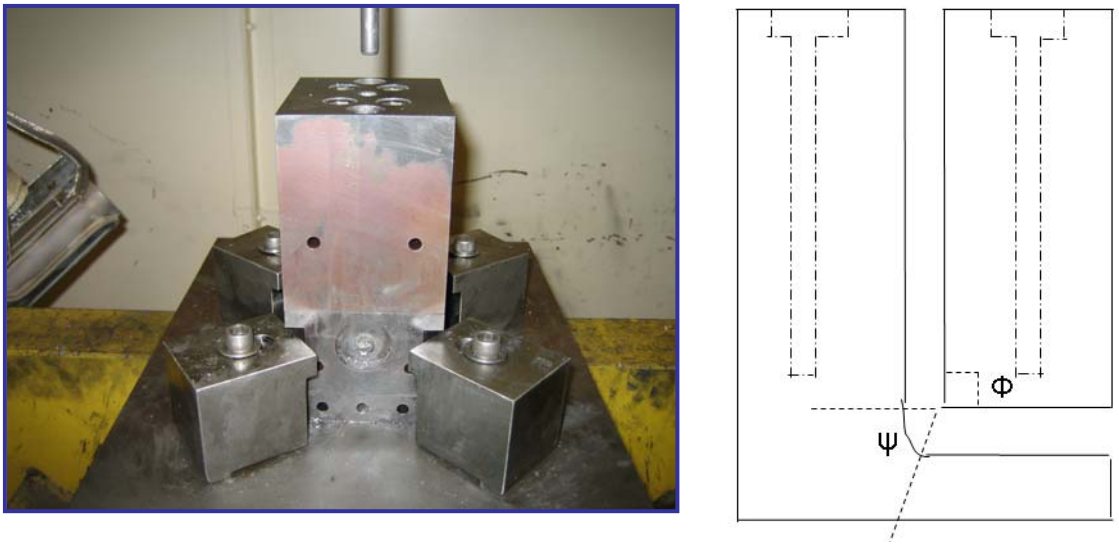

(a) (b)

Figure 3.5 (a) ECAP facility; (b) Schematic cross section of die.

The shear strains were calculated using Equation (3.1) [95], in which Φ is the inner die angle, 90^{o}, ψ is the angle of the curved portion of the channel, 20o, and N is the pass number which is 1 in this research. The resulting shear strain is 191%.

$$\varepsilon_N = \frac{N}{\sqrt{3}}\left[2\cot\left(\frac{\Phi}{2}+\frac{\Psi}{2}\right)+\Phi\cos ec\left(\frac{\Phi}{2}+\frac{\Psi}{2}\right)\right] \tag{3.1}$$

3.4 Hopkinson Bar Testing

Hopkinson Bar technique has been used to accurately provide a complete stress-strain history to understand the properties of materials and compare to the numerical simulation data. The split Hopkinson pressure bar (SHPB) was originally developed by Kolsky [96] and has been intensively employed and modified to determine the dynamic reponse of a variety of engineering materials, such as metals[97,98],concrete [99], ceramics[100], composites [101], and polymers [98].

In this section, the technique and theory of the Hopkinson bar is presented. The conventional split Hopkinson bar and a few modified Hopkinson bars are introduced. Compared to the conventional Hopkinson bar, which is more suitable for testing on strong materials, modifications were proposed for testing soft materials. The advantages and limitations of modified Hopkinson bars are described. The theory of the Hopkinson bar shear testing is also introduced.

3.4.1 Split Hopkinson Pressure Bar Compression Testing

The basic idea of the SHPB is that a sample is deformed between two bars excited above their resonant frequency [81], therefore, this technique provides accurate deformation history of the sample. Hopkinson bar technique has been increasingly used as a standard method of measuring the dynamic properties in the strain rate range 10^3-10^4 s^{-1}. The materials of the bars are chosen so that they remain elastic (usually small strain) while the samples may be driven to plastic deformation (usually large strain). Dynamic loading is realized by releasing the pressurized gas in the launch chamber to drive the striker bar which hits the incident bar. The resulting elastic wave travels through the sample and transmitted into the transmitted bar. It is reflected at the incident bar/samples interface so the incident wave, the reflected wave and the transmitted wave could be recorded and analyzed (Figure 3.6). Hopkinson bar testing also provides information for a constitutive equation that represents the materials' dynamic behavior under specific circumstances at a given temperature and strain rates. One application [102,103] is to obtain high-strain-rate data for the failure of solder joint in cell phones. When a cell phone is dropped on a concrete floor, a high magnitude of dynamic force at the solder joints occurs, thus generating high-strain-rate impact.

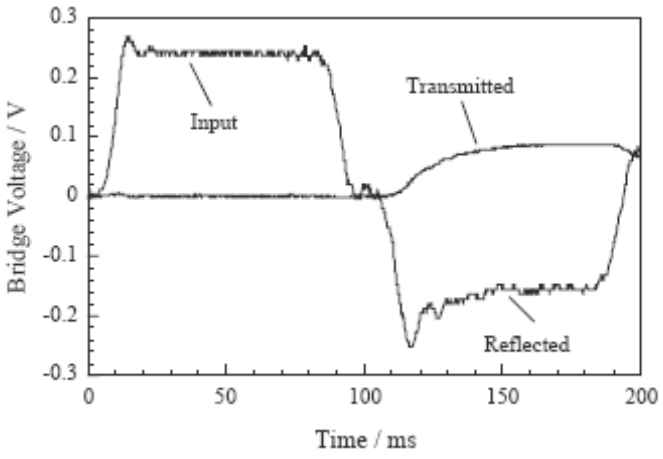

Figure 3.6 Typical incident, reflected, and transmitted signals from a split Hopkinson bar experiment [81].

3.4.1.1 Theory of Conventional Split Hopkinson Bar

The Hopkinson bar technique was initially developed by Hopkinson [104] and later refined by Kolsky [96]. The theory of the Split-Hopkinson Pressure Bar is presented as followed [97]. The schematic illustration (Figure 3.7) shows strains (ε_i, ε_r, ε_t) in elastic wave traveling in a typical split Hopkinson bar test. Displacement (u_1 and u_2) on two sides of the sample with thickness l_s are also shown in Figure 3.7.

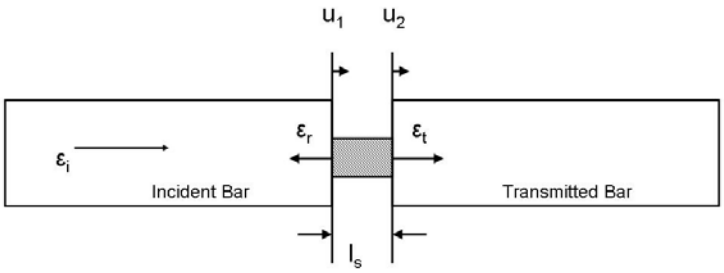

Figure 3.7 Illustration of incident bar, sample, and transmitted bar in a Hopkinson bar.

The wave equation within the bars is:

$$\frac{\partial^2 u}{\partial x^2} = \frac{1}{c^2}\frac{\partial^2 u}{\partial x^2} \tag{3.2}$$

has the solution:

$$u = f(x - ct) + g(x + ct) = u_i + u_r, \tag{3.3}$$

in which u_i and u_r are the displacements of the ends of the sample. In a one-dimensional system, the strain ε is given by:

$$\varepsilon = \frac{\partial u}{\partial x}. \tag{3.4}$$

Therefore strain in the incident bar can be determined by differentiating equation (3.3) with respect to x:

$$\varepsilon = f' + g' = \varepsilon_i + \varepsilon_r. \tag{3.5}$$

Differentiating equation 3.3 with respect to time gives the velocity of the incident bar:

$$\dot{u}_1 = c(-f' + g') = c(-\varepsilon_i + \varepsilon_r). \tag{3.6}$$

The velocity in the transmitted bar is given by differentiating the time derivative of the displacement in the transmitted bar, $u_t = h(x - ct)$:

$$\dot{u}_2 = -c\varepsilon_t. \tag{3.7}$$

The strain rate in the sample is calculated from:

$$\dot{\varepsilon} = \frac{(\dot{u}_1 - \dot{u}_2)}{l_s}, \tag{3.8}$$

where l_s is the instantaneous length of the sample. Combining equations 3.6, 3.7, and 3.8, the strain rate in the sample can be calculated from the strains in incident, reflected, and transmitted waves by:

$$\dot{\varepsilon} = \frac{c}{l_s}(-\varepsilon_i + \varepsilon_r + \varepsilon_t). \tag{3.9}$$

The forces in the two bars on the corresponding sides of the sample are:

$$F_1 = AE(\varepsilon_i + \varepsilon_r) \tag{3.10}$$

and

$$F_2 = AE\varepsilon_t, \tag{3.11}$$

where A is the cross-sectional area of the bar and E is the Young's modulus of the incident and transmitted bars which are assumed to be equal.

It is assumed that the sample is in force equilibrium, and the sample deforms uniformly after an initial "ringing-up" period. If these assumptions are valid, the forces on the two ends of the sample are equal, i.e. $F_1 = F_2$. Therefore, combining equations (3.10) and (3.11) yields:

$$\varepsilon_t = \varepsilon_i + \varepsilon_r \,. \tag{3.12}$$

Substituting (3.12) into (3.9) gives a relationship for calculating the strain rate in the sample:

$$\dot{\varepsilon} = \frac{2c\varepsilon_r}{l_s} \,. \tag{3.13}$$

The stress in the sample is calculated by dividing the force in Equation 3.11 by the cross-sectional area of the sample:

$$\sigma(t) = \frac{AE\varepsilon_t}{A_s} \,. \tag{3.14}$$

Therefore, the stress-strain curve can be determined from the two strain gage signals.

3.4.1.2 Modified Hopkinson Bar for Soft Materials

The conventional Hopkinson bar is a reliable experimental technique to obtain the high-strain-rate response of high strength materials. However, limitations on the magnitude of the transmitted bar signal due to low signal-to-noise ratio and inhomogeneous deformation of soft materials (low strength and low impedance) in the conventional Hopkinson bar have been an obstacle to researchers. A low impedance material allows the incident bar-sample interface move relatively free, causing only a very small portion of transmitted wave passing through the sample. As a result, the

amplitude of the transmitted pulse in the traditional Maraging steel bar is usually very low compared to intrinsic noise level, making the data reading very difficult. Figure 3.8 shows a typical Hopkinson bar signals of a soft material. It is obvious that a small amplitude transmitted pulse for a RTV630 silicone rubber sample tested in a conventional Hopkinson bar is too weak, compared to the amplitude of noise, for the accurate interpretation of the dynamic response of this material. Another problem related to the traditional technique is the rising time for the incident pulse. A typical rising time for the traditional Hopkinson bar material, Maraging steel, is less than 10 μs. During this period, because of low speed elastic wave in low impedance materials, the state of force equilibrium at both ends of the sample may not be reached. The loading pulse traveling back and forth with the sample more than three times is required to reach the dynamically equilibrated stress [105,106]. To address these problems, a number of investigations have been conducted.

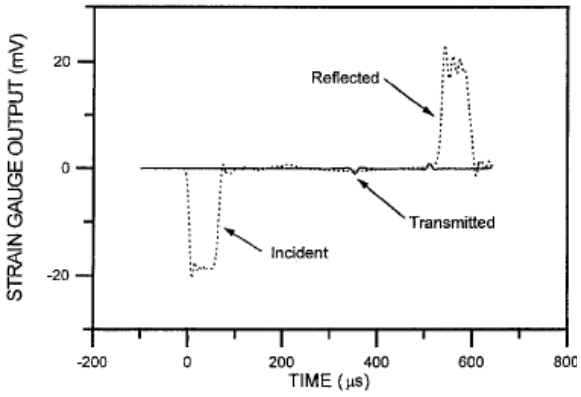

Figure 3.8 Strain time records for an RTV630 silicone rubber sample using a conventional split Hopkinson pressure bar. [107].

Sawas et al. [108] proposed an all-polymeric (cast acrylic) split Hopkinson bar to achieve a closer impedance match between the pressure bars and the sample materials, thus providing both a low noise-to-signal ratio data and a longer input pulse for higher maximum strain. However, because of the viscoelastic behavior of the incident and transmission bars, the traditional analysis of data is not valid and the viscoelastic wave propagation equations should be adopted. This method was examined in the high-quality stress-strain data for polycarbonate, polyurethane foam and Styrofoam.

Chen et al. [107] employed a low Young's modulus Al alloy instead of steel as the bar material and adopted a hollow transmission bar design (Figure 3.9) to increase the amplitude of transmitted strains pulse by one order of magnitude compared to the conventional technique. In addition, a polymer disk serving as a pulse shaper was placed to the impact end of the incident bar to generate a longer rising time of the incident pulse to ensure stress equilibrium and homogeneous deformation in soft materials. An Al alloy bar also avoided the effect of dispersion and shifting of elastic strain pulses [109,110] in bars made of viscoelastic materials. The problem related to this method is that the Al cap which was used to support the sample could present a potential challenge to the one-dimensional wave propagation equation.

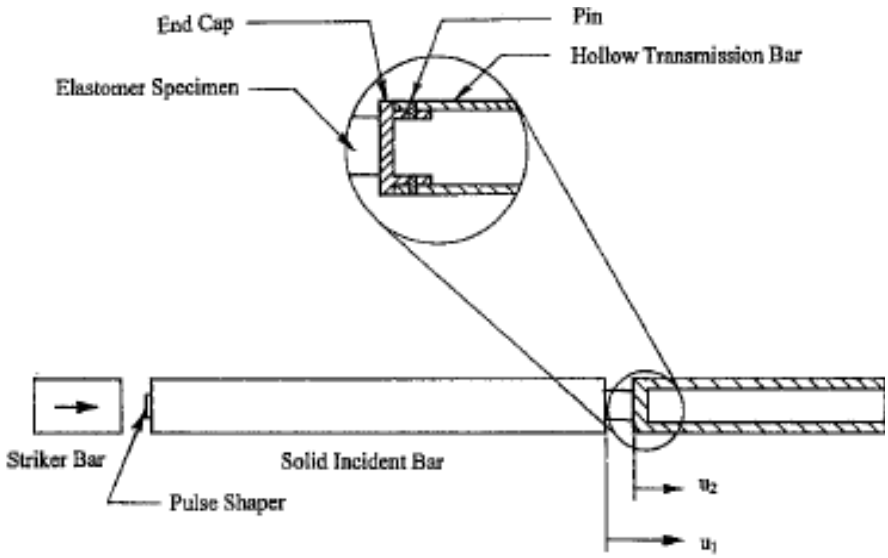

Figure 3.9 Schematic of the modified split Hopkinson pressure bar with high-strength aluminum bars for testing low impedance samples [107].

Another modification made to the Hopkinson bar involved an embedded quartz transducer instead of strain gages in Al bars (Figure 3.10a) [111,112] to directly measure the time-resolved transmitted force. This approach could increase the amplitude of the transmitted pulses over three orders of magnitude compared to the conventional Hopkinson bar technique to examine the dynamic behavior of rubber and Styrofoam. Compared to Figure 3.8, the transmitted wave in Figure 3.10b is much more distinctive to make the accurate interpretation of deformation history.

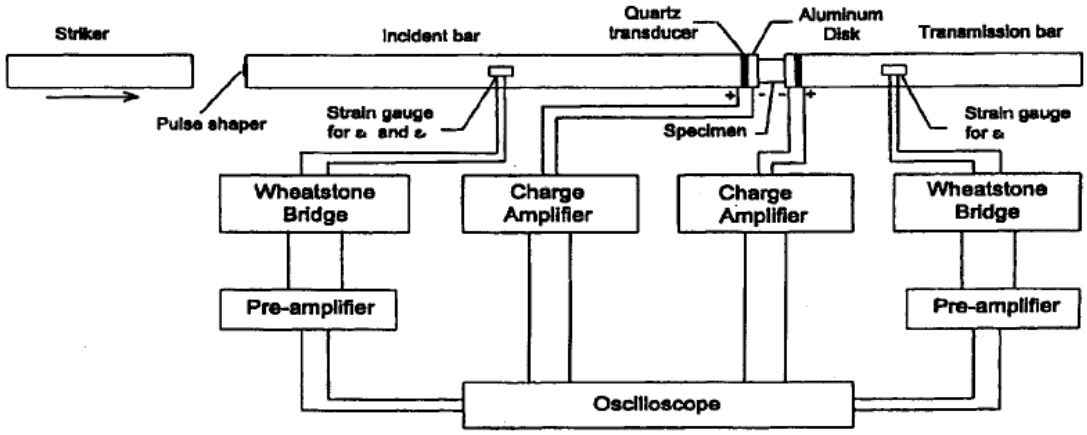

(a)

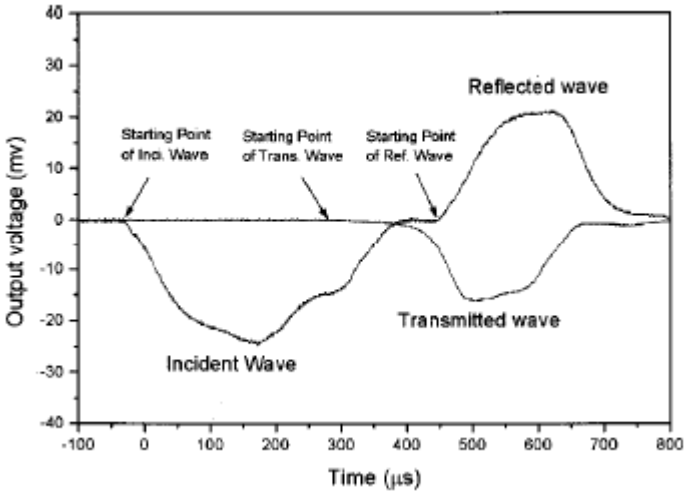

(b)

Figure 3.10 (a) A schematic of the modified SHPB setup for rubber testing; (b) Typical incident, reflected, and transmitted signals from a pulse-shaped experiment with a SHPB modified for rubber testing [111].

Some of our investigated materials, the PTFE-Al-W composites, also have very small strengths (5-100 MPa). The conventional Hopkinson bar method therefore cannot

provide the accurate dynamic response of these materials. To improve the situation, all Hopkinson bar testing of PTFE-Al-W composites was performed using the Hopkinson bar which comprises three 19 mm diameter bars: a 457 mm long Maraging Steel striker bar, a 1828 mm long Maraging Steel incident bar and a 1828 long Magnesium transmitted bar. Because the investigated materials have a lower strength, a low-impedance Magnesium transmitted bar was adopted to obtain low noise-to-signal ratio in transmitted waves.

The equations for calculating strain and stress of the sample on the present special configuration of the Hopkinson bar are as follows.

$$\begin{aligned} \dot{\varepsilon}(t) &= \frac{C_{MS}(\varepsilon_I(t) - \varepsilon_R(t)) - C_M \varepsilon_T(t)}{L} \\ \sigma(t) &= E_M \cdot \frac{A_O}{A} \cdot \varepsilon_T(t) \\ \varepsilon(t) &= \frac{1}{L}\int_0^t [C_{MS}(\varepsilon_I(t) - \varepsilon_R(t)) - C_M \varepsilon_T(t)]dt \end{aligned} \quad , \qquad (3.15)$$

Where C_{MS} designates the sound speed in the Maraging steel incident bar (5000 m/s), C_M the sound speed in the Magnesium transmitted bar (5000 m/s), E_{MS} the elastic modulus of the Maraging steel incident bar (200 GPa), and E_M the elastic modulus of the Magnesium transmitted bar (44.7 GPa). The strain-stress curves were obtained based on the equations.

3.4.2 Hopkinson Bar Shear Testing

The Hopkinson bar was also developed by Hartman et al. [113] and Meyer and Manwaring [114] to characterize the shear zone in a hat-shaped sample (Figure 3.11).

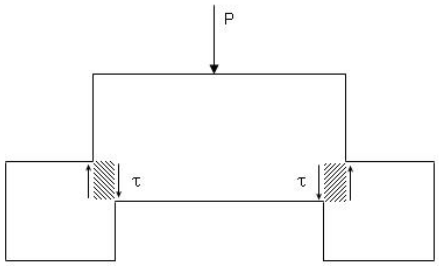

Figure 3.11 Schematic illustration of a hat-shaped sample undergoing Hopkinson bar test with shear zone shown by shaded areas.

Meyers et al. [115] developed the theory of hat-shaped sample. It is considered that the stress state in the plastic deformation region is fairly close to simple shear. The plastic strain is approximately equal to the ratio between the shear displacement d (d is from the top of the hat to where it is stopped) and the thickness of the plastic deformation region, t (t can be measured with optical micrograph, but usually about the difference between the internal and external diameters). Therefore, strain is given by:

$$\gamma = \frac{d}{t} \tag{3.16}$$

The average strain rate in a hat-shaped sample is calculated from the velocity of the incident bar, v, divided by the thickness of the plastic deformation region, t:

$$\dot{\gamma} = \frac{v}{t}. \tag{3.17}$$

The shear stress is equal to the load, *P*, divided by the area of the resisting region, where *di* is the internal and d_e is the external diameter, and h is the height of the area:

$$\tau \approx \frac{P}{\pi h(\frac{d_i + d_e}{2})} \tag{3.18}$$

This approach to observe the shear deformation are comprehensively used in metals [116-119].

3.5 Drop-weight Testing

The drop-weight apparatus has been used for the observation of a variety of aspects related to the dynamic response of a number of materials. With the installation and aid of a AWRE C4 rotating-mirror camera [120] and pressure-measuring technique, it is a straightforward approach to examine the ignition of energetic materials [40,41,121] and the deformation of a number of polymer materials [122,123].

Figure 3.12 illustrates how the drop-weight apparatus works. A weight W (usually in the interval 3 ~ 6 kg) is held at a certain height (0.6 or 1 m in most experiments) above the upper glass anvil by a magnet. At the beginning of a test, the weight drops to the upper glass anvil. Therefore, samples sandwiched between two glass anvils are deformed. The strain gauge or force-transducer on the lower glass anvil captures the voltage-time pulse using a Wheatstone bridge. The data could be later converted into the time dependent force change on the samples.

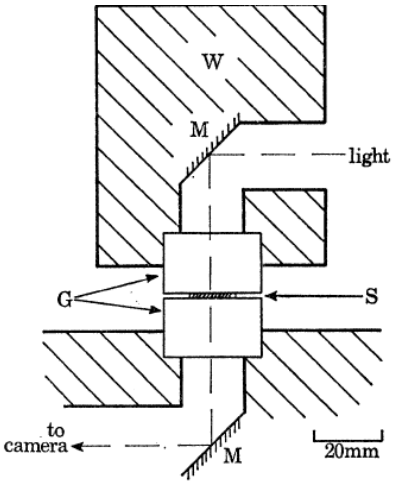

Figure 3.12 Schematic of the high-speed photography drop-weight apparatus. W is the weight, M is the mirror, G is the glass anvils, and S is the sample [121].

Figure 3.13 shows a typical output signal that could be obtained from a drop-weight test. The voltage V varies linearly with force F on the sample with a factor k.

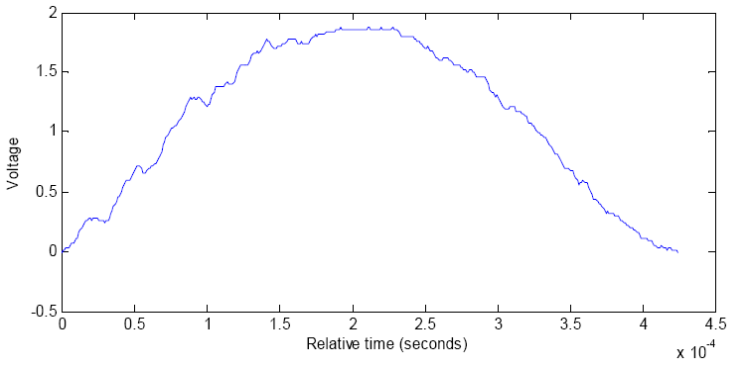

Figure 3.13 Typical voltage-time pulse obtained from a drop-weight test.

A calibration number k (unit N/V) is needed to convert voltage-time data into force-time data. The equation is as follows:

$$k \cdot \int V dt = \int F dt \,. \tag{3.19}$$

According to Newton's Second Law ($F=ma$), the following equation is obtained by integrating it with respect to time:

$$m\Delta v = \int F dt \,. \tag{3.20}$$

The velocity of the dropping weight is monitored when it passes a grating with 2 mm spacing. The photodiode records how long it takes the weight passing the grating. Thus, the velocity can be calculated. By dropping the weight on the anvil without a sample, the calibration number k is therefore calculated.

By using Equations 3.19 and 3.20, a voltage-time trace $V(t)$ could be converted into a force-time trace $F(t)$.

The force acting on the sample is negative. Therefore, the acceleration a is obtained:

$$a(t) = -\frac{F(t)}{m}, \tag{3.21}$$

where $F(t)$ is obtained from Equation 3.19 and m is the mass of the weight.

The velocity change $\Delta v(t)$ at any time t since the impact starts is calculated by integrating Equation 3.21 with respect to time:

$$\Delta v(t) = \frac{\int_{o}^{t} F(t')dt'}{m}. \tag{3.22}$$

The initial velocity of the weight at the moment of impact is v_i, detected by photodiode and calculated by dividing 2 mm spacing.

Thus, the actual velocity of the weight after impact is:

$$v(t) = v_i - \Delta v(t). \tag{3.23}$$

The displacement of the top of the sample *x(t)* is obtained by integrating Equation 3.23:

$$x(t) = \int_{0}^{t} v(t)dt. \tag{3.24}$$

The actual length of the sample at any time t is therefore obtained by subtract x(t) from the initial length l_0:

$$l(x) = l_0 - x(t). \tag{3.25}$$

Then, the engineering strain or the true strain (logarithmic) of the sample can be calculated. There, we consider the true strain:

$$\varepsilon(t) = \ln(\frac{l_0}{l(t)}). \tag{3.26}$$

Note for convenience, now the compression strain is positive.

The true stress $\sigma(t)$ is obtained by dividing the force at the moment *t* by the actual area of the sample:

$$\sigma = \frac{F(t)}{A(t)}, \tag{3.27}$$

in which *F(t)* is obtained from Equation 3.19 and *A(t)* is calculated by:

$$A(t) = \frac{A_0 l_0}{l(t)}, \tag{3.28}$$

in which A_o is the initial area, l_o the initial length and *l(t)* the spontaneous length. Note that it is assumed that the tested sample is incompressible i.e. the volume of the sample does not change during the drop-weight testing procedure. It is valid for solid materials. But if a sample is in the form of powder or a porous material, it will tend to compact at the constant area. Therefore, the engineering stress $F(t)/A_o$ may be a more proper parameter to characterize the loading of the specimen.

Now, a stress-strain curve can be plotted. The strain rate is obtained by finding the gradient of strain with respect to time in the strain-time curve.

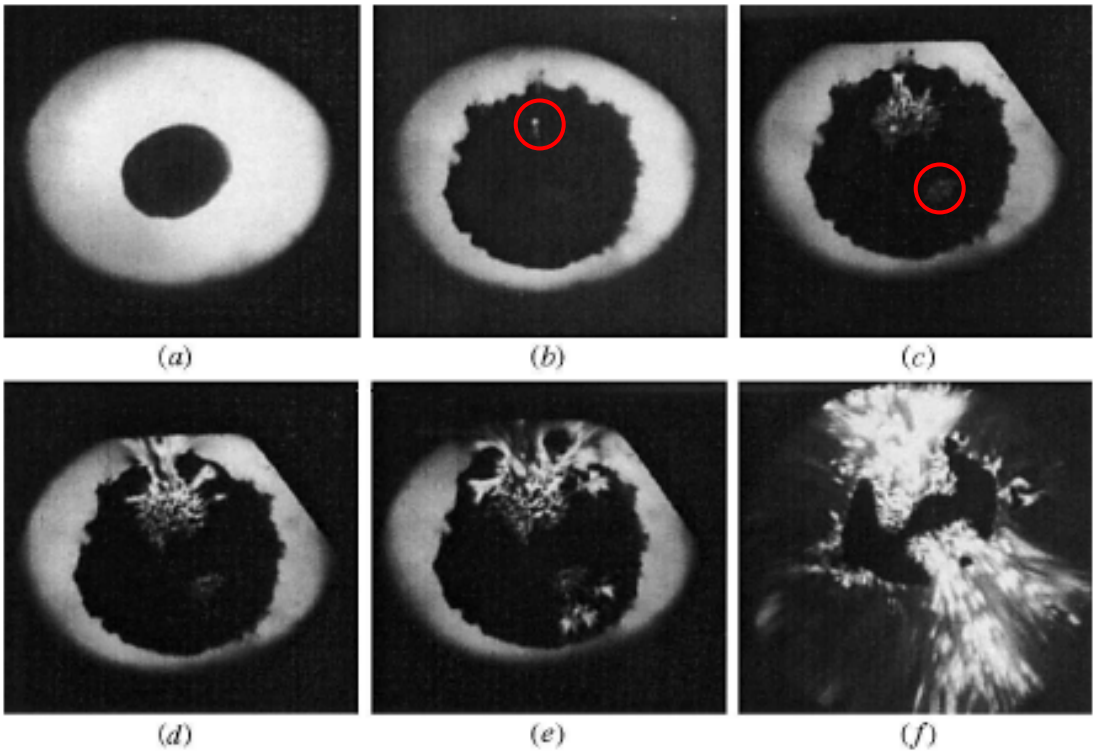

Figure 3.14 Selected frames from the high-speed photographic sequence of the dynamic deformation of a pre-sheared pressed disk of SR 813. Times from the moment of impact for the various figure parts: (a) 0 μs, (b) 329 μs, (c) 343 μs, (d) 350 μs, (e) 357 μs, and (f) 420 μs [37].

For photography, an AWRE C4 rotating-mirror camera was used [120]. It has 140 framing lenses, 5 microseconds per frame interval, giving a total recording time of approximately 1 milliseconds. The duration of the light flash was fixed at 500 microseconds, less than the period of rotation of the mirror (700 microseconds), so that double exposure on the camera film was avoided. The records were used to probe the localization of failure in unconfined samples and to provide the evidence of reaction. Figure 3.14 shows the consequence of a high speed rotating camera recording the whole reaction process after impact from ignition to full consumption of the reactants of a

thermite reaction of 40% Al and 60% KClO4 [37]. The first ignition size can be seen in Figure 3.14 b (in the red circle) and this ignition propagated in Figure 3.14 c. The second ignition size can be seen in Figure 3.14 c (in the circle) and this ignition propagated in Figure 3.14 d and e until the whole sample was consumed.

3.5.1 Standard Drop-weight Testing

In the research, the polymeric composites have a lower strength than those of most metals. Therefore, the output signal from the standard method has oscillation whose amplitude is close to that of true signals produced by the sample's deformation. It could be explained that the by the inevitable vibrations in the system caused by impact. Because the sample materials are weak, it would take longer time to reverse the momentum of the weight and stronger samples. Figure 3.15 showed the output signal from a densified PTFE-Al-W sample containing coarse W particles.

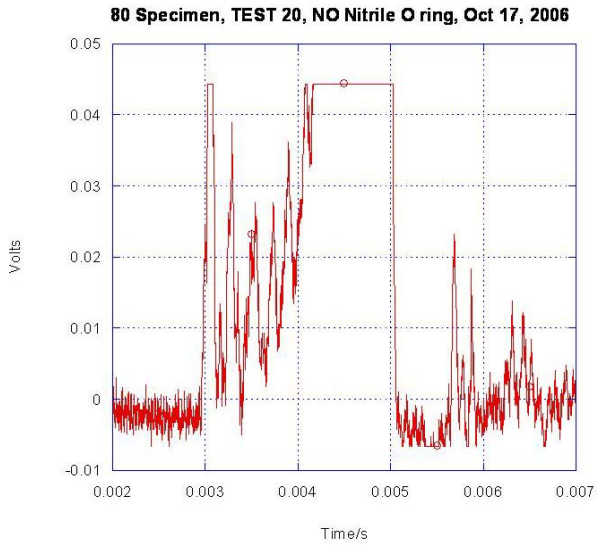

Figure 3.15 Output signal for a PTFE-Al-W composite sample containing coarse W particles tested in a conventional drop-weight experiment.

A typical oscillogram from an experiment with a coarse PTFE-Al-W composite sample containing coarse W particles in a standard drop-weight test showed large amplitude oscillations comparable or even larger than signal (Figure 3.15). The oscillation of signal trace presents a challenging task to extract the useful information in this case. The signals accompanied by such oscillations were almost impossible to interpret. To decrease such oscillations caused by the facility itself, a modification was proposed.

3.5.2 "Soft" Drop-weight Testing

To overcome the intrinsic oscillation associated with the conventional drop-weight setup, a Nitrile o-ring (BS201NI70) was placed on the top of the impact surface (Figure 3.16) to reduce the mechanical oscillations in the system caused by impact of the mass to the upper anvil. This is termed as “soft” drop-weight setup.

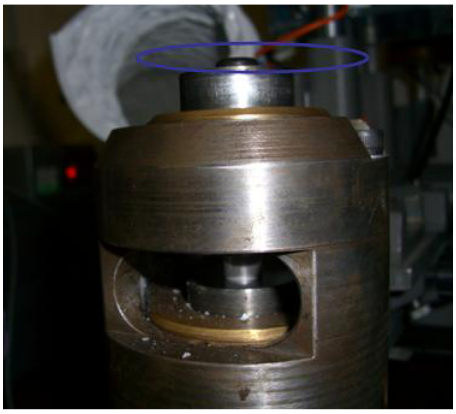

Figure 3.16 Polymer o-ring (black in the circle) was placed on the top of the upper anvil to mitigate parasitic oscillations.

Compared to Figure 3.15, Figure 3.17 shows the signal of a sample, which had the identical components and geometry as the one represented by Figure 3.16, from this “soft” drop-weight setup. This approach was proved effective (Figure 3.17). It is obvious that traces exhibit much less oscillation than with conventional testing.

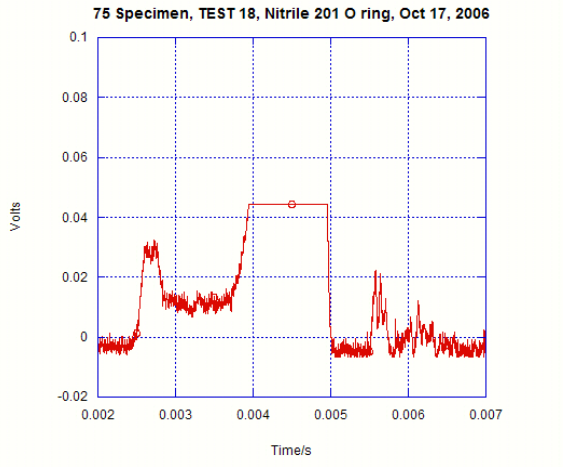

Figure 3.17 Output signal for a densified PTFE-Al-W composite sample containing coarse W particles tested in a "soft" drop-weight experiment exhibited much less oscillation than the data in Figure 3.15.

To validate that the introduction of the o-ring does not change the explanation of the signal trace for the "soft" drop-weight experiments, the o-ring itself was tested by the conventional method with various dropping height of the weight, 50 cm, 80 cm, and 112 cm. The results in Figure 3.18 show that the o-ring deformation is almost strain-rate independent in the range investigated. So, the deformation of the o-ring at a given force can be subtracted to give the precise deformation information of the tested sample.

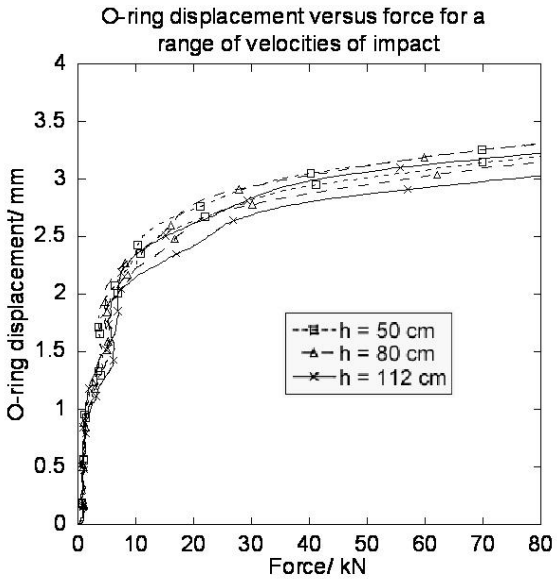

Figure 3.18 O-ring deformation for a range of velocities of impact showing its insensitivity to strain rate [124].

To further verify the "soft" drop-weight technique, it was used on commercial sintered PTFE samples, which were considerably stronger than the CIPed consolidated PTFE–Al-W samples. Comparing the stress-strain curves obtained with conventional and modified drop-weight tests shows good agreement (Figure 3.19). This suggests that the error in the strains calculated from modified tests is less than 10%.

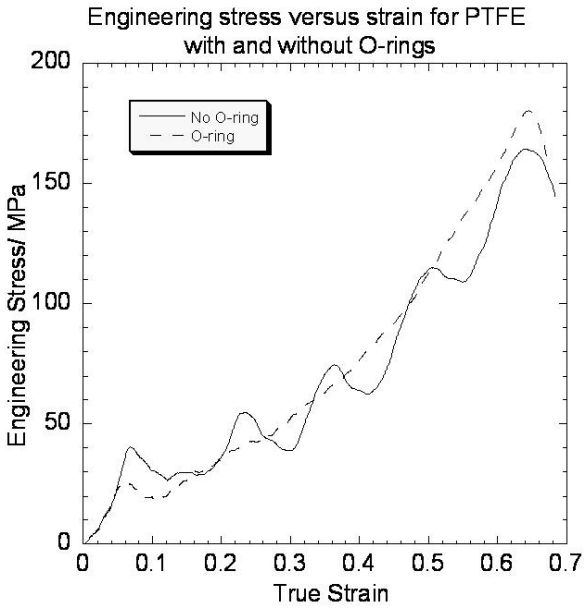

Figure 3.19 Comparing the stress-strain curves obtained with conventional and modified drop-weight tests on commercial PTFE samples [124].

3.6 Thick-walled Cylinder (TWC) Testing

The thick-walled cylinder technique was [125,126] developed to investigate the high-strain, high-strain-rate deformation and shear band patterning of inert and energetic materials. It has been extensively used in the studies of reactive porous materials (Nb+Si, Mo+Si+$MoSi_2$ [127,128], Ti-Si [129]), granular alumina [130], Ti and its alloy [131-133], stainless steel [133,134], Fe-Cr-Ni [135]. Figure 3.20 describes the details of sample setup in a TWC test. Detonation is initiated at the top of the cylinder and propagates along the cylinder axis.

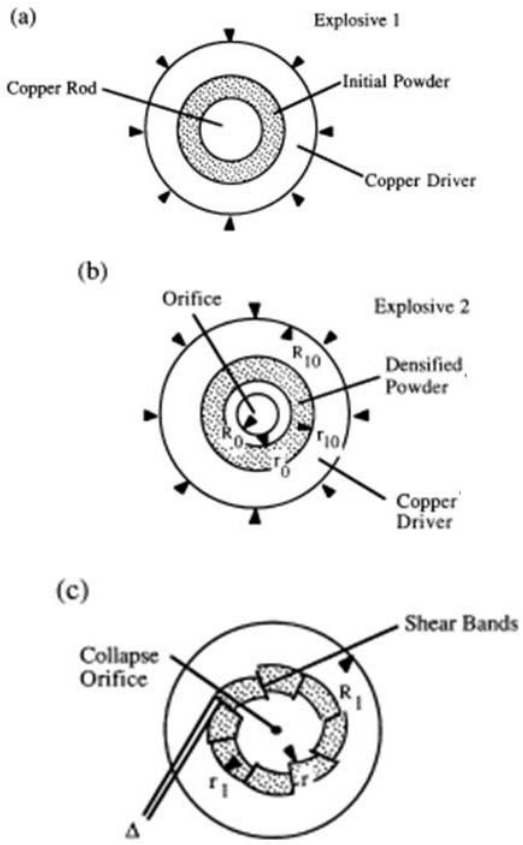

Figure 3.20 Geometry and sequence of deformation events in thick-walled cylinder method: (a) initial geometry, densified by explosive 1; (b) densifid powder with central orifice cylinder collapsed by explosive 2; (c) final geometry. [129]

The initial powder was placed in the tubular cavity between the copper rod and the copper drive (Figure 3.20a). The powder was consolidated by the explosive 1. After that, an orifice was drilled along the longitudinal axis in the center copper cod to form another tube (Figure 3.20b). A second explosive occurs to collapse this whole cylinder system to produce significant plastic deformation on the densified powder (Figure 3.20b).

3.6.1 Standard Method Testing

Explosively driven TWC tests were conducted according to the previously described set-up using a copper stopper and driver tubes [74]. Typical sizes of solid PTFE samples for explosively driven TWC test were 14 and 21 mm (inside and outside diameters) with a length 62.3 mm. They were fitted into a copper tube with an outside diameter of 31 mm. The inner and outer diameters of the copper stopper tube were 12.5 mm and 14 mm. This standard test usually require about 1 kg of explosive and can be done in conditions of special proving grounds or in explosive chambers which usually are not available in a university environment.

3.6.2 Small-scale Hopkinson Bar Assisted TWC Testing

Modified thick walled cylinder tests were conducted using the compression Hopkinson bar, which is available in a university environment. This method allows monitoring of the kinetics of collapse by introduction gauges on the surface of the chamber. One of two strain gages was placed along the periphery direction to control pressure in the chamber is shown in the circle (Figure 3.21). The ruler is shown in the right. The screw to seal the filling hole is on the bottom.

Figure 3.21 Actual chamber for dynamic collapse of simulant materials

The typical size of samples in this test were much smaller (inner diameter 4.3 ~ 5.5 mm, outside diameter 10 mm) than in the explosively driven TWC test. In the Hopkinson bar based TWC test we were not able to collapse solid PTFE samples in copper driver and stopper tube due to a relatively smaller pressure level. For this reason samples were jacketed using a low strength soft polymer driver tube made from TYGON R-3603 with 10mm and 13mm inner and outer diameters (Figure 3.22).

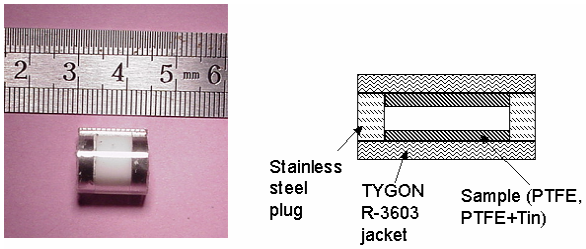

Figure 3.22 Schematic set-up (right) for the sample shown on the left.

Two stainless steel plugs with a thickness of 3 mm and diameter 10 mm were placed on both sides of the sample to prevent water from entering the inner cavity. This

type of jacket allowed us to initiate the collapsing process in solid PTFE ensuring soft recovery of heavily deformed samples. In a PTFE-Sn mixture, there was complete collapse. It is important that this encapsulation provided a radial motion of the material with a negligible axial strain of 0.007.

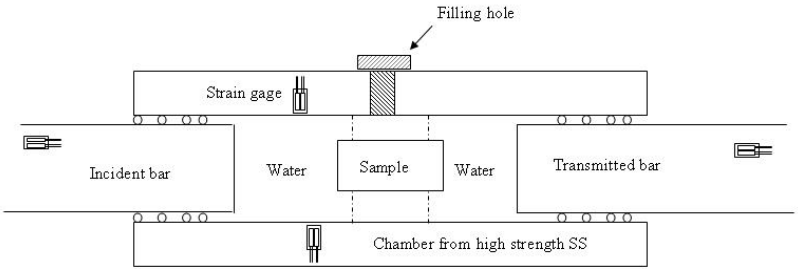

(a)

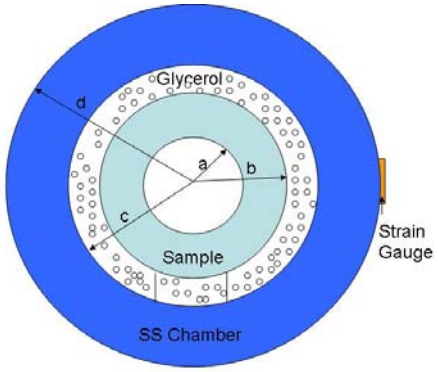

(b)

Figure 3.23 Schematic illustration of the experimental set-up for collapse of cylindrical sample (modified TWC test) in Hopkinson bar: (a) front view; (b) cross-sectional view of the chamber with a sample inside. Various diameters: a=2.55mm, b=5.25mm, c=9.55mm, and d=22.5mm.

After the sample was encapsulated by the polymer tube and stainless steel plugs, it was placed in the chamber in Figure 3.21. The sample was held by a pair of thin layer of hard plastic ring-shaped sheets (dash lines in Figure 3.23a) to keep it in the middle of

chamber. The incident bar and the transmitted bar were inserted before the pressure transmitted liquid, such as water in Figure 3.23a and glycerol in 3.23b, was dripped into the chamber through the filling hole. Finally, a screw sealed the hole. From the side view of the chamber in Figure 3.23b, it can be seen that the outer diameter of the chamber is 22.5 mm, the inner diameter 19.55 mm which is the size of the Hopkinson bar diameter, the outer diameter of the sample is 5.55mm, and the inner diameter of the sample is 2.55mm.

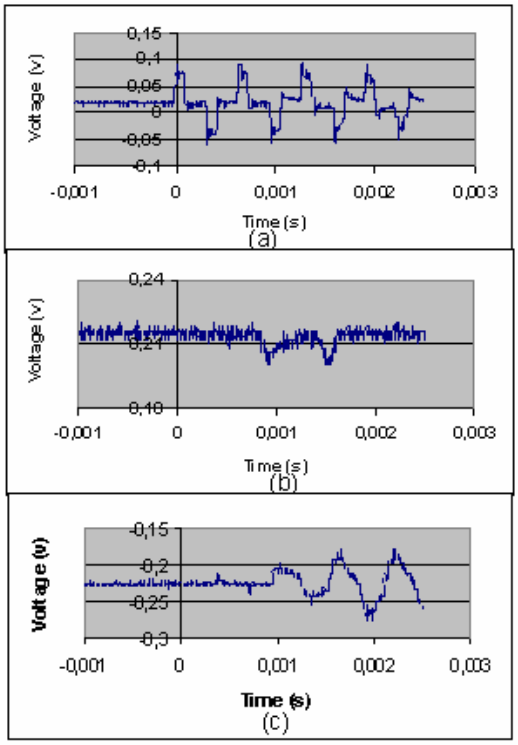

Figure 3.24 (a) Impulses in the incident bar; (b) only two impulses with pressure 100 MPa are detected in the chamber wall; (c) impulses in the transmitted bar.

The Hopkinson bar based TWC test allowed monitoring of the pressure history in the chamber using gages on the transmitted bar and on the wall of the chamber. The

typical record of the pulses in the incident bar, in the outside wall of the chamber and in the transmitted bar are shown in Figure 3.24. It is evident that two main pulses with similar amplitudes and durations of 300 – 400 microseconds were generated in the chamber based on the measurements on the outside surface of the wall.

Different liquids were used as driving media in the sample's chamber to ensure a controlled pressure in the chamber with small displacement of the incident bar: (a) water, (b) suspension of alumina particles, 20% by volume, in water with overall density 1.6 g/cm^3, particle size less than 10 μm (ALDRICH) (c) Glycerol (EMD, GR ACS, density 1.26 g/cm^3). The typical pressure pulses in the chamber filled with different liquids (with no sample inside) detected by gauges on the outside surface are shown in Figure 3.26. They were generated by an impact with a 254 mm-long, 19 mm-diameter striker bar with a velocity of 14 m/s. The ideal pressure transmitted liquid should have a small compressibility which will ensure a larger pressure in the chamber with a small displacement of the incident bar. The compressibility of water, alumina suspension in the water, and glycerol are equal to $45.8 \cdot 10^{-11}$ Pa^{-1}, $36.7 \cdot 10^{-11}$ Pa^{-1}, and $21 \cdot 10^{-11}$ Pa^{-1} [136]. At the similar striker velocity, the largest pressure was achieved with glycerol (Figure 3.25c) due to the smallest compressibility of this liquid.

The time of the pulse reverberation inside the chamber, when the length of the cavity filled by liquid equals 22 mm, is about 30 microseconds for water (sound speed C_0=1500 m/s), 34 μs for the suspension (C_0=1300 m/s) and 23 μs for glycerol (C_0=1904 m/s). This reverberation time is causing a step-like increase of the stress in the

transmitted bar. It is less noticeable in the measured stresses on the outside wall of thick walled chamber.

Comparison of averaged pressure in the chamber and its duration based on stresses on its surface and stresses in the transmitted bar demonstrated a reasonable agreement.

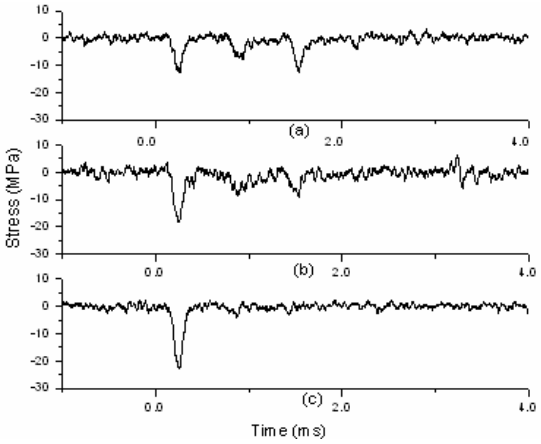

Figure 3.25 The stresses detected by the strain gages on the chamber wall with different liquid medium inside: (a) Water, (b) Alumina suspension in the water, (c) Glycerol.

The higher speed of sound in glycerol facilitates smoother increase of pressure that creates higher stress amplitude. The total duration of the pulses is about 200-250 μs, which is significantly longer than reverberation times and do not depend significantly on the nature of the liquids inside.

3.7 Scanning Electron Microscopy (SEM)

Microstructures of the initial surface and the fracture surface (recovered from quasi-static, ECAP, Hopkinson bar, and drop-weight tests) of samples were analyzed and studied using a FEI XL30 Environmental Scanning Electron Microscope in CalIT^2, UCSD and a FEI Quanta 600 in SIO, UCSD. These microstructures investigation was intended to to help understand the failure mechanisms and microstructural evolution of sample undergoing high-strain, high-strain-rate deformation.

FEI XL30 and FEI Quanta 600 both are multipurpose SEMs that provide electron imaging at variable pressures. Low vacuum environment in the chamber offers charge free analysis of potentially problematic samples for conventional high vacuum SEMs at high resolution, such as non-conductive and hydrated samples. The microscopes are also equipped for Energy Dispersive X-ray analysis (EDX) to qualitatively and quantitatively identify the elemental composition of the sample or an area of interest.

Secondary electron images provide high-resolution topographical feature of samples, while backscattered electron images provide more information on the elements, brighter regions representing heavier elements (higher atomic number Z) and darker regions lighter elements. Secondary electron imaging utilizes inelastic electron scattering caused by the interaction between the electrons from samples and the incident electron beam to generate the emission of low-energy electrons from near the sample's surface [137]. How many of electrons actually reach the detector determines how much topographical information a secondary electron image could provides. When the incident electron beam arrives at the edges of topographically high portions of a sample at lower

angles, more energy is deposited into the volume of secondary electron production. Thus, high edges yield more secondary electrons, generating a larger detected signal. The orientation of surface features also play an important role on how many electrons reach the secondary electron detector, which creates variations in image contrast that represent the surface topography of a sample. Electrons backscattered from the nucleus of an atom (the larger the nucleus, the more the electrons that are backscattered) are produced by the elastic interactions between the sample and the incident electron beam [137]. These high-energy electrons usually escape from much deeper regions of the sample than secondary electrons, so surface topography is not as accurately resolved by them as by secondary electrons. The efficiency of production of backscattered electrons is proportional to the sample's material's mean atomic number Z, resulting in image contrast as a function of composition -higher atomic number material appears brighter than low atomic number material.

The top of the initial pressed samples and the fracture surface of the non-conductive (polymeric composites) sample after testing were polished, and deposited with ~1 μm thick Au using Denton Discovery 18 Sputter System at CalIT^2, UCSD. Secondary electron and back-scattered electron images were collected using SEMs thereof. EDX analysis was employed to collect elemental analysis on the samples.

3.8 Raman Spectroscopy

Raman spectroscopy was employed to detect the composition of the dynamically tested samples to determine whether new chemical composition appeared. Raman spectroscopy is a spectroscopic technique used in condensed matter physics and chemistry to study vibrational, rotational, and other low-frequency modes in a system [138]. It relies on small-energy inelastic scattering, or Raman scattering of monochromatic light, usually from a laser in the visible, near infrared, or near ultraviolet range. When laser light interacts with the electron cloud of the bonds of that molecule, Raman scattering occurs and can be detected by the spectroscope. In chemistry, vibrational information is very specific for the chemical bonds in molecules. Thus, Raman spectroscopy provides an accurate message which molecule is identified.

In the research, the Raman spectra of initial and collapsed samples were collected on a Renishaw Raman Spectometer with a Melles Griot laser. The 514.5 nm excitation line was chosen with an incident power varying from 10 mW to 25 mW.

CHAPTER 4

RESULTS AND DISCUSSION

In the research, a range of various heterogeneous materials were investigated. In this chapter, the results of the work are presented. Section 4.1 introduced the PTFE-Sn material followed by Section 4.2 in which the PTFE-Al material was presented. Most of the research was being focused on the investigation of the PTFE-Al-W material whose details is brought by Section 4.3. Besides the works related to the polymeric composite, a part of the research was concentrated to the carbon-fiber-filled Al alloy. It is in Section 4.4.

4.1 PTFE-Sn Composites

PTFE (polytetrafluoroethylene) has an excellent combination of electric and mechanical properties that make it suitable for many applications [139]. This material is also one of components of energetic mixtures [140-144]. Very few studies have been made of testing and modeling of dynamic behavior of solid PTFE [145-150], including initiation and patterning of shear bands [74].

The main goal of the research is to develop experimental tests which will be adequate for establishing the critical conditions for the start of shear induced instability in

non-traditional energetic matierals (like PTFE/Al). It is important to develop experimental tests that allow the investigation of the mesomechanical features of deformed materials (including area of localized shear bands) inside the initiation threshold (like for Ti-Si mixtures [74]). It is also desirable to generate an array of self-organized shear bands under controlled boundary conditions and to identify the major mesomechanical mechanisms of softening (hardening) which may destabilize uniform plastic flow (or stabilize and mitigate shear localization).

Commercially available solid PTFE samples with density 2.11 g/cm^3 (corresponding to crystallinity about 38% [139]) were used in our experiments for comparison

Shear instability and patterning of shear bands in PTFE and in its mixtures with Sn particles were studied using explosively driven and newly developed small scale Hopkinson bar based thick walled cylinder (TWC) methods. The mixture of PTFE and Sn is considered as an inert material, which was used on the first stage of the research to develop experimental techniques. Currently available theoretical models of shear instability and spacing between shear bands are based on a thermal softening mechanism which apparently does not account for the beginning of shear instability in PTFE [151]. Critical effective strain at strain rate 10^4 s^{-1} for propagation of shear bands in PTFE under plane strain conditions was equal to 0.4 and shear band spacing for the initial stage of shear localization was 0.5 mm. In the Hopkinson bar based TWC test shear instability, in a form of a group of small number of shear bands, starts at overall strain on inner surface above 0.22 and causes a break of cylindrically

symmetrical motion of material. Contrary to the behavior of solid PTFE, its mixture with Sn particles is more stable with respect to shear localization.

4.1.1 Thick-walled Cylindrical (TWC) Testing

Explosively driven TWC tests of the densified PTFE-Sn samples were conducted. Different cuts of the sample after this test with pattern of shear bands are shown in Figures 4.1. The pattern of multiple shear bands developed from the inner surface with intact cylindrical geometry of the outside. Copper driver and stopper tubes are not shown in Figure 4.1b. The vertical cut was made outside the stopper tube. After TWC test (Figure 4.1a) planes of shear localization are running parallel to the sample axis (vertical direction in Figure 4.1b). This means that material flow after instability start is of plane strain. About 50 shear bands with spacing 0.5 mm were developed; critical effective strain for shear band propagation is about 0.4. Global strain rate is about 10^4 s^{-1}.

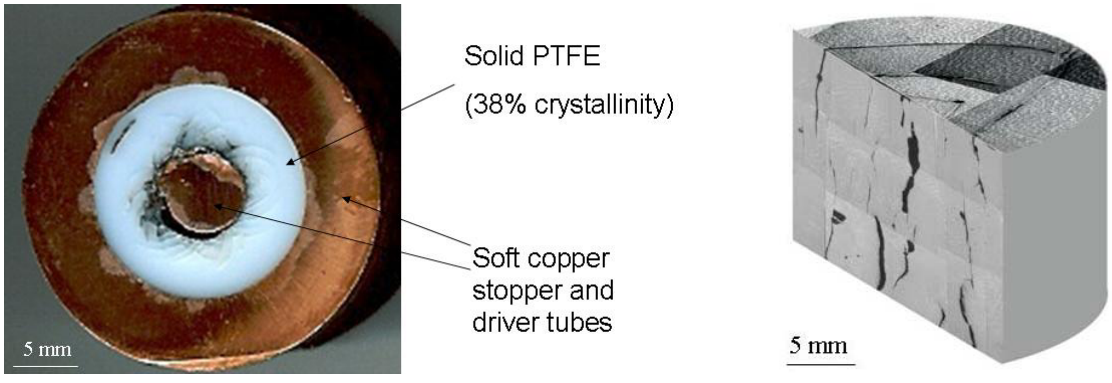

(a) (b)

Figure 4.1 (a) Explosively tested solid PTFE sample; (b) Shear bands in horizontal and vertical planes corresponding to the sample shown (a).

4.1.2 Small-scale Hopkinson Bar Assisted TWC Testing

Samples after Hopkinson based TWC tests are presented in Figure 4.2 (solid PTFE) and Figure 4.3 (PTFE-Sn mixture). The initial PTFE sample had a 4.3 mm inner diameter and 10 mm outer diameters (Figure 4.2a). The stable deformation of the sample with size (Figure 4.2 a) in the TYGON R-3603 jacket, which had a10 mm and 13 mm inner and outer diameters, was observed. The effective strain is about 0.22 on the inner surface. Unstable deformation due to local shear instability of sample with larger inner (5.5 mm) diameter in the same jacket as in the Figure 4.2b was noticed. The shear bands (Figure 4.2d) in the sample which had a larger inner diameter (Figure 4.2c) were distinctive.

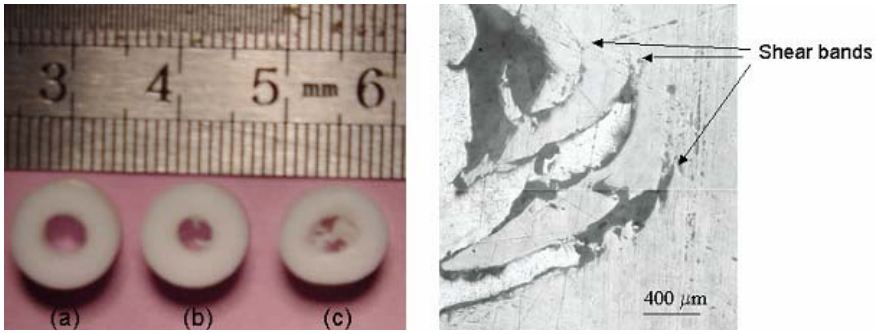

Figure 4.2 (a) Initial PTFE sample; (b) Stable deformation of sample with size (a); (c) Unstable deformation due to local shear instability of sample with larger inner (5.5 mm) diameter in the same jacket as in (b); (d) three shear bands in the sample (c) corresponding to the area with a smaller radius in the collapsed sample (there are two such areas opposite to each other).

In contrast with solid PTFE sample of similar size only one shear band was detected in PTFE-Sn mixture under similar conditions of dynamic loading in Figure 4.3. Therefore, we could conclude that the PTFE-Sn was more stable than the PTFE in terms of shear localization.

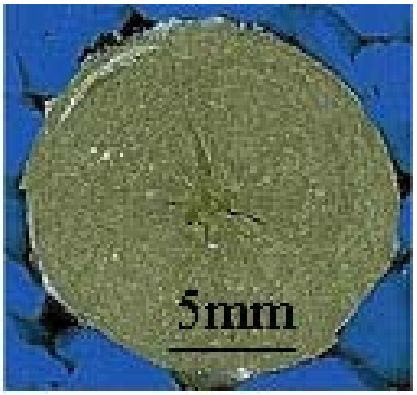

Figure 4.3 Sample of PTFE (54 wt%)+Sn (46 wt%) was completely collapsed in mostly cylindrically symmetrical shape and fractured by radial cracks.

4.1.3 Discussion and Conclusions

Thermal softening is a typical shear instability mechanism for metal and alloys. Thermal softening leads to shear instability when it outweighs strain-hardening, namely the ratio B exceeds 1 [152]

$$B = \tau \left|\partial\tau/\partial T\right| / (\rho C \partial\tau/\partial\gamma) > 1. \quad (4.1)$$

The following parameters for solid PTFE were taken based on data in [145], shear strength τ = 70 MPa, decrease of shear strength (thermal softening) $\Delta\tau$ =−15 MPa corresponding to ΔT = 16 K (evaluated based on complete conversion of mechanical

work into heat), density of solid PTFE ρ = 2100 kg/m^3, heat capacity C = 1020 J/kg K, $\Delta\tau$ = 45 MPa corresponding to a strain hardening at the tip of shear band ($\Delta\gamma$ = 0.4) in explosively driven TWC test. Evaluation of B gives B = 0.27 < 1. Therefore thermally induced instability can not explain observed nucleation of shear bands or development of a pattern of shear bands in PTFE. Based on this analysis and microstructural observations (Figure 4.4) it was suggested that strain softening, most probably crazing, is the main mechanism in initiation of shear bands in explosively driven TWC test. This athermal behavior of solid PTFE is similar to the observed in polycarbonate and polymethyl methacrylate [153].

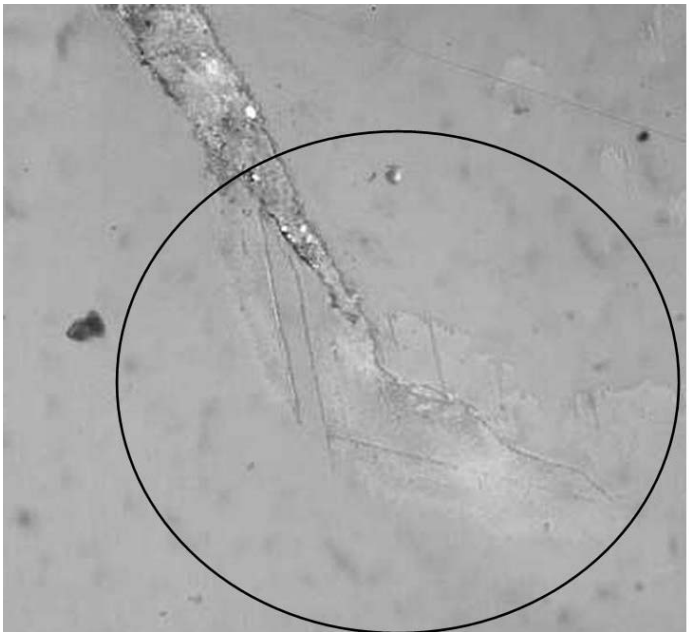

Figure 4.4 Crazing in the tip of shear band in solid PTFE (area close to the tip is shown by circle).

Cylindrically symmetrical collapse of samples in the Hopkinson bar based TWC test resulted in high strain (estimated strain rate about $10^3 \sim 10^4$ s^{-1}), plane strain (pure shear) deformation with negligible axial strain (0.007). The solid PTFE sample was symmetrically collapsed with the effective strain 0.22 on the inner surface without developed shear instability, and after, exhibited a loss of cylindrical symmetry due to local shear instability. This is in agreement with data for an explosively collapsed PTFE sample where critical strain for localized shear propagation was 0.4.

Cold isostatically pressed PTFE-Sn samples are more stable with respect to shear localization than solid PTFE and were collapsed almost symmetrically. They demonstrated brittle radial cracks probably caused by tensile stresses on unloading (Figure 4.3). The observed stability of a PTFE mixture with Sn may be due to a lack of strain softening (crazing) in this material. It can be attributed also to a lower strength of pressed PTFE and heat conductivity into metal particles which hinder thermal softening. Strain hardening caused by initial porosity and subsequent densification during plastic deformation can be an additional reason for stability of high strain plastic flow of this mixture.

4.2 PTFE-Al Composites

In Section 2.3, the properties of the mixture of PTFE and Al were introduced. A mixture of PTFE and Al powders was selected because Al could react with PTFE and release a large amount of energy when forming AlF_3 or AlF_4 [154]. The theoretical

energy content of the mixture of 26.5 wt% Al powder is 3380 cal/g (Table 1)[1]. It can be seen that the huge amount of energy of PTFE-Al is a major reason for selection of this materials as a prime candidate for reactive materials.

Table 4.1 The theoretical energy content of a range of polymer/metal composites [1]

Material	Loading (% by mass)	Binder	TMD (g/cm^3)	Theoretical Energy Content (cal/g)
Al-PTFE	26.5/73.5	PTFE	2.4	3380
Zr-THV	52.0/48.0	THV	3.1	2340
Ta-THV	74.0/26.0	THV	5.3	1755
Hf-THV	69.0/31.0	THV	4.6	1515

The athermal mechanism of strain softening, instead of thermal softening typical for metals, causes the initiation and subsequent patterning of shear bands observed in the explosively driven collapse of PTFE cylinders [74] and in Hopkinson bar based tests with samples of smaller size [151]. The dynamic shear localizations in polycarbonate and polymethyl methacrylate also exhibited similar behavior [153].

The creation of a hot spot by the oxidation of Al particles in Teflon AF led to shock-induced decomposition into monomers [155] and resulted in the condensation of carbon [142]. Dienes [156] analyzed four hot spot mechanisms: void collapse with a closing shock, void collapse with uniform, nonlocalized plastic flow, shear banding with plastic flow, and shear cracking with frictional heating as mechanisms of detonation observed when propellant cylinders were fired at low speeds against a steel plate. He

proposed that interfacial heating due to friction inside closed cracks is the most likely mechanism of XDT detonation observed below critical velocity characteristic for Shock to Detonation Transition.

Here results of experimental tests which allow characterization of the critical conditions for the start of shear induced instability in non-traditional (like PTFE-Al or their simulants) heterogeneous materials are presented. The method generates an array of self-organized shear bands under controlled boundary conditions and allows the identification of the major mesomechanical mechanisms of softening of heterogeneous reactive materials which may destabilize uniform plastic flow. A different diameter of Al particles in the mixture was used to determine the influence of metal particle size on the initiation of shear instability, shear band patterning and chemical reaction.

The Hopkinson bar based thick walled cylinder (TWC) method was developed to collapse hollow cylinders with a small mass of about 0.5 grams made from the mixtures of PTFE and Al particles of different sizes (2 and 95 μm). In section 3.6.2, different media (water, suspension of alumina particles in water, and glycerol) were introduced to ensure the collapse of hollow cylinders with a single pressure pulse under pressure/time conditions achievable in Hopkinson bar tests. Glycerol was the best choice. In this section, the Hopkinson bar assisted TWC tests were all carried out with glycerol as the pressure transmitted medium. Raman spectroscopy of the samples of PTFE and 2 μm aluminum particles mixtures demonstrated the evidence of the decomposition or reaction of PTFE inside the shear localization area or cracks.

The inner and outer diameters of the hollow cylindrical samples of high-density, high accuracy PTFE-Al (76wt% and 24wt%, respectively) composite samples were 4.8 mm and 10.4 mm respectively. The weight varied from 0.5 to 1 g

4.2.1 Small-scale Hopkinson Bar Assisted TWC Testing

The Hopkinson bar based test allowed monitoring of the pressure history in the chamber using gages on the transmitted bar and on the outside wall of the chamber. The detected pulses are shown in Figure 4.5 for an experiment of a PTFE-2μmAl sample with a height of 2.97 mm. This sample was totally collapsed and shattered. Other samples in a similar condition of loading were also almost completely collapsed, but were held together by the polymer holder. They usually had a few radial and spiral cracks (shear bands) (Figure 4.6).

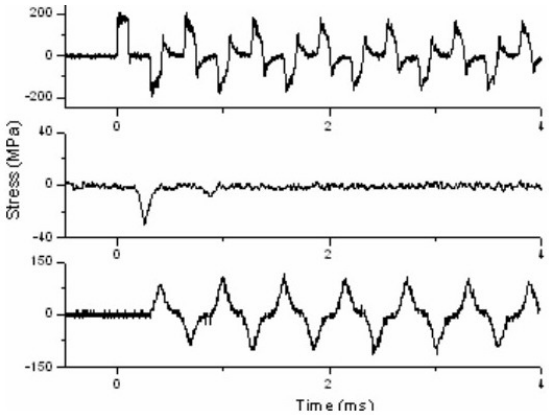

Figure 4.5 Stress detected from a Hopkinson bar assisted TWC experiment of a PTFE-2μmAl sample: stresses in the incident bar (top), one main stress peak in the chamber wall corresponding to pressure 100 MPa inside the chamber (middle), and stresses in the transmitted bar (bottom).

The cylindrically symmetrical collapse of samples in the Hopkinson bar based TWC test was observed with negligible axial strain (0.007). The estimated radial strain rate was about $10^3 \sim 10^4$ s^{-1}. The solid PTFE sample was symmetrically collapsed with an effective strain of 0.22 on the inner surface without developing shear instability [151]. The start of shear instability at larger strain resulted in a loss of cylindrical symmetry. This is in agreement with data for an explosively collapsed PTFE sample where critical strain for localized shear propagation was 0.4 [74,151].

Figure 4.6 The nearly collapsed sample from the mixture of PTFE and 2-μm Al in polymer jacket. Note the characteristic four cracks/shear bands.

4.2.2 Raman Spectroscopy

In totally collapsed samples, black, flaky residues were observed (Figure 4.7) in areas adjacent to the cracks/shear bands. The Raman spectra of the original samples before testing, black solid chunks and black flaky residues after testing (Figure 4.8) show the decomposition of PTFE in the latter. The peaks in the samples before testing and in the black solid chunks after testing are the same, indicating no reaction. New sp2 and sp3

peaks from the black flaky residues verify the decomposition of PTFE into graphitic carbon. No lines in the Raman spectra of the black flaky residue corresponded to AlF_3 (or other similar compounds).

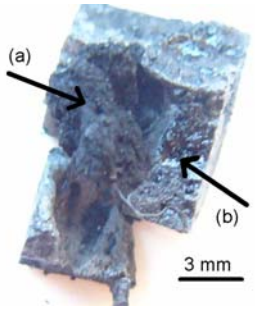

Figure 4.7 Part of collapsed sample in experiment with PTFE/Al particles with 2–μm diameter. Surfaces on the left and right correspond to the initial side of the sample. (a) Black flaky residue identified as graphitic carbon; (b) solid black chunk with the same composition as the sample before testing.

The black residue was also observed in laser initiated reactions in Teflon^{AF} (Dupont Teflon, Amorphous Fluoropolymer which is composed of the chemical monomers tetrafluoroethylene and a dioxole monomer) and its mixture with nanoparticles (500 nm diameter) of Al [142]. Raman spectra of the Teflon AF and Teflon AF/Al samples indicate that the recovered opaque material is graphitic carbon. The proof of the reaction was based on the change of the diameter of Al particles measured using time resolved absorption spectroscopy.

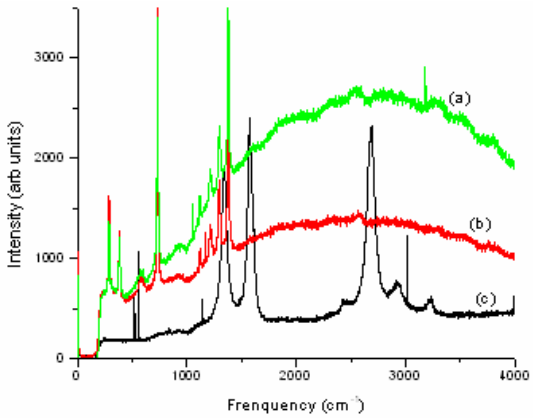

Figure 4.8 The Raman spectra of (a) original samples before testing, (b) solid black chunks after testing, and (c) black flaky residues after testing.

The black flaky residue was not observed in pure PTFE, in the mixture of PTFE and 95 μm Al particles or in the mixture with Sn particles under the same conditions of deformation. This behavior strongly indicates that the observed phenomenon is due to the reaction of PTFE and 2 micron size Al particles inside the shear zone or on the sliding sides of cracks during collapse of hollow cylindrical samples. The reaction did not propagate into the bulk of the sample, being restricted to the area adjacent to a shear band or crack.

4.2.3 Discussion and Conclusions

CIP (Cold Isostatic Press) based method was used to prepare high-accuracy small cylinders (mass about 0.5 g) from PTFE and Al particles. The dynamic collapse of solid PTFE/Al samples with different particle sizes was accomplished with the localized shear

bands and cracks in Hopkinson bar assisted TWC tests in which glycerol functioned as the pressure transmitted medium. The mechanism of the shear localization phenomenon was athermal. Only samples with 2 μm Al particles demonstrated a black flaky residue which was identified using Raman Spectroscopy as carbon. This phenomenon was not detected under collapse of cylinders made from pure Teflon or from mixtures of PTFE and large aluminum particles or in mixtures of PTFE and Sn particles, indicating that the reaction between PTFE and 2 μm Al particles was initiated inside the shear band (crack). It did not propagate into the rest of the sample.

4.3 PTFE-Al-W Composites

This section presents high strain-rate mechanical and microstructural properties of a composite system consisting of Teflon (PTFE), aluminum (Al) and tungsten (W) particles, with a density up to 7.2 g/cm^3. Al powder contains spherical shape of Al particles. The W powder contained irregularly shaped particles. The particle size of each powder is summarized in Section 3.1. The addition of W particles was necessary to increase the density of samples, the level of g/cm^3 required in the applications.

Samples with different sizes of W particles were prepared to investigate the effect of particle size on the density (ρ) and the ultimate compressive strength (σ_f) of the materials. Three types of samples with the same weight content of components were prepared and studied to understand the particle size effect: porous samples containing fine W particles (ρ = 6 g/cm^3), porous samples containing coarse W particles (ρ = 6

g/cm^3), and samples containing coarse W particles with a density close to the theoretical value (ρ = 7 g/cm^3). The first and the third type of samples were pressed under hydrostatic pressure of 350 MPa. The second type was pressed at 20 MPa to introduce the same porosity into the samples containing coarse W particles as in the samples with fine W particles to distinguish the effect of porosity and the effect of the particle size. Another type of samples consisting of 2-μm Al, -325 mesh W and PTFE were prepared by uniaxial pressing at a pressure of 100 MPa, reaching 95% theoretical density. These samples were tested in the conventional drop-weight approach. Aluminum ring jackets with varying thickness were placed around this type of samples to terminate the tests at the beginning of deformation to attempt to capture the information of early deformation.

Hopkinson bar testing was performed using a low-impedance magnesium transmitting bar. Drop-weight tests with various arrangements including free standing and jacketed samples were used to find dynamic compressive strength with simple boundary conditions and to analyze microstructural development caused by high strain, high strain rate plastic flow and fracture.

An unusual phenomenon has been observed when comparing samples with fine W particles with lower density to those with coarse W particles, which had a higher density. The samples with higher porosity exhibited a higher strength in both quasi-static and dynamic experiments. It is an interesting behavior since higher porosity usually leads to lower material strength.

In Hopkinson bar tests, the ultimate compressive strength of the high density PTFE-Al-W composite (ρ= 7g/cm^3) with coarse W particles was σ_f = 24 MPa, while more porous PTFE-Al-W composite with fine W particles (ρ= 6 g/cm^3) had stress level as high as σ_f = 44 MPa. This tendency is consistent with data from a quasi-static tests where the ultimate compressive strength of the dense (ρ= 7 g/cm^3) PTFE-Al-W composite with coarse W particles was σ_f = 18 MPa and more porous PTFE-Al-W composite with fine W particles (ρ = 6 g/cm^3) exhibited strength σ_f = 24 MPa. Critical failure strains for both composites in quasi-static and dynamic tests are 4-5%.

A similar phenomenon of a significantly higher strength (σ_f = 55 MPa) of porous composites with fine W particles compared to the strength (σ_f = 32 MPa) of dense composites containing larger W particles was also observed in drop-weight tests.

It is explained the phenomenon of higher strength in these composite materials at relatively high porosity with fine W particles by the influence of force chains between them. Two-dimensional numerical analysis of drop-weight tests (where the boundary conditions correspond to constant speed of dropped weight) revealed that small particles create force chains that augment the effective global strength of porous granular materials. Based on the densities of tapped composite materials, it is considered that force chains are not significant in the composite containing large W particles containing the same volume fraction as samples with small W particles.

Microstrutural observation of heavily deformed samples after drop-weight and Hopkinson bar tests revealed that most of the plastic strain is accommodated by a soft

PTFE matrix with practically undeformed metal particles. The PTFE that is attached to W particles is extended in fracture, creating a network of nanofibers with diameters as low as 60 nm. For comparison we heavily deformed cold isostatically pressed PTFE-Al-W samples (submicron size W powder with a density of ρ= 6 g/cm^3) using Equal-Channel Angular Pressing (ECAP) and also observed nanoscale size PTFE films. Hollow cylindrical samples of composites were collapsed using a Hopkinson bar based thick walled cylinder (TWC) method. A chemical reaction in this system in these conditions of static and dynamic loading has not been observed.

The mixture had the following weight content of components: 77wt% W, 17.5 wt% PTFE, and 5.5 wt% Al. The final density of the pressed mixture was 95 % of the theoretical density. Due to the large difference in density between the constituents, PTFE was the major component on a volume fraction, 56%, followed by Al, 23 % and W, 21%. The typical height of the samples was 10mm and the diameter 10.44mm.

4.3.1 Small-scale Hopkinson Bar Assisted TWC Testing

Details and geometry of the experimental set-up for Hopkinson bar based thick walled cylinder tests are described in Section 3.6.2. In experiments with PTFE-Al-W glycerol as driving liquid was used.

Stresses in the incident bar, at the wall of the chamber with the sample, and in the transmitted bar are shown in Figure 4.9 below for corresponding samples.

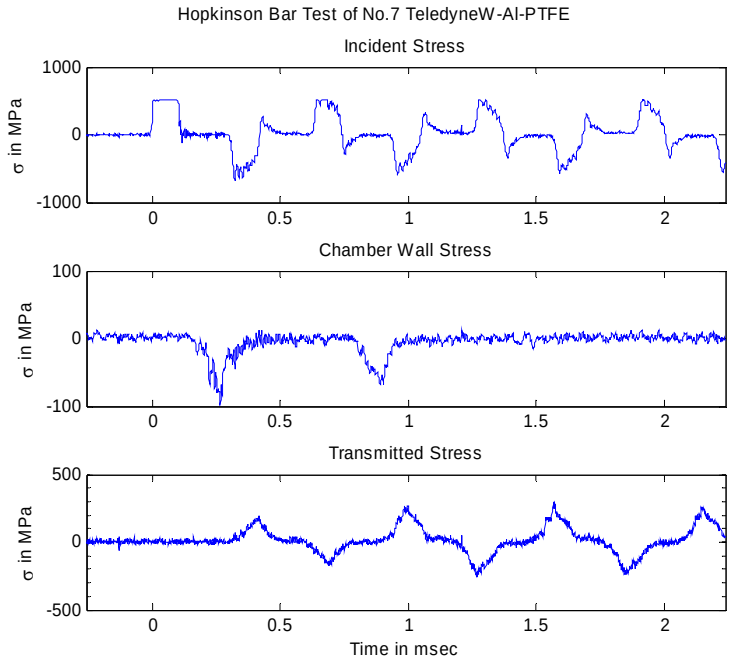

(a)

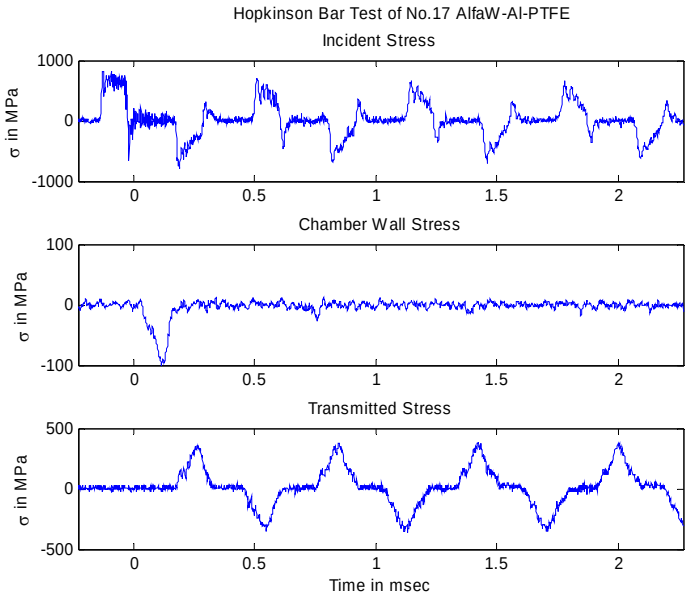

(b)

Figure 4.9 Stresses in the incident bar, at the wall of the chamber with the sample, and in transmitted bar are shown for corresponding samples: (a) oscillographs from the test with a dense PTFE-Al-W sample containing coarse W particles; (b) oscillographs from the test with a porous PTFE-Al-W sample containing fine W particles.

The experimental conditions were identical for two samples. However, for the low strength sample (discussed in Sections 4.3.2 and 4.3.2), two peaks were observed in the wave detected from the chamber wall and the first transmitted signal was weaker (Figure 4.9a). For the high strength sample (discussed in Sections 4.3.2 and 4.3.2), only one peak was observed in the wave detected from the chamber wall and the first transmitted signal was stronger (Figure 4.9b). The stronger transmitted signal represented a strong material. These results were consistent with the results that are presented in the following sections.

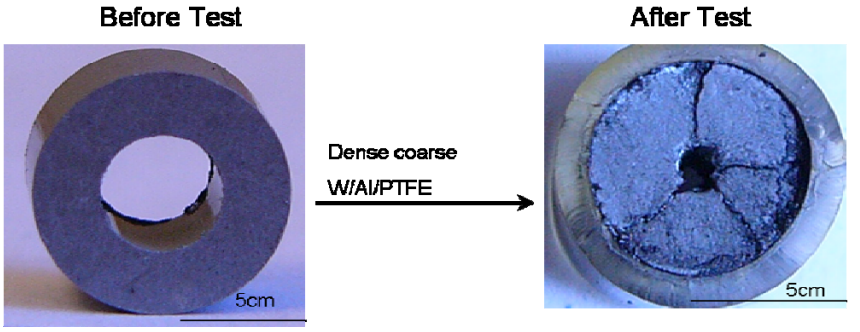

(a)

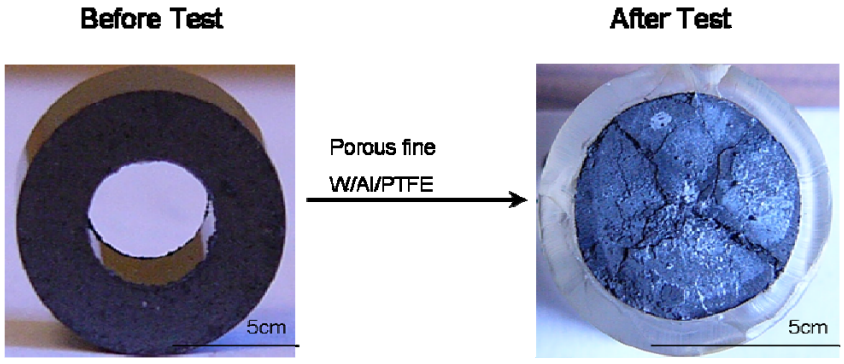

(b)

Figure 4.10 Images of hollow cylindrical samples before and after Hopkinson bar based TWC tests: (a) the weaker sample, i.e. the dense PTFE-A-W sample containing coarse particles; (b) the stronger sample, i.e. the porous PTFE-A-W sample containing fine particles; During the test samples were encapsulated in polymer jacket seen in figures after tests.

Figure 4.10 shows that the stronger sample was able to be collapsed, but the weaker one was not be able to do so in the same condition as the weaker sample. The stronger sample was symmetrically collapsed without developing shear instability. But the start of shear instability can be observed in the weaker sample. It is probably because the particles in the stronger sample were able to transfer stress effectively so it could bear more stress loading until it was totally collapsed. Due to the lack of an effective way to transfer stress in particles in the weaker sample, stress localization would occur to initiate shear bands. Cylindrically symmetrical overall deformation at the outside circumference of the sample and radial cracks are visible in both cases (Figure 4.10). The evidence of a reaction in this system in collapsed samples was not observed, unlike in similar test with PTEF/Al system.

4.3.2 Quasi-static and Hopkinson Bar Compression Testing

Quasi-static compression tests demonstrated that porous PTFE-Al-W composite with fine W particles show the highest compressive strength and display the highest elastic modulus (Figure 4.11 and Table 4.2).

Table 4.2 Strength of samples in quasi-static compression test.

Material	Average Compressive Strength (MPa)
Dense coarse PTFE-Al-W	18
Porous fine PTFE-Al-W	24
Porous coarse PTFE-Al-W	5

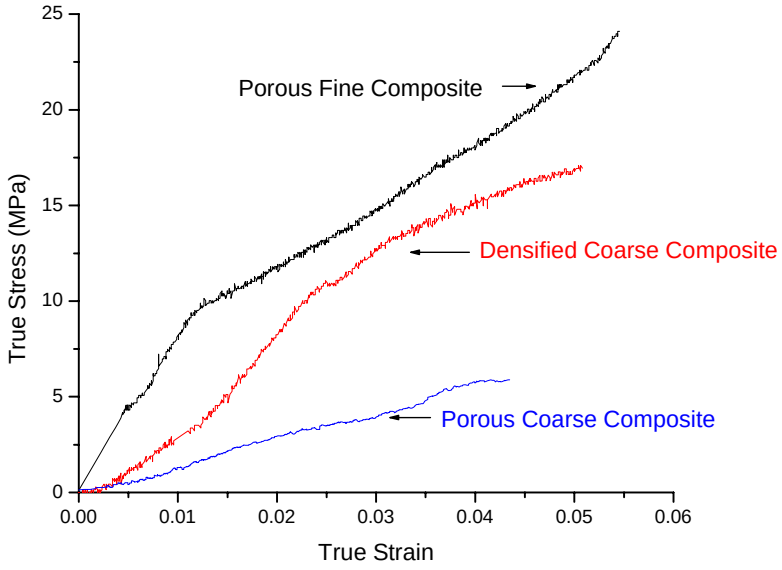

Figure 4.11 Quasi-static stress-strain curve of PTFE-W-Al composites with variation of one of the parameters: density (dense versus porous composites with coarse W particles) and particle size of W (porous composites with fine W particles versus porous composites with coarse W particles).

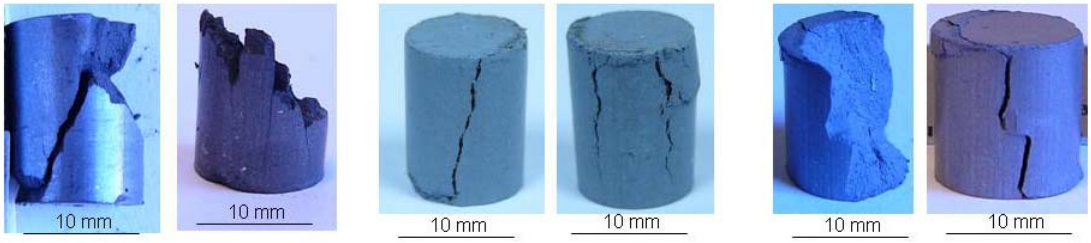

(a1) (a2) (b1) (b2) (c1) (c2)

Figure 4.12 Various sample composites after quasi-static testing. (a1) shear crack in the porous fine PTFE-Al-W composite sample; (a2) axial and shear cracks in the porous fine PTFE-Al-W composite sample; (b1) axial crack in the porous coarse PTFE-Al-W composite sample; (b2) axial cracks in the porous coarse PTFE-Al-W composite sample; (c1) shear/axial crack in the dense coarse PTFE-Al-W composite sample; (c2) kinked axial cracks in the dense coarse PTFE-Al-W composite sample.

The tested samples also demonstrated a consistently different pattern of fracture shown in Figure 4.12. It is natural to expect that porous materials in compression tests fail due to axial cracks caused by tensile stress concentration at the vicinity of pores (Timoshenko and Goodier, 1987). It is interesting that the more porous PTFE-Al-W containing fine W particles failed mainly because of shear cracks.

Dynamic testing was performed using the Hopkinson bar apparatus which consists used a magnesium transmitted bar. Because the investigated materials have a lower strength, a low-impedance magnesium transmitted bar was adopted to obtain low noise-to-signal ratio in transmitted waves. The measured stress-strain and strain-rate-strain curves of the PTFE-Al-W composite are shown in Figures 4.13-4.15.

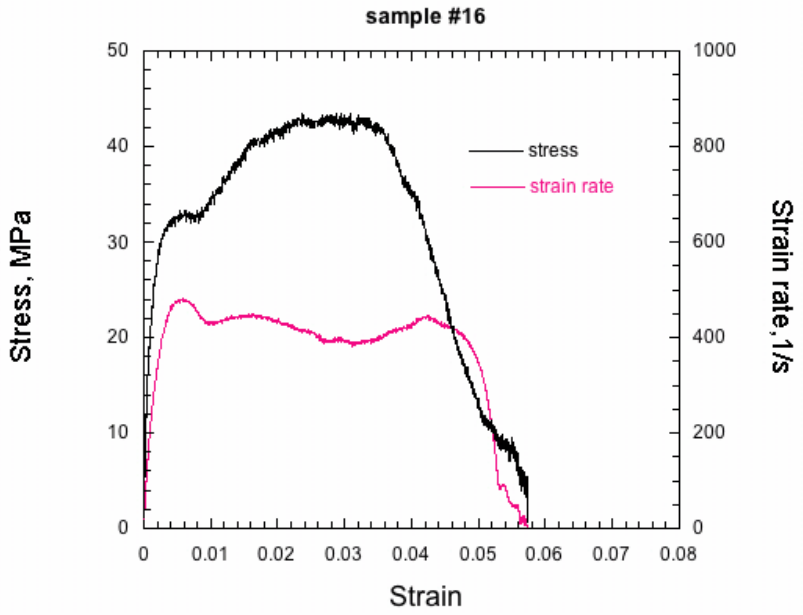

Figure 4.13 Hopkinson Bar strain-stress curve of a porous PTFE-Al-W composite sample containing fine W particles.

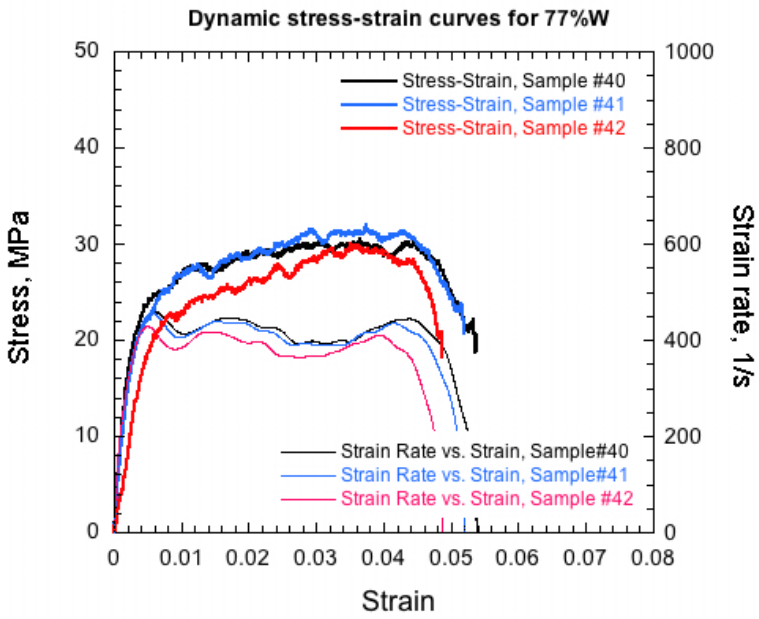

Figure 4.14 Hopkinson Bar strain-stress curve of dense PTFE-Al-W composite samples containing coarse W particles.

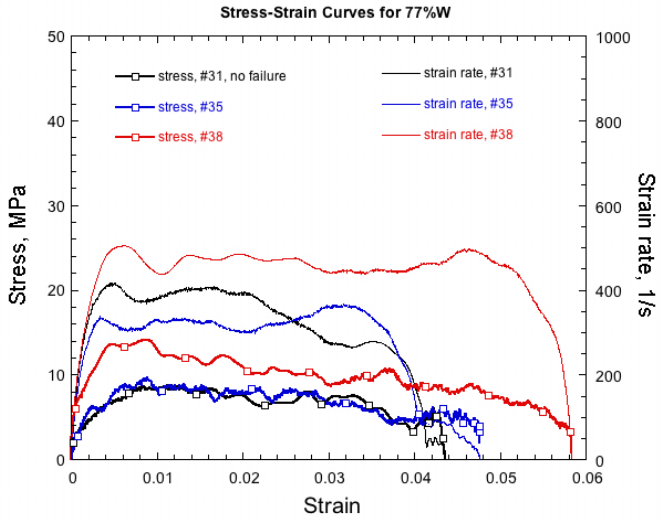

Figure 4.15 Hopkinson Bar strain-stress curve of porous PTFE-Al-W composite samples containing coarse W particles.

Samples of cold isostatically pressed PTFE to density 2.1 g/cm^3 were also tested (Figure 4.16) to provide information about strength of PTFE matrix in cold isostatically pressed composites and obtain information on failure strain (about 0.05) which was used in modeling composite behavior in numerical calculations [157].

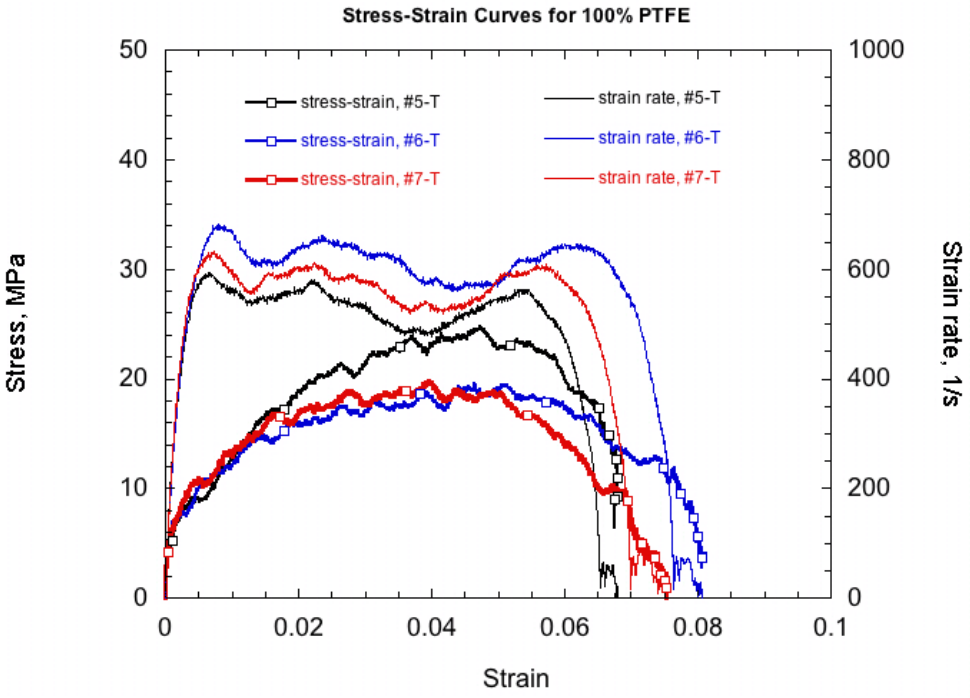

Figure 4.16 Hopkinson Bar strain-stress curve of cold isostatically pressed PTFE sample.

Compressive strengths of the samples with different mesostructures obtained in Hopkinson bar tests are presented in Table 4.3.

Table 4.3 Strength of samples in Hopkinson bar tests.

Material	Average Compressive Strength (MPa)
Dense coarse PTFE-Al-W	24
Porous fine PTFE-Al-W	44
Porous coarse PTFE-Al-W	18
Dense PTFE	20

The data in the Table 4.3 illustrate that the samples with fine W particles with higher porosity had higher strength than higher density samples with coarse W particles, which is an unusual phenomenon. This behavior is consistent with the results of quasi-static tests. It is an interesting phenomenon, because usually the more porous the material is, the weaker strength it has. Note that there were not any signs of chemical reactions in any of the Hopkinson bar tests.

4.3.3 "Soft" Drop-weight Testing

A “soft” drop-weight method (seen in Section 3.5.2), which allows testing of our samples with a relatively low mechanical strength, was described. The reason why a “soft” drop-weight was necessary in the research and the validation of the approach are

also presented in that section. Generally speaking, this test provided reliable output of the gauges at large strains including post critical behavior after shear localization, fracture and possible reaction at these stages.

4.3.3.1 Experimental Results

A standard drop-weight device in Cavendish Laboratory was initially employed to understand the materials' behavior under high engineering strain (~90%). In contrast, Hopkinson Bar testing usually generated ~5% strain for the PTFE-Al-W composites. Another advantage of this technique is that it allows the termination of experiments at the specific strain to explore the initial response of materials under high-strain, high strain-rate deformation. Additionally, a practically constant velocity at the interface between the dropped weight and the sample represents the boundary conditions in this test in the initial stages of deformation and is easily implemented in the numerical analysis presented below. The data generated by the drop-weight tests are the voltage output of the gauge converted into a stress-strain curve (Walley, 1989).

Because the PTFE-Al-W composite materials are relatively weak, the drop-weight testing usually caused the sample to collapse into a flat disk with thickness about 1 mm, which cannot be used to explain the failure mode of the sample at the earlier stages of flow especially because this composite samples had a relatively low critical failure strain. A copper ring was placed around the sample was utilized to cease the experiment at a specific strain. A schematic of the setup was shown in Figure 4.17. When

the dropped weight hit the ring, the deformation of the sample was terminated due to the resistance of the ring to the mass which resulted in fast increase of electrical signal allowing estimation of the average velocity of drop mass additionally to the standard measurements (Walley, 1989).

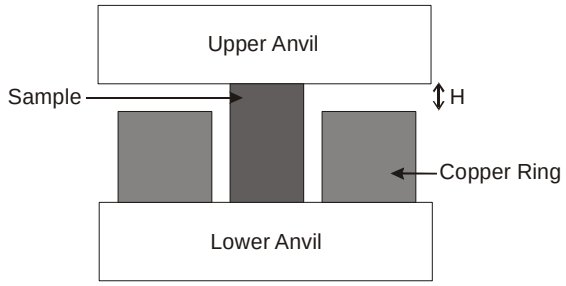

Figure 4.17 Schematic experimental set-up with the copper stopper ring.

A copper ring used to terminate the deformation to understand the failure mode of the sample and the initial stage of deformation. A post-test sample is seen in Figure 4.18. The copper ring succeeded in preserving the sample at a specific deformation, because the strain can be determined by the height of the copper ring (Figure 4.18a). Radial cracks propagated along approximately 45^{o} on periphery of the deformed sample with copper stopper ring (Figure 4.18b)

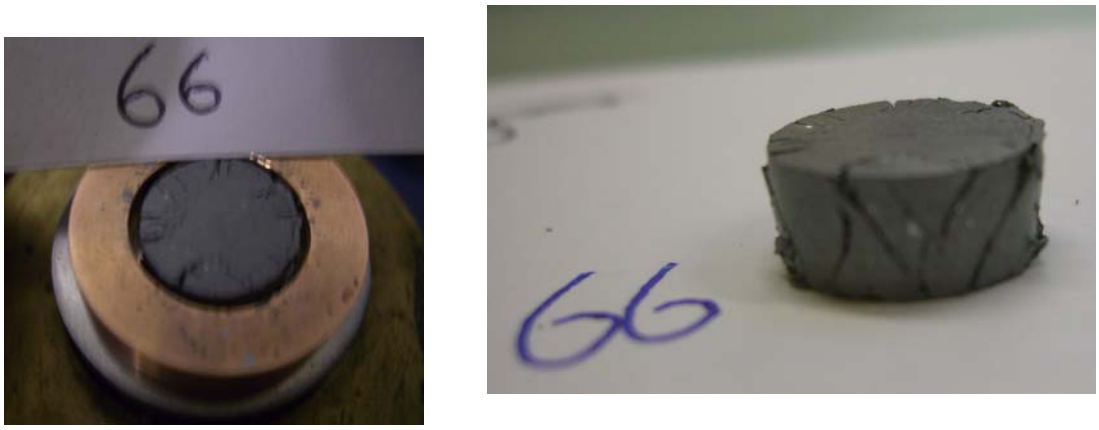

(a) (b)

Figure 4.18 (a) The picture of the copper ring and the sample after the drop-weight test; (b) failure mode of radical cracks.

The compressive strength of the samples obtained in the "soft" drop-weight tests is presented in Table 4.4.

Table 4.4. Compressive strength of samples in drop-weight tests.

Material	Average Compressive Strength (MPa)
Dense coarse PTFE-Al-W	32
Porous fine PTFE-Al-W	55
Porous coarse PTFE-Al-W	10

These values were very reproducible for dense coarse W samples (total number of tests 6, error bars 2 MPa) and porous fine W samples (total number of tests 5, error bars 5 MPa). In contrast with this data, the compressive strength of porous samples with coarse W were about 10 MPa in four tests and 51 MPa and 30 MPa in other two tests. High values of compressive strength in some tests were accompanied by a precursor signal suggesting that the failure could be preceded by densification. This is a reasonable argument taking into account that unusual values of maximum strength are above the densification pressure of 20 MPa employed to process these samples in cold isostatic conditions. This illustrates a very interesting competition between densification and macroscopic failure of porous composite sample which we are planning to address later.

The temperature increase in the bulk sample in the drop-weight tests was estimated. It assumed that all work done by the weight was converted into the heat absorbed by the temperature increase and the temperature increase was uniform inside the sample, the following equation is valid:

$$FL=\Delta TCm \tag{4.2}$$

where F is the force applied on the sample by the dropweight, approximately 18000N, L the displacement the weight went through, 8 mm, m the mass of the sample, typically 4.594 g, C is the heat capacity of the sample. C is calculated by the addition law of W, Al and PTFE. It is know that C_W is 132J/kg-K, C_{Al} 963 J/kg-K, and C_{PTFE} 1020 J/kg-K. The temperature increase estimated by this approach is 94K, which is not significant high to reach the melting point of Al (660C) and PTFE (340C, unsintered PTFE has a higher melting point than sintered one (323C)[158]). It should be noted that this temperature

increase was a uniformly temperature increase. Local temperature increase would be more profound.

4.3.3.2 Force Chains in Composites with Fine W Particles

The consistent results from quasi-static, Hopkinson bar, and drop-weight tests demonstrated that the porous PTFE-Al-W samples containing fine W particles has a higher strength that that of the densified samples containing coarse W particles. It is speculated that force chains between the fine W particles could contribute to this interesting phenomenon. Many experiments and numerical simulations have made it clear the existence of force chains in quasi-static and dynamic deformation of granular materials [159-161]. Figure 4.19 shows a distinct fracture path along fractured grains in a deformed plastic bonded explosive upon impact on a modified Taylor anvil. Experimental results demonstrated that force chains in the granular bed were formed upon initial loading for the static and dynamic tests [162]. Increasing stress along these paths could cause stress concentration resulting in crystal fracture. The sheared fractured crystals in the PBX would serve as a hot spot for the reaction ignition. Also, the friction between newly developed surfaces of fractured crystals could lead initiation. An irregular shape will increase the stress intensity, thus making stress concentration more likely, and which would subsequently assist ignition.

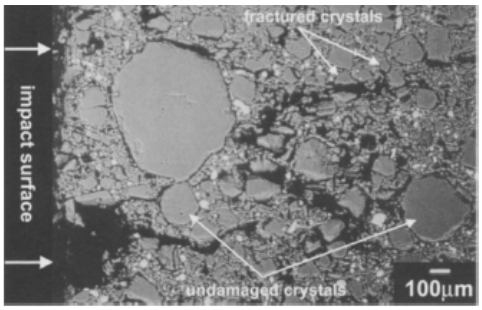

Figure 4.19 The cross section of a cure cast plastic bonded explosive demonstrates the stress chain damage evolution within these types of particulate materials [162].

Although the post-test examination does not resolve the time dependence of deformation process, the fracture path is indicative of the existence of stress chains. Unfortunately, it is extremely challenging, if not impossible, to examine the deformation process inside tested materials during high-strain-rate tests at the meso-scale. To understand the interaction between the constituents in this process, dynamic photoelasticity has been applied to examine the wave propagation and stress distribution [163].

Roessig [164] and Bardenhagen et al. [165] examined the effect of a binder on the stress propagation in plastic bonded explosives. Figure 4.20 represents the simulation results of dynamic compression of a series of PBX with varying binders. Figure 4.20a illustrates no binder between particles; Figure 4.20b-f illustrates the effect of binders. In this figure, the higher wave speed ratio between the binder and the particles, the harder the binder is. It is obvious that a soft binder, which has a much higher impedance than the particles in a PBX, only allows little compressive and shear stresses to be transferred. This is beneficial for the stress localization and the formation of ignition sites. By

contrast, a hard binder, which has a good impedance match between the binder and the particles, favors the stress transfer and distribution but exhibits disadvantage in terms of boosting ignition.

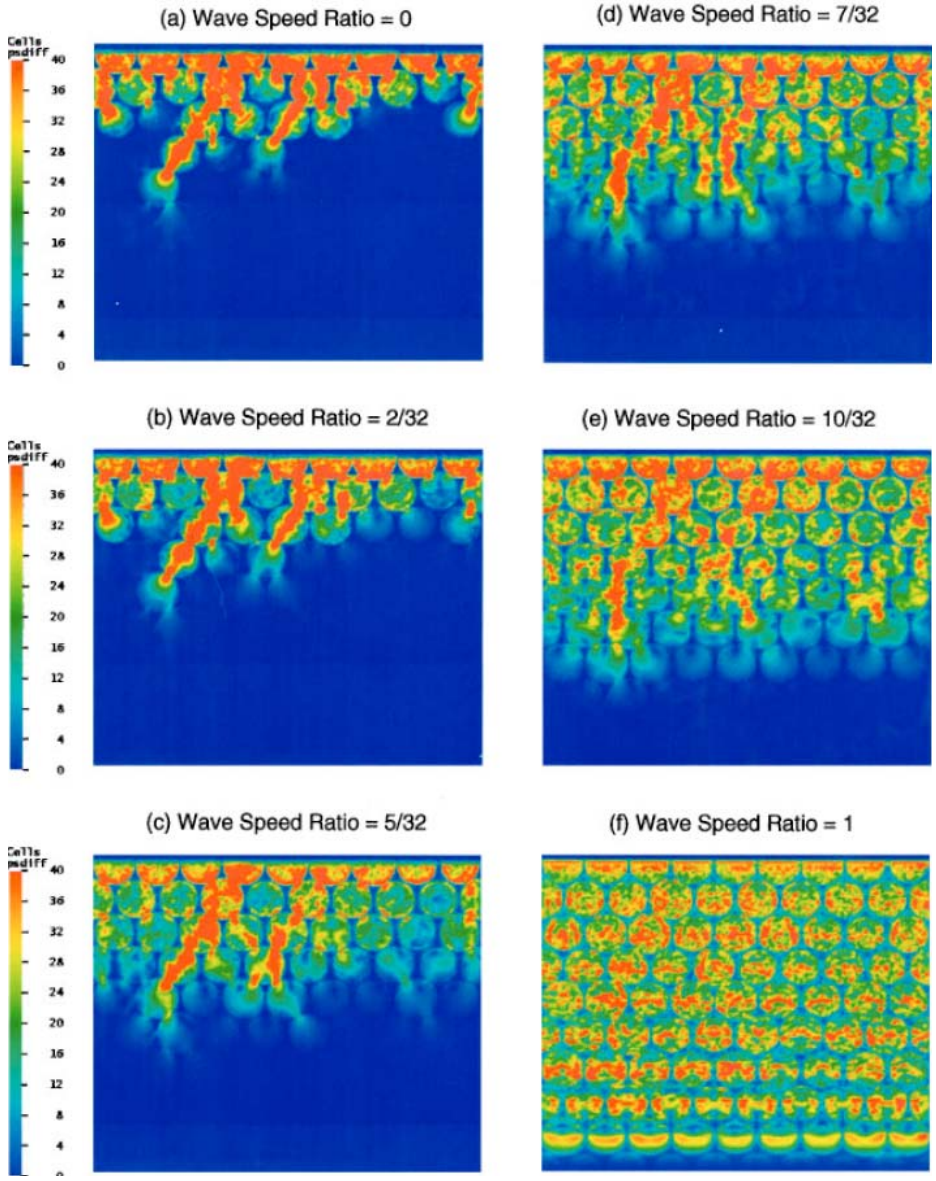

Figure 4.20 Contour plots of the difference in principal stresses (MPa) under weak shock loading for the lattice of cylinders (a) without binder and (b)-(f) with binder, where (e) is the case for which the binder is Adiprene-100. All contour plots correspond to the same time after impact [165].

The friction between the binder and the particles is also studied [162]. It shows that interface friction plays an important role for the stress transfer. Higher friction would increase the ability to transfer compressive and shear strength, so the stress concentration within the bulk materials decreases. It will allow the stress distributed more into the bulk materials. However, it may not be good for the formation of hot-spots, which could require a stress concentration for heating local region.

In this research, polymer (PTFE) serves as the continuous matrix instead of the interstitial binder in PBX. In PBX, granular particles are in good contact with each other. However in the investigated composite system, the contact of metal particles is limited owing to their relatively small volume fraction in the composites. But local arragnement of fine W particles provides possibility that force chains forms along contacting particles. Compare to fine W particles, coarse W particles have less probability to contact each other, though the volume ratio of W powder in two composites remains the same. Also, those studies have focused on the 2-dimensional configuration. Our experimental study is on a 3-dimensional condition with actually investigated materials. Plus, particles were placed in a good order in the above mentioned simulations, while they are randomly distributed in our case.

A two-dimensional Eulerian Hydrocode with diffusive heat transfer implemented to investigate the quasi-static behavior of the sample was done by Herbold [157]. A constant velocity of 4.43m/s was prescribed across the top boundary and the bottom of the specimens was fixed in the vertical direction. Along both the top and bottom

boundaries a tungsten slab was used to simulate the drop-weight test conditions where a steel anvil was used to strike the specimens on a steel base. The specimen material was allowed to slip along both the top and bottom boundaries without friction. The boundary conditions on the left and right sides of the specimens were free from restriction

The specimens use small tungsten particles (~1μm) and large aluminum particles (~2μm) surrounded by a PTFE matrix (Figure 4.21). The first random specimen (Figure 4.21a) was selected based upon the appearance of a particle distribution initially concentrated at some type of band that would easily create force chains and resist the loading. The second random specimen (Figure 4.21b) where force chains were less probable was selected where the particles were distributed more or less evenly throughout the PTFE matrix.

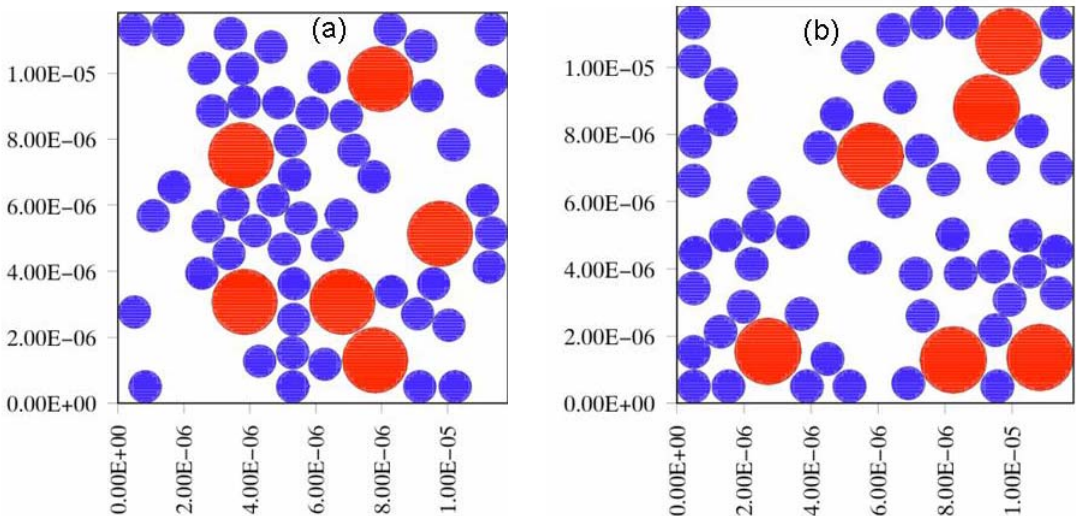

Figure 4.21. PTFE-W-Al specimens using 2μm Al particles and 1μm W particles: (a) force chains of metal particles were introduced (specimen 1); (b) force chains less probably exist (specimen 2) .

The numerical analysis shows that the effective yield stress of specimen 1 (Figure 4.22 a) is 85MPa; and the effective yield stress of specimen 2 (Figure 4.22b) is only 35MPa. It can be seen that in specimen 1 force chains were being created and activated and yielding in specimen 2 did not result in force chains which could provide structural enforcement of the specimens.

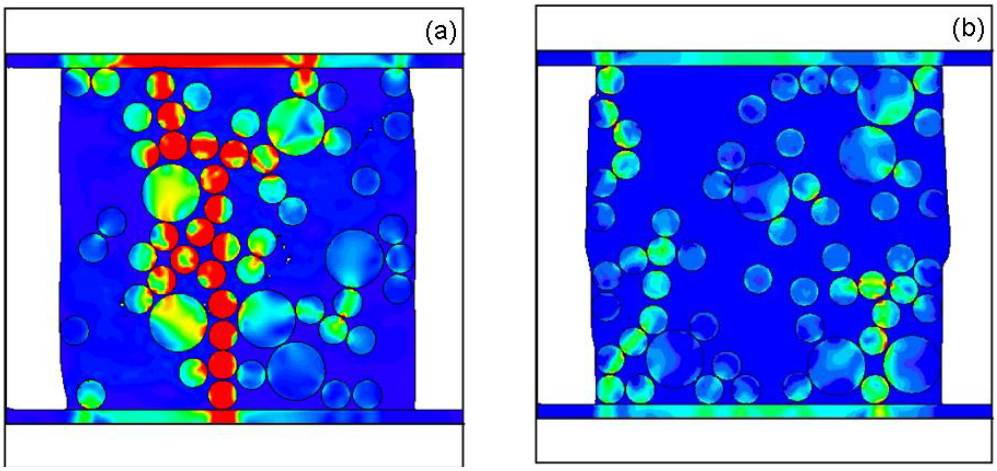

Figure 4.22. Plots show local Mises stresses at each specimen's yield point and the colors indicate the level of strain throughout the specimens from 0 (light) to 50 MPa (dark): (a) specimen 1 yielded at 0.022; (b) specimen 2 yielded at 0.0018 .

The presented two-dimensional calculations demonstrated that force chains created by metallic particles are a probable cause of the higher strength of these mixtures with volume content similar to three dimensional packing of powders.

This speculation is also supported by the observation of tapped densities of coarse W, fine W, Al and mixtures of Al with fine or coarse W particles presented in the Table 4.5. Tapped density of powders means that the powder was only tapped into the smallest volume by hands, not any equipment was employed in this procedure. In this table, the

ratio is the density of the tapped powder to the theoretical density of the solid, i.e. the volume fraction of the solid phase in a tapped powder. It means that if the volume fraction of the powder in a material is higher than this number, there is the existence of force chains. In Table 4.5, it can be seen that the tapped mixture of coarse W and Al powders is characterized by a volume fraction of solid phase equal to 69%. This number is larger than 44%, the volume fraction of metal particles in the PTFE-Al-W composites. It means that force chains supporting the mesostructure of the tapped mixture of coarse W and Al powders will probably be destroy by adding PTFE powders into the mixture and densifying the composite. It is highly possible that force chains will not be active in the PTFE-Al-coarseW composite samples and the strength of the composite will be mainly determined by the PTFE matrix in agreement with experiment results.

In the case of the tapped mixture of fine W and Al powders, the volume content of the solid phase in the mixture is equal to 27%. This number is small than 44%, the volume fraction of metal particles in the PTFE-Al-W composites. It means that adding 56 vol% PTFE into the mixture of fineW-Al and densifying the PTFE-Al-fineW will not be able to destroy force chains, which are used to support the mesostructure of the mixture. It is evident that force chains between metal particles structurally support the low density PTFE-Al-fineW composite samples.

So, one can safely conclude that the addition of PTFE breaks the force chains in the densified PTFE-A-W specimens containing coarse W particles. And the PTFE matrix does not suppress activation of force chains which provide structural support and higher

strength for large strain deformation in the porous PTFE-Al-W specimens containing fine W particles.

Table 4.5. Density and volume fraction of solid components in tapped powders

Tapped Powder	Theoretical density of solid (g/cm^3)	Density of tapped powder (g/cm^3)	Volume of solid phase in tapped power (%)
Coarse W	19.3	9.5	49
Fine W	19.3	4.2	22
2-μm Al	2.7	1.1	40
Mixture of coarse W and 2-μm Al (weight ratio of W to Al 14 :1)	13.7	9.5	69
Mixture of fine W and 2-μm Al (weight ratio of W to Al 14 :1)	13.7	3.7	27

4.3.4 Conventional Drop-weight Testing

The PTFE-Al-W composite was fabricated by cold uniaxial pressing at a pressure of 100 MPa. The initial powders had the following average sizes: Al: 2 μm (ValimeH-2 and H-95); W: <44 μm (Teledyne, -325mesh); PTFE: 100 nm (DuPont, PTFE 9002-84-0, type MP 1500J).

The samples were tested in the unconfined and confined conditions. The use of confinement rings of an aluminum alloy 7075-T6 enabled arrest of the experiment at different strains. Aluminum rings with the same height as the samples and thicknesses of 0.5, 1, 1.5, and 2 mm were used.

Figure 4.23(a) shows the velocities of the drop weight as a function of time for the 0.6 m setup; it can be seen that the greater the load, due to the presence of the confinement ring, the faster the velocity decreases. The corresponding strain rates are shown in Figure 4.23(b) as a function of strain. For the unconfined sample and sample confined with a 0.5 mm ring, the strain rate actually increased slightly from an initial value of approximately $400s^{-1}$. As the Al alloy confinement ring thickness increased, the strain rate decreased. For the 2mm confinement ring, the strain rate reached zero at a strain of 0.25. This corresponds to the arrest of sample deformation. The velocity of the drop weight was measured and this was used for the determination of the strain. In this manner it was possible to obtain the stress-strain response of the sample/confinement ring assembly.

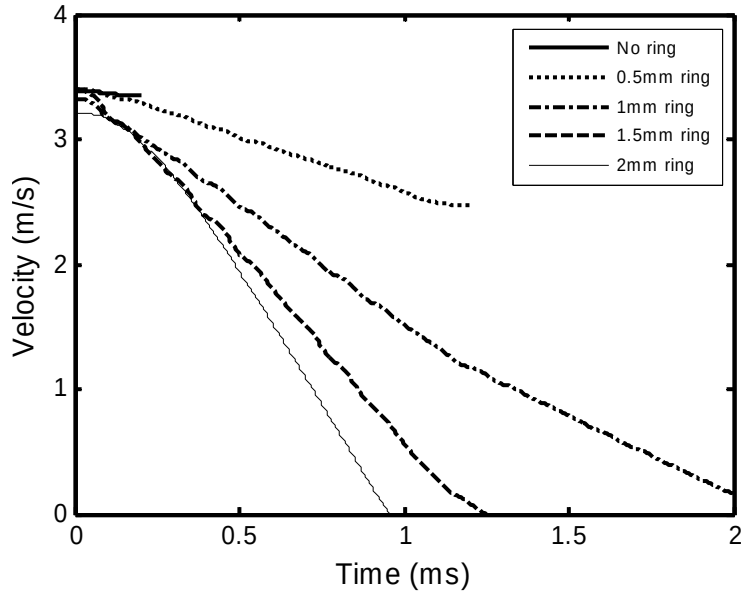

(a)

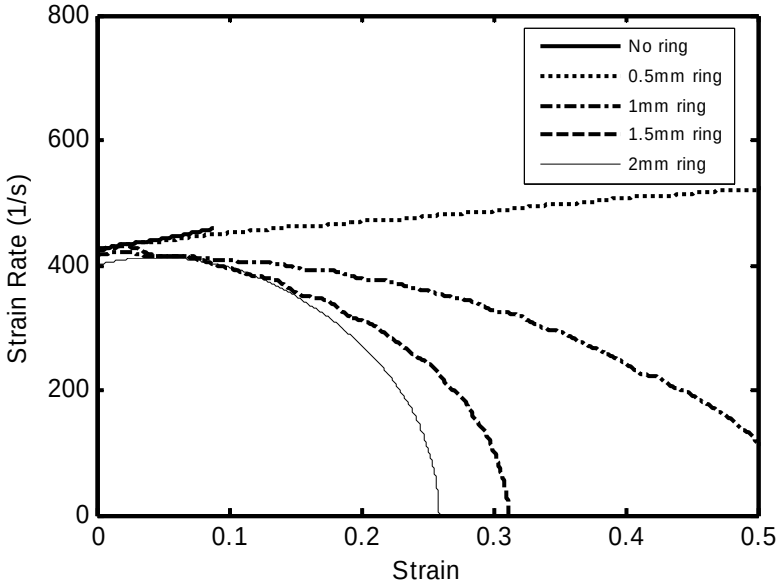

(b)

Figure 4.23 Effects of confinement on drop weight velocity and composite deformation strain rate: (a) velocity as a function of time after impact; (b) strain rate as the function of strain.

4.3.4.1 Compressive Strength

The different samples after deformation are shown in Figure 4.24. The sample and an Al confinement ring are shown on top, and the post-deformation configurations at the bottom. As the confinement ring thickness increased the total deformation undergone by the samples decreased, in accordance with the strain rate vs. strain plot of Figure 4.23 (b). The 0.5 mm ring underwent total buckling and folding, whereas the 1mm ring underwent barreling and lateral cracking. On the other hand, the 1.5 and 2 mm rings retained their cylindrical shape. The aluminum ring (2 mm thick) was tested separately both quasistatically and dynamically. The results are shown in Figure 4.25. By comparison, the quasistatic compression curve (10^{-3} s^{-1}) is much more smooth and accurate. The results in Figure 4.25 indicate that the dynamic strength of the aluminum alloy used is approximately 400 MPa, whereas the quasistatic strength is approximately 300 MPa. It can be assumed that the strength of the material reaches a saturation level where work hardening is absent. This strain-rate sensitivity is expected in aluminum alloys [166-168]. This value was used in estimating the corrected flow stresses of the sample-confinement assemblies.

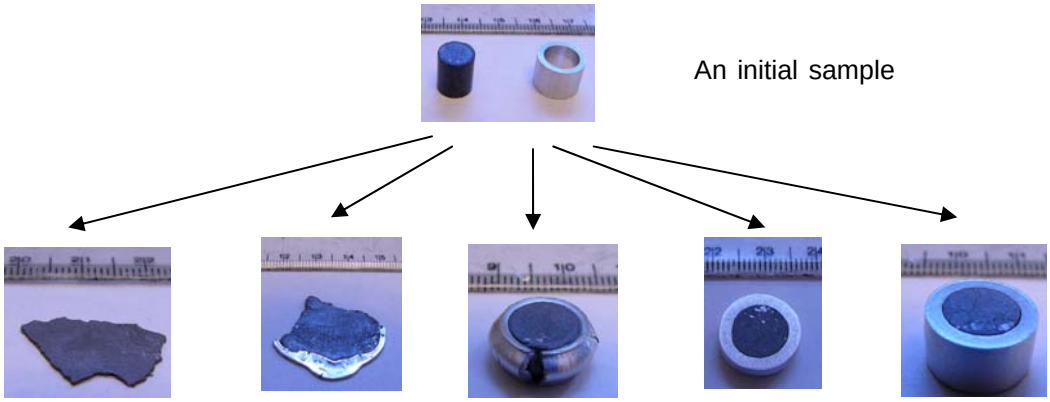

Figure 4.24 Configuration of samples before (top) and after (bottom) testing.

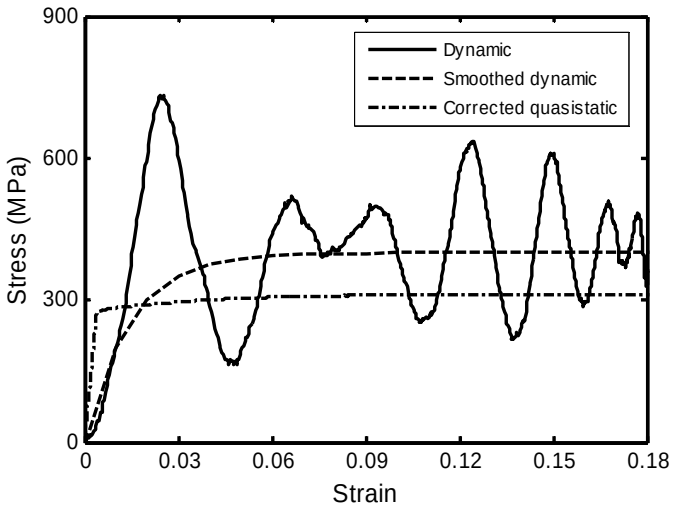

Figure 4.25 Quasistatic and dynamic (drop-weight test) response of aluminum alloy used in sample confinement.

It should be mentioned that the Al rings only provide limited confinement since the internal diameter of the rings increases with strain. In the absence of frictional stresses at the platens, the volume inside the orifice is constant. Thus, the principal

effects of the Al rings are (a) to allow the sample to deform without fragment, and (b) to provide a limited confinement.

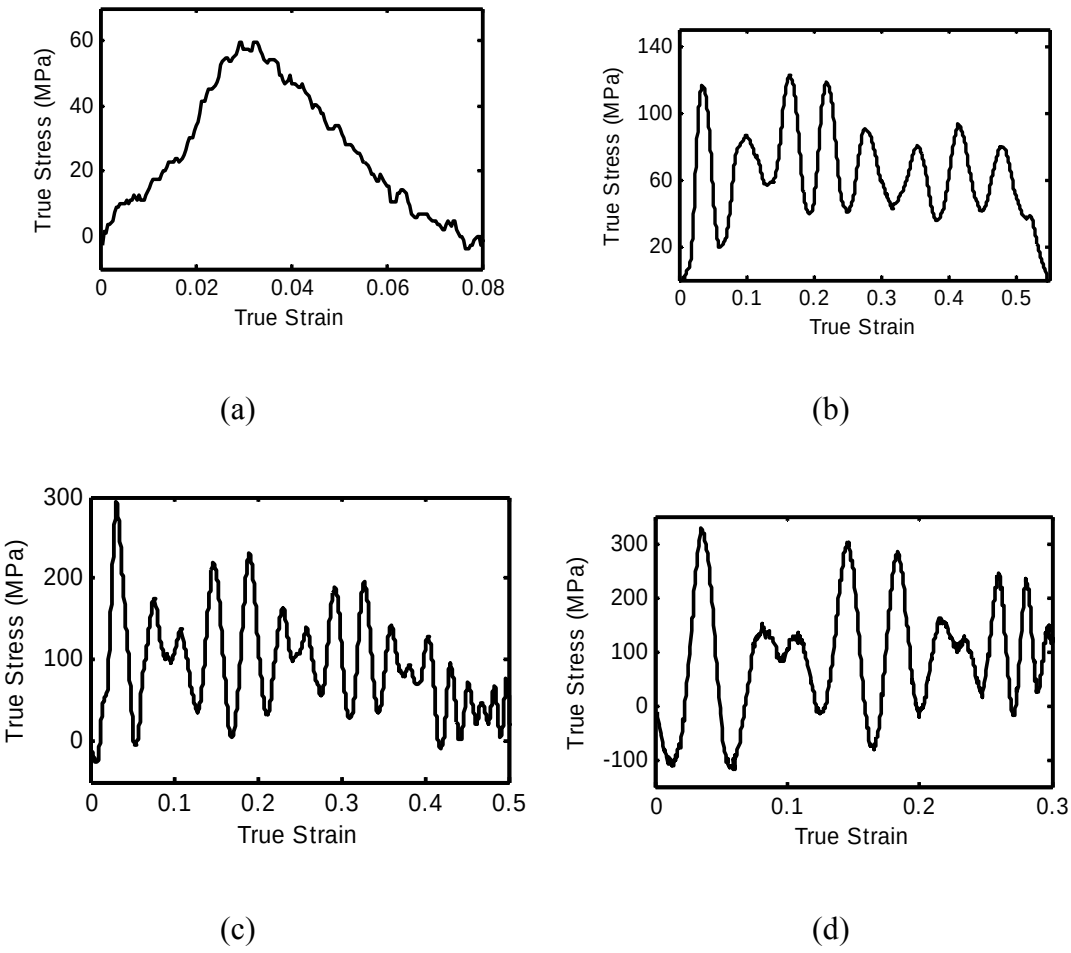

Figure 4.26 Compressive response of samples subjected to various confinement conditions: (a) no confinement; (b) 0.5 mm Al; (c) 1 mm Al; (d) 1.5 mm Al.

The results of the dynamic tests under different confinement conditions are shown in Figure 4.26. In the absence of confinement the stress rises to 60 MPa and rapidly drops (Figure 4.26(a)). This is due to fracture and fragmentation of the sample under the anvil. This occurs at a low strain of 0.035. The confinement significantly increases the range of

plastic strain that the samples can undergo, as shown in Figure 4.26 (b-d). The fluctuations in stress are very high. For the 0.5 mm Al ring, the flow stress is approximately 80 MPa, slightly higher than the unconfined sample. However, the sample retains its load-carrying ability up to a strain of 0.5. As the thickness of the confinement ring increases to 1 and 1.5 mm, the strength of the composite increases correspondingly. This is evidence of confinement, which is actually non-existent if one assumes that frictional effects at the platens do not exist.

The calculated stress-strain response obtained from the Zerilli-Armstrong constitutive equation [169] for polymeric materials is shown in Figure 4.27. The equation was inspired in the two Z-A equations for metals [170,171]. The constitutive model has the form:

$$\sigma = Be^{-\beta T} + B_0\sqrt{(1-e^{-\omega\varepsilon})/\omega}e^{-\alpha T}$$

$$\begin{aligned} &\textit{Where}: \\ &\beta = \beta_0 - \beta_1 \ln\dot{\varepsilon} \\ &\alpha = \alpha_0 - \alpha_1 \ln\dot{\varepsilon} \\ &\omega = \omega_a + \omega_b \ln\dot{\varepsilon} + \omega_p p \\ &B = B_{pa}(1+B_{pb}p)^{B_{pm}} \\ &B_0 = B_{0pa}(1+B_{0pb}p)^{B_{0pm}} \end{aligned} \qquad (4.3)$$

Where T is the temperature, P is the pressure, $\dot{\varepsilon}$ is the strain rate and the other symbols are parameters listed in Table 4.6. The parameters for PTFE that were used in Z-A equation [169] are shown in Table 4.6. Please note the values of ω_a and ω_p and the units of B_{pb} and B_{0pb} are different from Zerilli-Armstrong's. It can be seen that PTFE exhibits

very high strain-rate and temperature sensitivity (much higher than metals). This is a defining feature of polymers.

Table 4.6 Parameters in Zerilli-Armstrong equation for the visco-plastic deformation of PTFE.

β_0 (K^{-1})	2.01×10^{-2}
β_1 (K^{-1})	2.64×10^{-4}
α_0 (K^{-1})	4.78×10^{-3}
α_1 (K^{-1})	5.02×10^{-5}
ω_a	-2
ω_b	-0.625
ω_p (MPa^{-1})	-3.1×10^{-2}
B_{pa} (MPa)	4016
B_{pb} (MPa^{-1})	2.0×10^{-2}
B_{pn}	0.714
B_{0pa} (MPa)	72.4
B_{0pb} (MPa^{-1})	2.2×10^{-2}
B_{0pn}	0.5

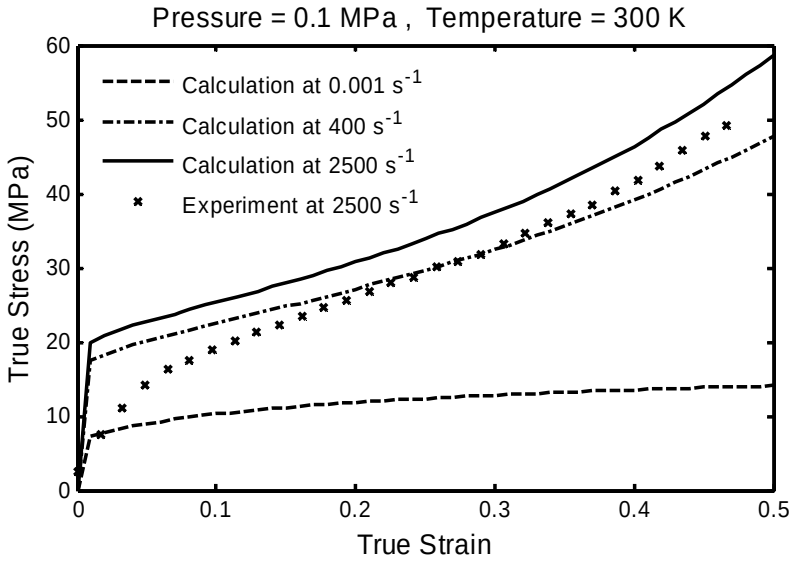

(a)

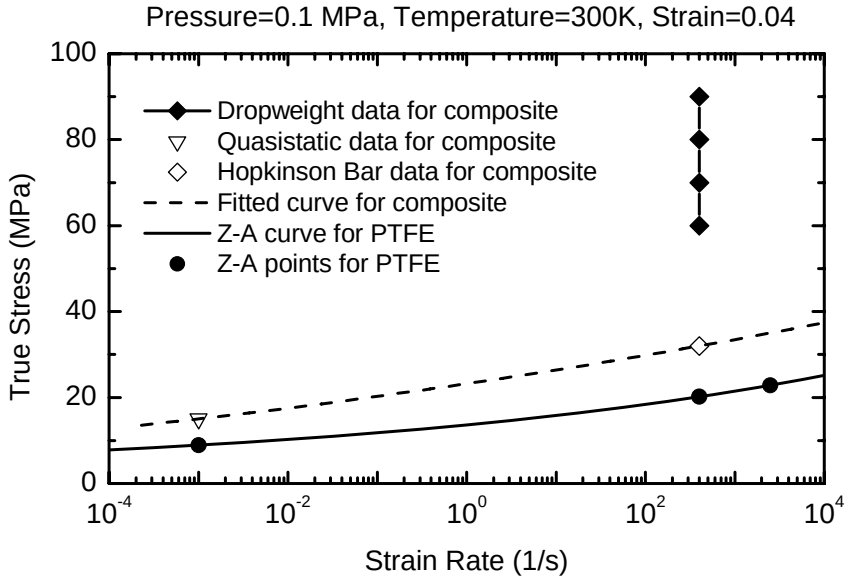

(b)

Figure 4.27 (a) Experimental and computed compressive stress-strain curves of PTFE at different strain rates. (Experimental data adopted from Walley et al. [122]); (b) Comparison of composite PTFE-Al-W and PTFE on compressive strength at the same strain.

Figure 4.27(a) shows the calculated stress-strain response for PTFE compared to the experimental results by Walley et al. [122]. Figure 4.27(b) shows the predicted values of the flow stress (for strain=0.04) as well as the experimental values for the PTFE-Al-W mixture. The calculated flow stress of PTFE at a strain of 0.1 at the strain rate of 10^{-3} s^{-1} is approximately 10 MPa. This value is approximately one half of the value of the strength of the composite sample surrounded by 1.5 mm Al ring (Figure 4.28), suggesting that the majority of the deformation takes place in the continuous PTFE matrix. The addition of metal increased the flow stress (dashed curve in Figure 4.27(b)). However, the strain-rate sensitivity is not changed. It is seen that the PTFE-Al-W mixture parallels the Z-A equation at low strains. Flow stresses of composites tested via the drop-weight apparatus are higher because of the confinement effect and the drop-weight technique itself.

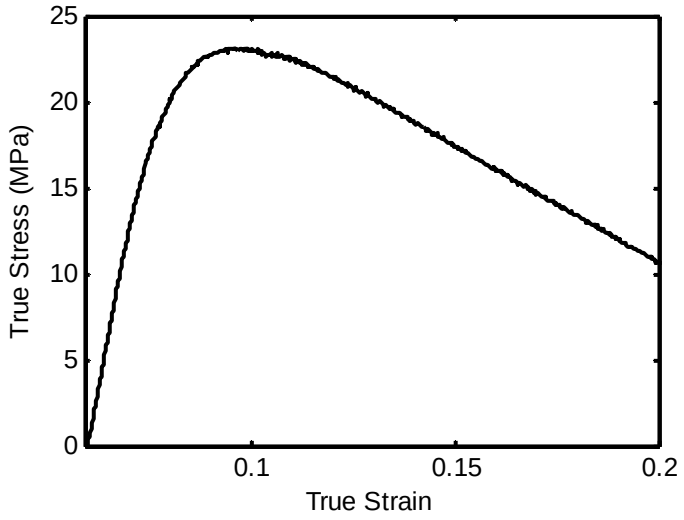

Figure 4.28 Quasistatic compression response ($\dot{\varepsilon} \sim 10^{-2}$ s^{-1}) of composite sample surrounded by 1.5 mm Al ring (force on ring subtracted from the total force).

4.3.4.2 High-speed photography

This technique was used on an unconfined sample to establish the degree of uniformity of deformation. The results are shown in the sequence of Figure 4.29. This is a negative, i.e. the dark regions correspond to the outside and the light to the sample and compression platens. The sample position is marked SP. in Figure 4.29. The initial height of the sample, h_0, was equal to 8 mm. Four snapshots are shown, at decreasing heights, h: 7, 6, 5, and 4 mm; they correspond to true compressive strains of -0.133, -0.288, -0.470, and -0.693. One of two lateral surfaces of the sample (left surface) is shown. For h=7 mm, the surface is fairly smooth. As the strain increases, irregularities at the surface initiate and grow. They are marked with arrows in Figure 4.29(d). These irregularities are due to shear localization/cracking. It can be concluded that, in the absence of confinement, the deformation becomes highly heterogeneous. These results are consistent with the stress collapse measured in the unconfined compressive test (Figure 4.26(a)).

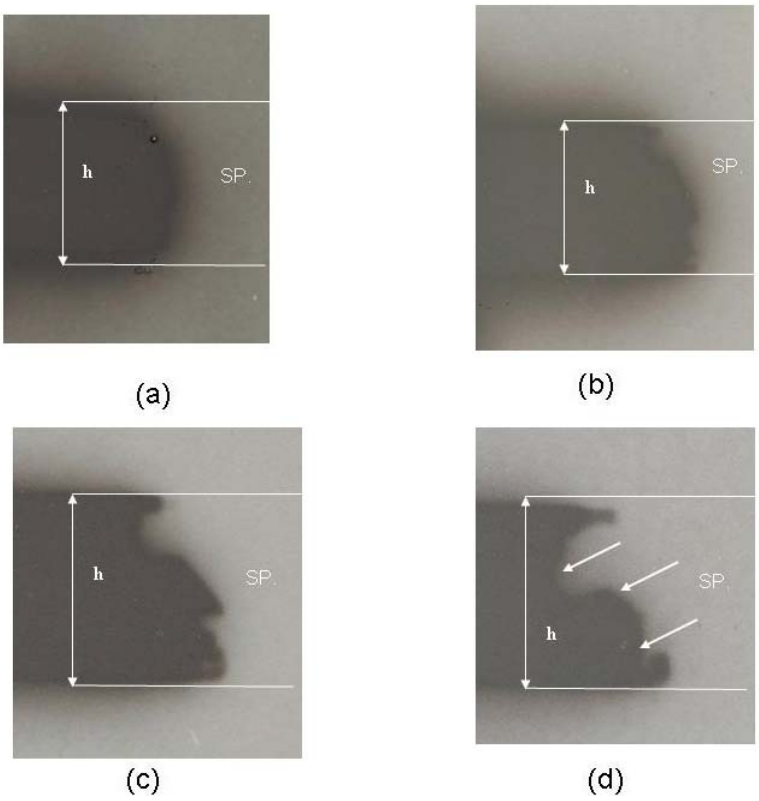

Figure 4.29 Snapshots from high-speed photography of compression of unconfined sample: (a) height=7 mm, $\varepsilon = -0.133$; (b) height=6 mm, $\varepsilon = -0.288$; (c) height=5 mm, $\varepsilon = -0.470$; (d) height= 4 mm, $\varepsilon = -0.693$.

4.3.5 Microstructural evolution

The initial microstructure and that after high-strain high-strain-rate deformation of the PTFE-Al-W composites are discussed in this section.

4.3.5.1 Initial Microstructures

The initial microstructure of the uniaxial pressed composite is shown in Figure 4.30. The backscattered image shows the W particles as bright features because of their high atomic number. The Al and PTFE cannot be distinguished in the low-magnification SEM micrograph of Figure 4.30a; Figure 4.30b resolves the features. Medium grey spherical features represent Al agglomerates. The individual Al particles (2 μm diameter) can only be faintly resolved.

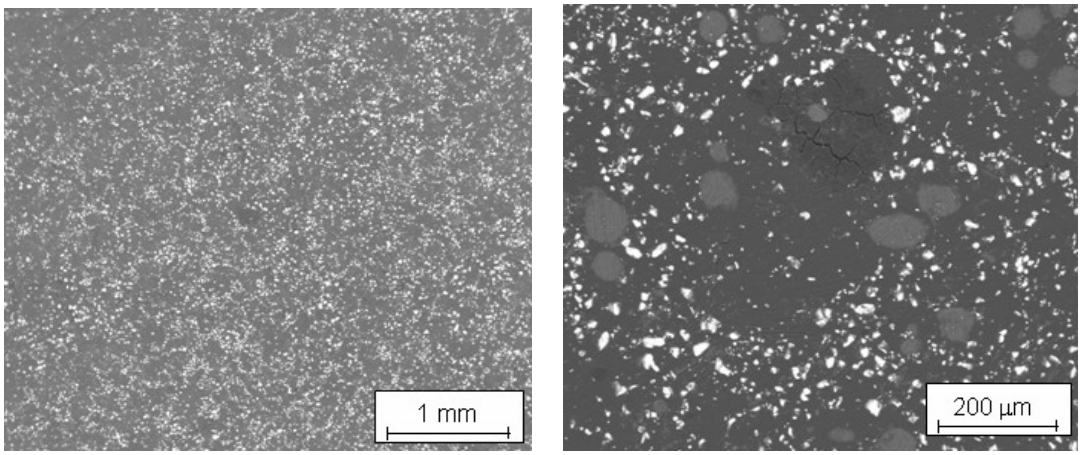

(a) (b)

Figure 4.30 Backscattered SEM images of initial compact configuration at: (a) lower magnification; (b) higher magnification.

Observation of a fracture surface shows the three constituents in a clearer fashion (Figure 4.31a). The larger W particles, which have a spheroidal shape, are surrounded by PTFE (the majority volume fraction) and Al. The PTFE forms the continuous matrix in which the W and Al particles are discretely distributed. Elemental analysis (Figure 4.31 b-d) for three particles is attached.

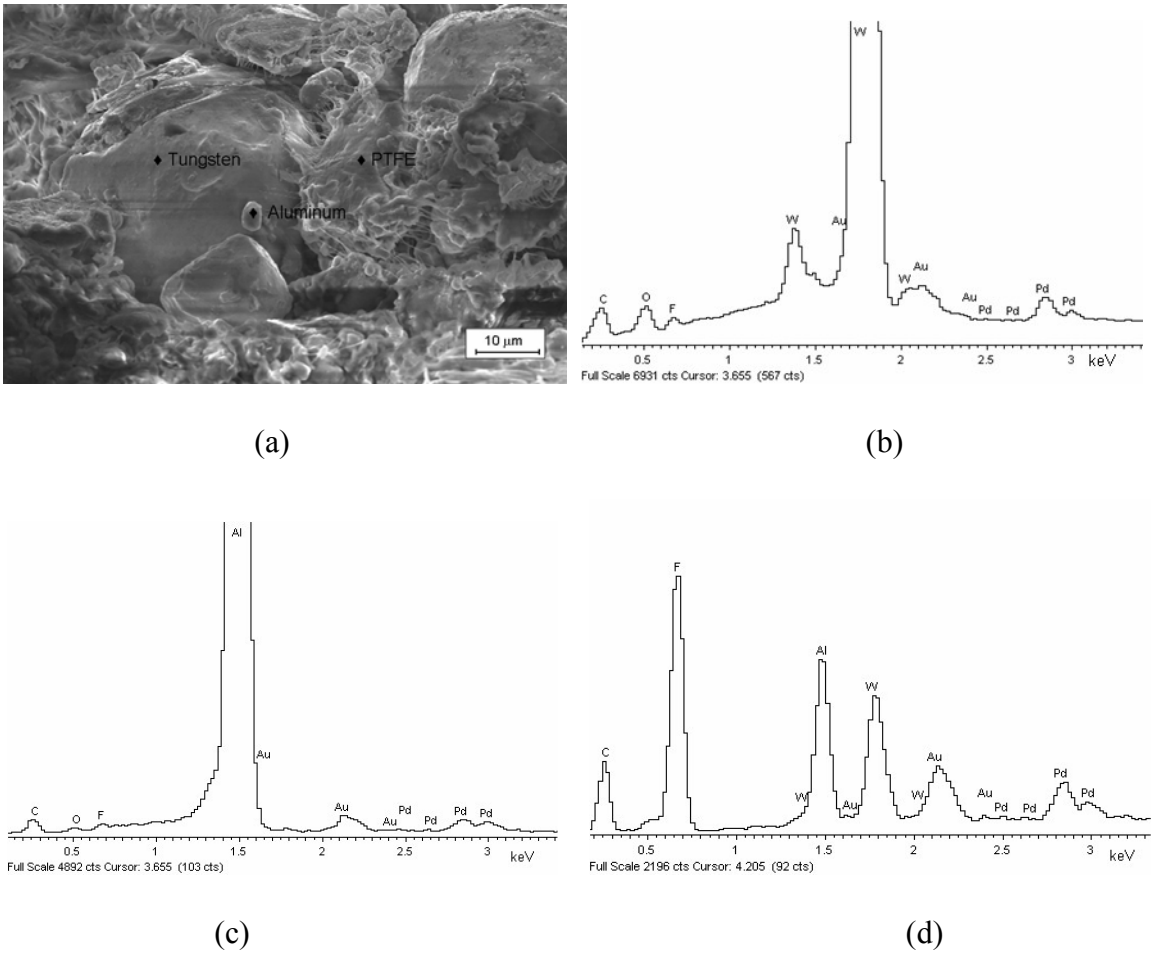

Figure 4.31 Identification of three components by secondary SEM and EDS: (a) fracture surface; (b) W; (c) Al; (d) PTFE.

The microstructure of cold isostatically pressed PTFE-Al-W composite samples are presented in Figures 4.31. It is clear that pores existed in the PTFE matrix in the porous PTFE-Al-W composite sample containing the coarse W particles (Figure 4.32) before dynamic testing. Because the CIPing pressure was much lower, only 20 MPa, the PTFE particles remained their initial shape. Individual PTFE particles are visible. PTFE fibers can be detected. Their formation is due to the manufacturing process.

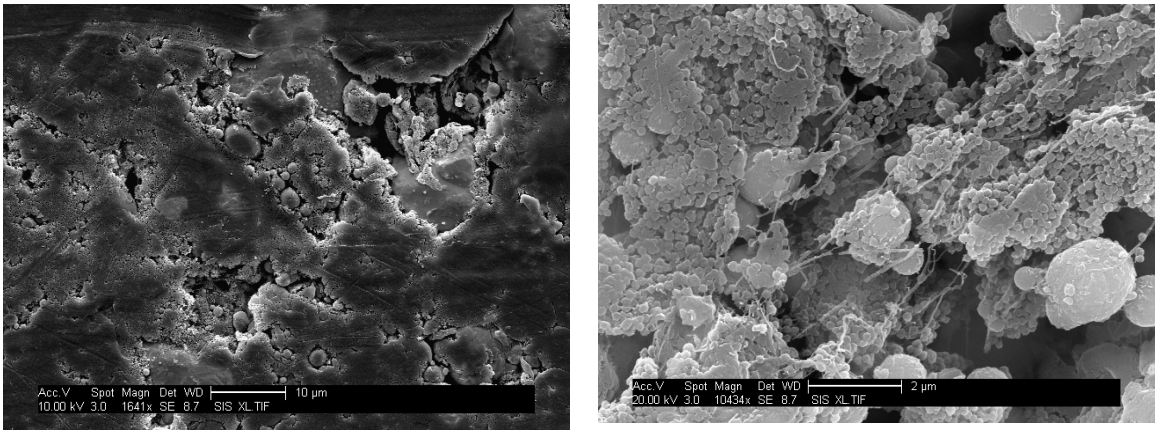

(a) (b)

Figure 4.32 SEM images of samples: (a) low magnification and (b) high magnification of the porous PTFE-Al-W composite sample containing coarse W particles.

By contrast, the uniform continuous PTFE matrix was bonded tightly with metallic particles in the dense PTFE-Al-W composite sample containing the coarse W particles (Figure 4.33) before dynamic testing. High magnitude of SEM micrograph shows that the PTFE matrix was populated by the small gaps, which are most probably the remaining initial PTFE particles (Figure 4.33 b).

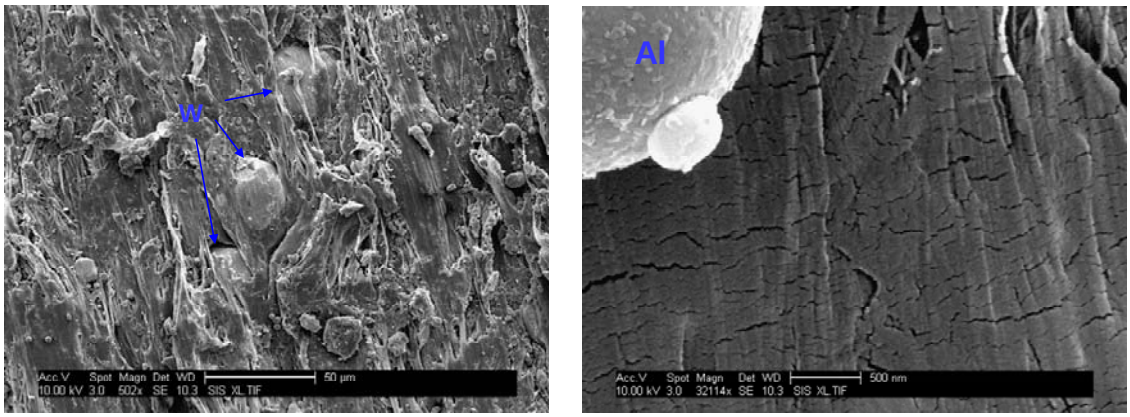

(a) (b)

Figure 4.33 SEM images of samples: (a) low magnification and (b) high magnification of the dense composite PTFE-Al-W sample containing coarse W.

Pores and agglomeration of fine W particles are visible in the porous PTFE-Al-W composite sample containing the fine W particles (Figure 4.34) before dynamic testing. It also has a PTFE matrix populated by the small apertures (Figure 4.34 b).

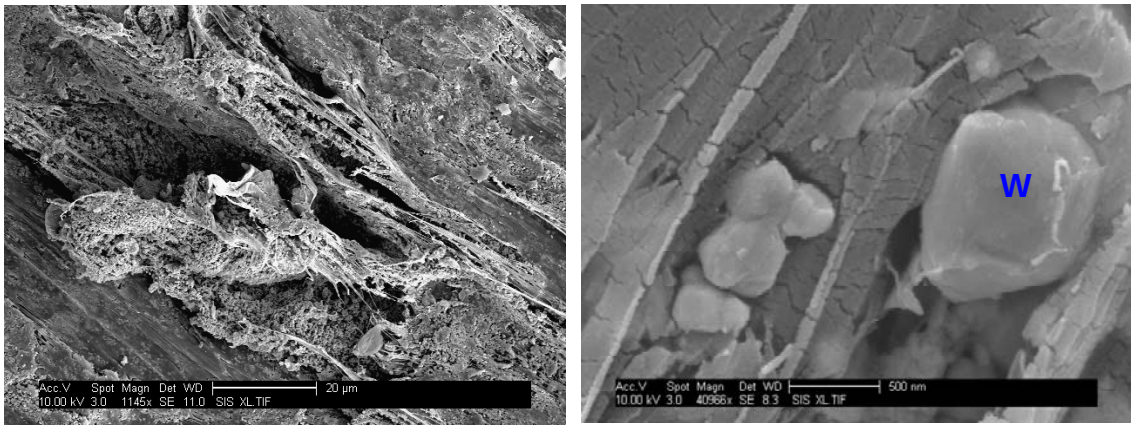

(a) (b)

Figure 4.34 SEM images of samples: (a) low magnification and (b) high magnification of the porous PTFE-Al-W composite sample containing fine W particles.

4.3.5.2 Microstructures after Plastic Deformation

Samples after different levels of plastic deformation were characterized by scanning electron microscopy to identify the failure mechanisms and microstructural evolution (Cai et al., 2007).

4.3.5.2.1 After Equal Channel Angular Pressing

CIPed PTFE-Al-W samples (small W, submicron size powder, density 6 g/cm^3) were heavily deformed using ECAP device shown below. The idea of this experiment was to compare microstructure of composite samples after high strain rate tests in drop weight device and in Hopkinson bar tests with microstructure after high strain and low strain rate deformation in ECAP device. Strain rate ($10^{-1}s^{-1}$) can be obtained based on time of experiment (20 s) and overall strain. After one pass, overall strain is about 2 according to the geometry of ECAP device. No visible fracture was visible. A secondary electron image of an ECAPed PTFE-Al-W sample is presented in Figure 4.35.

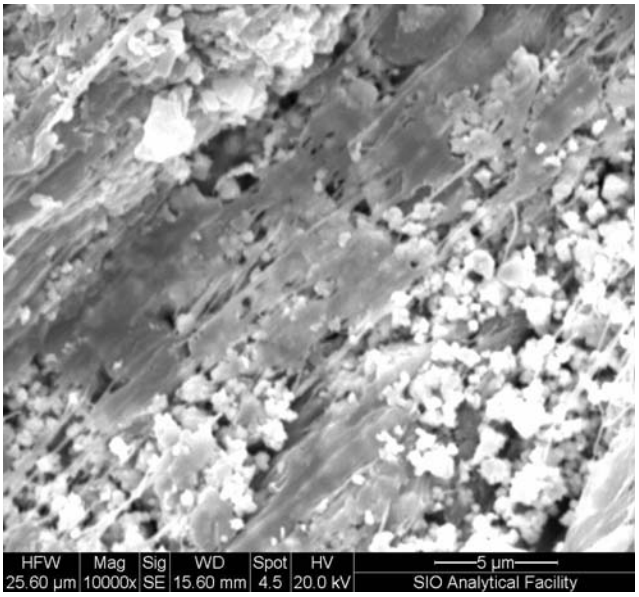

Figure 4.35 A secondary electron image of an ECAPed porous PTFE-Al-W sample containing fine W particle.

It has been observed that the fibers are formed in this relatively low strain-rate test similar to the dynamic case with strain-rate. The fibers appear in the area adjacent to the main crack too. In some regions, the films were observed in addition to fibers (Figure 36). It has been speculated that due to film instability under the stretching a film of PTFE could be split into the fibers.

4.3.5.2.2 After Hopkinson Bar Test

It has been discussed in Section 4.3.3 that porous PTFE-Al-W samples containing fine W particles have the higher strength than densified samples containing coarse W particles and porous samples containing coarse W particles. This fact was obtained from data in stress-strain curves. It is even reflected from the different fracture states of samples. All of porous samples containing coarse W particles were scattered into many

small fragments, because they were not pressured up to the limit in the CIP. From microscopic aspect, the initial PTFE particles (Figure 4.36) have developed into a continuous matrix (Figure 4.36 a). The interstices between PTFE particles and metal particles diminished. It looks like PTFE particles were melt. No distinctive PTFE fibers were found (Figure 4.36 b) to blunt cracks. Those visible fibers were probably developed during the manufacturing process. Unfractured spherical Al particles (~ 2mm) can be seen Figure 4.36 a.

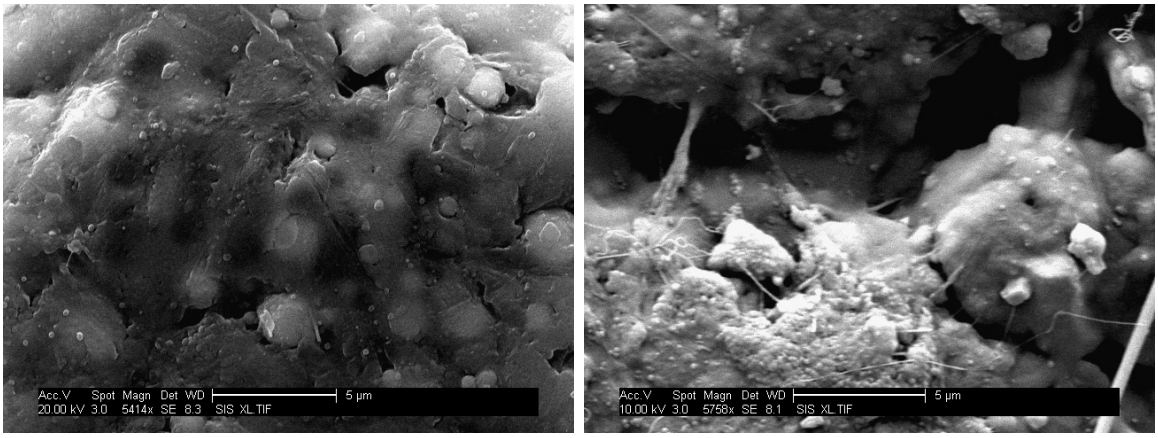

(a) (b)

Figure 4.36 SEM images of the porous composite PTFE-Al-W sample containing coarse W powder after Hopkinson Bar testing: (a) the PTFE particles melted around the metal particles; (b) sparse PTFE fibers.

Big irregular W particles can be seen in Figure 4.37a. No deformation of Al particles or W particles can be seen. Metal particles were separated from the matrix. It is clear that the PTFE matrix were stretched apart, forming fibers along stretching direction probably. It is due to the local adiabatic heating leading to crazing formation. Thin PTFE fibers were seen. Estimated from Figure 4.37 b, the diameter of them could be as low as 20 nm. The stretch and fibers formation of PTFE lead to the failure of samples.

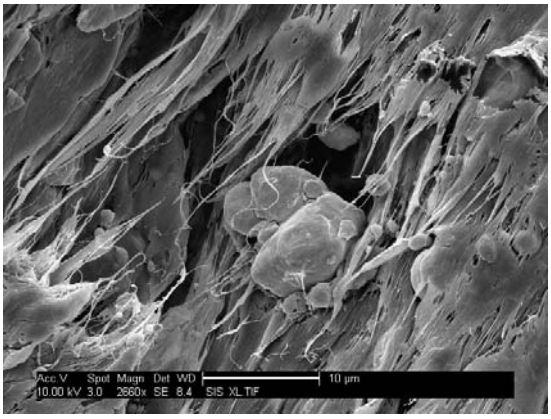

(a)

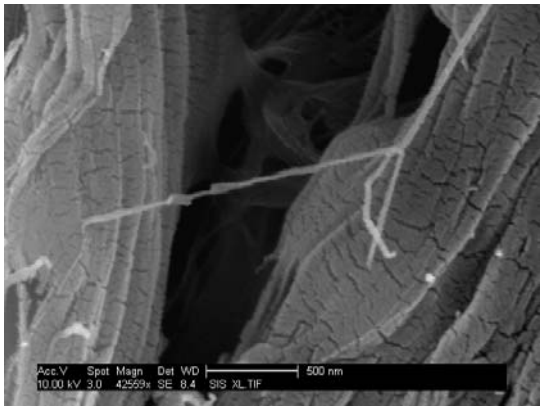

(b)

Figure 4.37 SEM images of the dense composite W/Al/PTFE sample containing coarse W powder: (a) PTFE was fractured and fibers connecting to metal particles; (b) the diameter of the thin fibers was estimated to 20 nm.

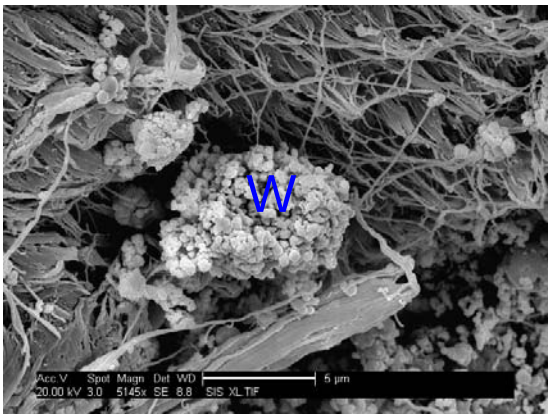

(a)

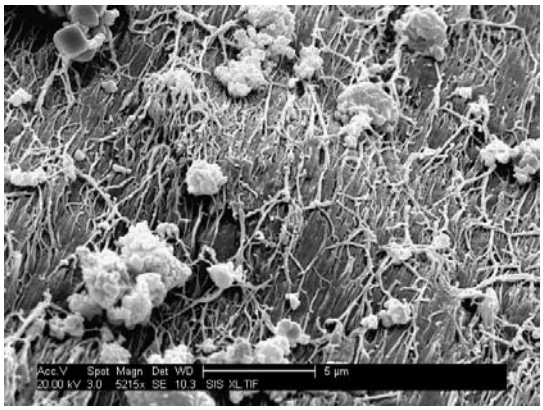

(b)

Figure 4.38 SEM images of the porous composite PTFE-Al-W sample containing fine W powder: (a) the agglomeration of W powder; (b) thick PTFE fibers.

The fractured surface of a porous PTFE-Al-W sample containing fine W particles is shown in Figure 4.38. The agglomeration of W is obvious. More PTFE fibers were formed, generating an intensive network of fibers to sustain higher stress. It is obvious

that the diameter of the fibers was larger than that of the densified sample containing coarse W particles.

The severe deformation of PTFE matrix is presented in all types of PTFE-Al-W samples. No deformed metal particles were detected. The deformation of PTFE could be melting in porous samples with coarse W particles, or formation of film or fibers in the other two cases. Debonding of metal particles from the matrix and the fracture of matrix were speculated to be two major mechanisms for the failure of the samples.

4.3.5.2.3 After Conventional Drop-weight tests

Figure 4.39 shows the top surface of a sample deformed with the 2 μm Al ring confinement.

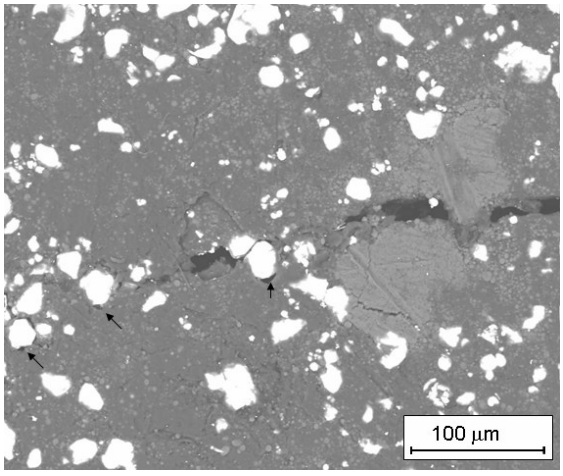

Figure 4.39 Crack propagation through composite showing separation of W and PTFE interface (indicated by arrows).

A few cracks could be seen, and their observation enables the conclusion that failure starts at the W- PTFE/Al interfaces. Three areas where separation has started are indicated by arrows in Figure 4.39. The small (2 μm) Al particles are more clearly visible in Figure 4.38 than in Figure 4.30b.

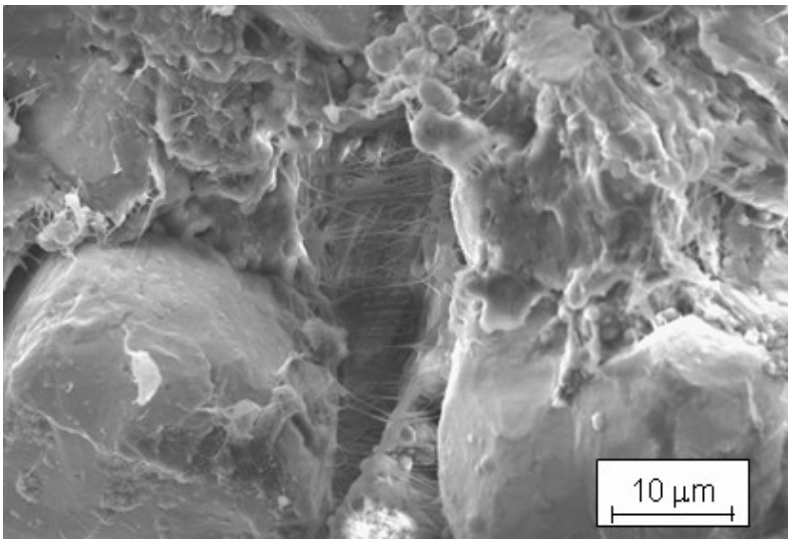

(a)

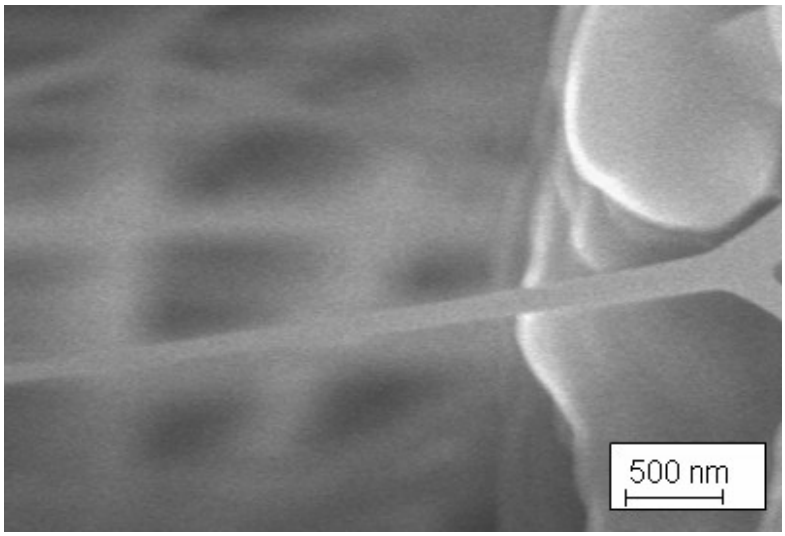

(b)

Figure 4.40 PTFE fibers formed by opening crack: (a) overall view; (b) detail.

Observation of a fracture surface (Figure 4.39) reveals three features: undeformed W particles, undeformed Al particles and highly deformed PTFE forming long strings in some places. In areas where large localized separation occurred, these strings form a dense network (Figure 4.40(a)). A detailed view of one of these fibers is shown in Figure 4.40(b). Their diameter is as low as 60-100 nm. In this sense, they can be termed nanofibers.

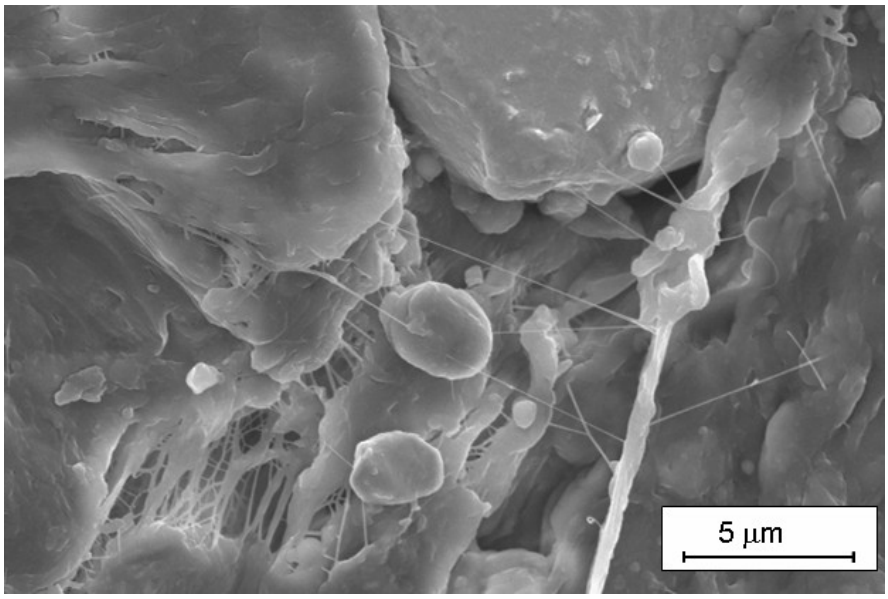

Figure 4.41 Network of PTFE micro-fibers formed along crack.

A network of these PTFE nanofibers is also shown in Figure 4.41. There is evidence of crazing. It has been observed by Brown et al. [172] that PTFE forms fibers when it is deformed at temperature above 30^{o}C. The formation of these thin fibers is connected with the crazing phenomenon, with fibers providing additional resistance for a propagating crack. They are most likely the result of the heating of PTFE due to adiabatic

deformation. This PTFE is bonded to the W particles in places and, upon fracture and separation of the W particles, is stretched into fibers to dissipate energy [173] and stabilize crack tips [174,175]. The pressed but not sintered PTFE in the investigated composites deformed in a different fashion than the sintered PTFE when it was tested in Mode I fracture (tension samples) [172]. The PTFE in our samples was deformed with sparse fibers formation and considerable cleavage. The similar behavior was exhibited in Mode II (shear loading) fracture testing by Brown et al. [172]. It should be noticed that the PTFE fibers in our samples are much thinner (60-100nm) than the fibers (~1μm) in the experiments by Brown et al. [172]. It is possible that good thermal conduction of metal particles (W and Al) leads to faster cooling of deformed polymer, resulting in more marked crazing and fine fibers.

4.3.6 Discussion and Conclusions

The behavior of high density polymer/metal composite energetic materials under various high rate mechanical stimulus was investigated. High strain-rate mechanical and microstructural properties of a composite system consisting of Teflon (PTFE), aluminum (Al) and tungsten (W) particles, with a density up to 7.2 g/cm^3 were presented. Two samples using different sizes of W particles were introduced to investigate the effect of particle size on the density (ρ) and the ultimate compressive strength (σ_f) of the materials.

Hopkinson bar testing was performed using a low-impedance magnesium transmitting bar. Drop-weight tests with various arrangements including free standing and jacketed samples were used to find the dynamic compressive strength with simple boundary conditions and to analyze microstructural development caused by high strain, high strain rate plastic flow and fracture.

We observed an unusual phenomenon when comparing samples with fine W particles with higher porosity to those with coarse W particles, which had a higher density. The samples with higher porosity exhibited a higher strength in both quasi-static and dynamic experiments. It is an interesting phenomenon since higher porosity usually leads to lower material strength.

In Hopkinson bar tests, the ultimate compressive strength of the high density PTFE-Al-W composite (ρ = 7 g/cm^3) with coarse W particles was σ_f = 24 MPa, while more porous PTFE-Al-W composite with fine W particles (ρ = 6 g/cm^3) had stress level as high as σ_f = 44 MPa. This tendency is consistent with data from a quasi-static tests where the ultimate compressive strength of the dense (ρ = 7 g/cm^3) PTFE-Al-W composite with coarse W particles was σ_f = 18 MPa and more porous PTFE-Al-W composite with fine W particles (ρ = 6 g/cm^3) exhibited strength σ_f = 24 MPa. Critical failure strains for both composites in quasi-static and dynamic tests are 4-5%.

A similar phenomenon of a significantly higher strength (σ_f = 55 MPa) of porous composites with fine W particles compared to the strength (σ_f = 32 MPa) of dense composites containing larger W particles was also observed in drop-weight tests.

We explain the higher strength phenomenon of these composite materials at relatively high porosity with fine W particles by the influence of force chains between metallic particles when they have small diameters. Two-dimensional numerical analysis of drop-weight tests (where the boundary conditions correspond to constant speed of dropped weight) revealed that small particles create force chains that augment the effective global strength of porous granular materials. Based on the densities of tapped composite materials, we consider that force chains are not significant in the composite containing large W particles with the same volume fraction as samples with small W particles. Two dimensional analysis predicted critical strain of developing of first macrocraking about two times smaller than critical strain of failure of PTFE matrix due to strain concentration caused by practically undeformed metal particles.

The high-strain, high strain-rate experiments carried out on PTFE-Al-W granular composites with varying Al confinement rings reveal the characteristics of deformation and the strengths under high strain rate ($\sim 4\times10^{2}$ s^{-1}). The quasistatic flow stress is ~ 22 MPa and the dynamic flow stress is approximately 60-90 MPa. This is consistent with the constitutive description by Zerilli and Armstrong [169], assuming that deformation takes place mainly on the continuous PTFE matrix. In unconfined samples, failure by cracking and shear localization follows immediately the maximum stress. Confinement with aluminum rings enables plastic deformation to continue to high values (up to a strain of -0.875). PTFE attached to W particles is extended in fracture, creating a network of new fibers having diameters as low as 60 nm to bridge the crack plane to prevent crack propagation. Most of the plastic deformation takes places in the “soft” PTFE, and the W

particles remain virtually undeformed. It is this deformation that leads to the formation of the nanofibers.

Microstrutural observation of heavily deformed samples after drop-weight and Hopkinson bar tests revealed that most of the plastic strain is accommodated by a soft PTFE matrix with practically undeformed metal particles. The PTFE that is attached to W particles is extended in fracture, creating a network of nanofibers with diameters as low as 60 nm. For comparison we heavily deformed cold isostatically pressed PTFE-Al-W samples (submicron size W powder with a density of $\rho = 6$ g/cm^3) using Equal-Channel Angular Pressing (ECAP) and also observed nanoscale size PTFE films. Hollow cylindrical samples of composites were collapsed using a Hopkinson bar based thick walled cylinder (TWC) method. We did not observe a chemical reaction in this system in these conditions of static and dynamic loading.

4.4 Carbon Fibers Filled Al Alloys

Carbon fibers are widely used in composites to tailor the strength and modulus and to decrease the density of composites [176-179]. Many studies have focused on the interfacial properties, seeking to improve the bonding between carbon fibers and the matrix [180-182], and on the influence of the carbon fiber content in the composites [183-185]. Recently, some researchers started to pay attention to the dynamic response of carbon fiber reinforced metal matrix composites [186,187].

The present investigation is aimed at: (a) establishing the effect of the carbon fiber (pitch-based and PAN-based (polyacrylonitrile)) on the mechanical response and strain-rate sensitivity of Al-Mg metal; (b) determining the failure evolution mechanism and the effect of the orientation of carbon fibers on the strength of the composites.

The composites being investigated were developed for tailored coefficients of thermal expansion and heat conductivity. The applications are in electronic thermal management, wireless communication systems, heat sinks for phased array radar antennas, and base plate applications for commercial power semiconductors used in hybrid electric vehicles (HEV) and static transfer switching technology. For instance, the addition of 30% graphite fibers decreases the CTE from $24x10^{-6}$/K to ~$8x10^{-6}$/K. The compressive strength of the Metal Matrix Cast Composite METGRAFTM is approximately 200 MPa. The manufacturing procedure is described by Cornie and Zhang [188].

The addition of carbon fibers is instrumental to control distributed fracture under dynamic conditions without sacrificing material strength. These composites can be also used as components in reactive materials, for example in mixture with Teflon [189,190].

Compression and forced shear loading were utilized to investigate the quasi-static and dynamic response of carbon fiber/Al-Mg composites. Two types of carbon fibers (PAN-based (C_{PAN}) and pitch-based (C_{Pitch})) were introduced into an Al-Mg alloy matrix (~30 vol% fibers). The CPAN/Al-Mg composite had higher compressive and shear strengths than C_{Pitch}/Al-Mg regardless of fiber orientation. The difference in strength due to the nature of fibers was more significant than the effect of fiber orientation

(perpendicular or parallel to loading direction). The compressive strength of these composites exhibited strain-rate sensitivity comparable with that of an Al-Mg alloy and more pronounced for the C_{PAN}/Al-Mg composite. The microstructural features of shear flow in the localized shear zone in hat-shaped samples and the characteristics of fractured fibers are analyzed and discussed. Possible reaction of the metal matrix and carbon fibers was observed.

4.4.1 Sample configuration and testing techniques

Two composite materials were supplied by Metal Matrix Cast Composite, LLC. The C_{Pitch}/Al-Mg composite consisted of a 70 vol% metal matrix filled with 30 vol% pitch-based carbon fibers. The theoretical density is 2.47 g/cm^3. The density of the material was 2.43 g/cm^3 with a porosity of 1.6 %. The C_{PAN}/Al-Mg composite consisted of a 70 vol% metal matrix filled with 30 vol% PAN-based carbon fibers. The density of the material was 2.20 g/cm^3 with a porosity of 10.9 %. In certain circumstance, for reference purpose, tests were also run on the unfilled matrix material, Al-Mg, consisting of 90 wt% Al and 10 wt% Mg.

Milled pitch-base and milled PAN-base carbon fibers were used; these fibers were not chopped. The diameters of both types of fibers are 10 μm nominally. C_{pitch} has a nominal length of 200 μm while C_{PAN} about 300 μm. C_{PAN} was produced from PAN fiber after carbonization. C_{pitch} was produced from petroleum pitch after carbonization and then graphitization at an even higher temperature. C_{pitch} usually has lower tensile and

compressive strengths but a higher modulus than C_{PAN} [191]. There is no special treatment on the fibers to enhance the interfacial bonding between the metal matrix and fibers. The Mg infiltration was performed at a temperature of about 7500C. The specimens were machined in either a milling machine or a lathe via common Mg machining protocol without using any coolant.

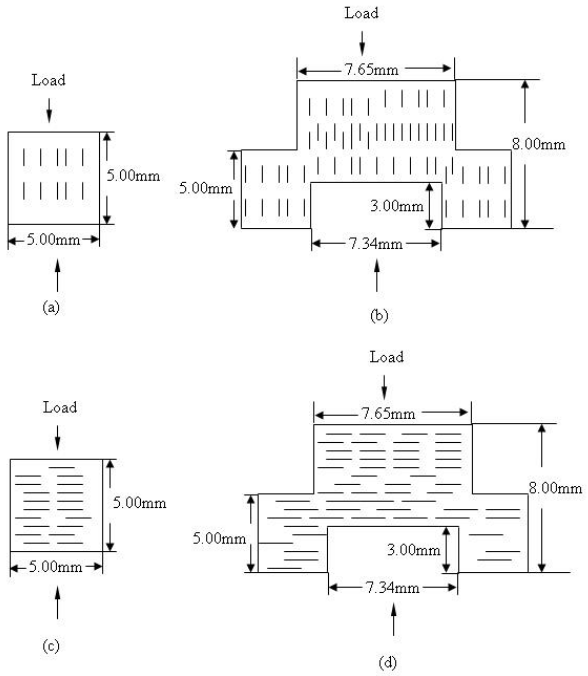

Figure 4.42 Geometry of cylindrical and hat-shaped samples: (a, b) fibers oriented parallel to (||) loading direction; (c, d) fibers perpendicular ($\perp$) to loading direction.

Quasi-static compression tests were performed using Instron 3367 with a 30 kN loading capacity. Hopkinson bar compression tests [96,114] were used to investigate the high-strain-rate compressive response of cylindrical specimens and the shear strength of hat-shaped specimens. Cylindrical specimens were tested at different strain rates. The estimated shear strain rate for the hat-shaped specimen is 35000 s^{-1}. The geometry of the corresponding specimens is shown below in Figure 4.42. Loading was carried out

perpendicularly ($\perp$) or parallel (||) to carbon fibers. The parallel (||) and perpendicular ($\perp$) orientations are shown with the schematic fiber directions (Figure 4.42).

4.4.2 Quasi-static and Hopkinson bar compression tests

The quasi-static stress-strain curves of materials are shown in Figure 4.43. The C_{PAN}/Al-Mg (PAN $\perp$ and PAN ||) has a higher compressive strength than C_{pitch}/Al-Mg (Pitch $\perp$ and Pitch ||). This response is consistent with the fact that PAN-based carbon fibers usually have a higher strength than pitch-based carbon fibers. The compressive strength of the metal matrix (Al-Mg) is higher than that of the C_{pitch}/Al-Mg and lower than that of C_{PAN}/Al-Mg. Meanwhile, the metal matrix presents much higher strain at the fracture (~50%) than both composites (~10% and ~20%). This is due to (a) both pitch-based carbon fiber and PAN-based carbon fiber have much lower critical strains [192]; (b) the low interfacial strength between the fibers and the metal matrix; and (c) the generation of micro-cracks in the composite upon loading.

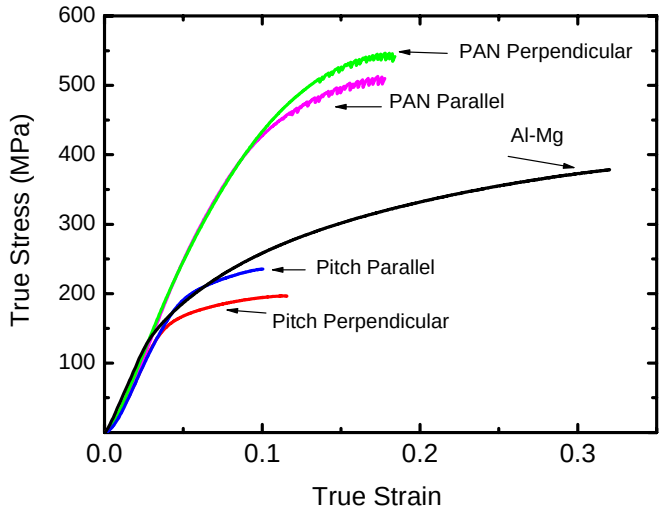

Figure 4.43 Cylindrical samples under quasistatic compression (~10^{-3} s^{-1}).

It is proposed that the change in elastic moduli with load in Figure 4.43 is due to micro-cracks produced in the compression process. It is known (e.g. Salganik [193] , and O'Connell and Budiansky [194]) that micro-cracks decrease the elastic modulus. The following expression was developed by O'Connell and Budiansky [194]:

$$E = E_0(1-163Na^3) = E_0(1-1.63D),$$

where N is the number of cracks per unit volume, a the radius of a mean crack, and , where D is a damage parameter. Li et al. [195] applied this equation to a material in which the damage changes with strain, ε, as $D = D_0 + K\varepsilon^n$, where D_0 is the initial damage and n is a damage accumulation parameter. Therefore, the stress σ is obtained as followed:

$$\sigma = E_0[(1-1.63D)\varepsilon - \frac{1.63K\varepsilon^{n+1}}{n+1}].$$

It can be seen that this is a non-linear relationship between σ and ε. The second term in the above equation is negative and decreases the slope in a stress-strain curve. Thus, damage accumulation at the extremities of the fibers (Figure 3) can lead to a concave curve and a decrease in modulus as shown in Figure 2. This is an alternative explanation to work hardening.

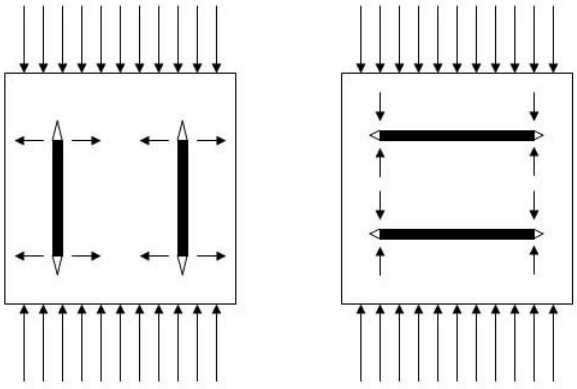

(a) (b)

Figure 4.44 Schematic drawing showing (a) opening of micro-cracks around fibers when parallel (||) to loading direction; (b) closing of micro-cracks around fibers when perpendicular ($\perp$) to loading direction.

The results of Hopkinson bar compressive tests, consistently with the quasi-static results, are presented in Figure 4.45. C_{PAN}/Al-Mg has a higher compressive strength than both C_{Pitch}/Al-Mg and the Al-Mg matrix. The dependence of compressive strength on strain rate can also be clearly seen in Figure 4.45. The higher the strain rate, the higher compressive strength both materials possess. Carbon fibers are usually strain rate insensitive [196], while the metal matrix (Al-Mg) is strain-rate sensitive, as shown in Figure 4.45. It can be concluded that the strain-rate sensitivity of the composites is

mainly caused by the strain rate sensitivity of the metal matrix. The strain-rate dependence of the debonding process can also contribute to the global strength of composites. A typical stress-strain curve is also presented (Figure 4.45 b).

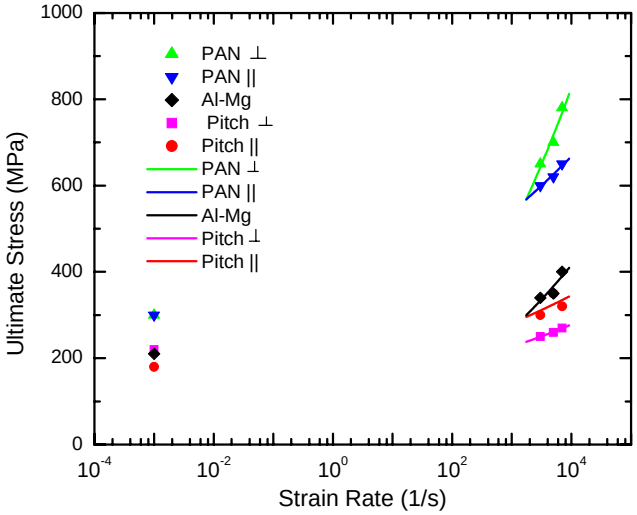

(a)

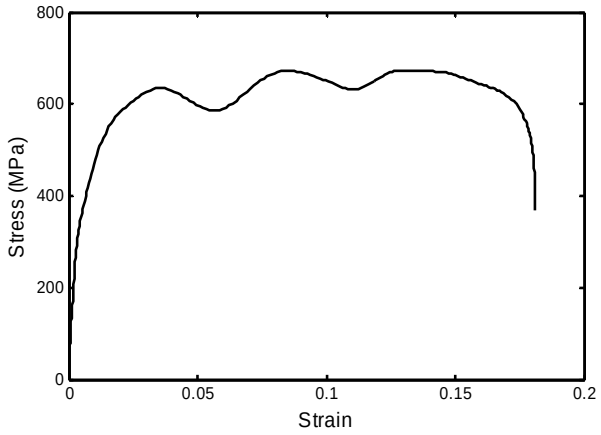

(b)

Figure 4.45 (a) Experimental data (all symbols) and fitted curves (only for the data from high-strain-rate deformation) of all materials; (b) stress-strain curve of a C_{PAN}/Al-Mg composite sample at 7000 s^{-1} deformation.

4.4.3 Hopkinson bar shear testing

Quasi-static tests (Figure 4.46) of the hat-shaped samples confirm that C_{PAN}/Al-Mg (PAN ⊥ and PAN ||) has a higher shear strength than Cpitch/Al-Mg (Pitch ⊥ and Pitch ||). The result is consistent with the fact that PAN-based carbon fibers usually have a higher tensile strength than pitch-based carbon fibers. The orientation of fibers did not have a significant impact on the shear strength of composites.

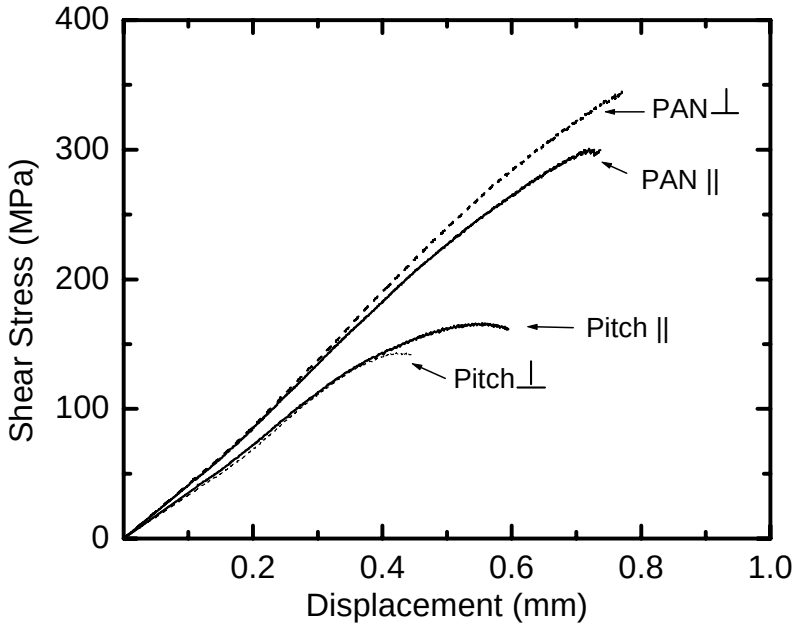

Figure 4.46 Data for hat-shaped samples of composite materials with different types and orientation of fibers under quasistatic compression.

The shear strain and strain rate in the hat-shaped sample can be estimated from the measured displacement as a function of time measured [115] and estimated thickness of the sheared region, in our case, using SEM micrograph. The schematic shear zones and plastic flow are illustrated in Figure 4.47. The average strain rate in the hat-shaped

samples is calculated from the velocity of the incident bar, v, divided by the thickness of the plastic deformation region, t: $\dot{\gamma} = v/t$. The velocity of the incident bar was 7 m/s. The thickness of the sheared region was measured from SEM micrograph of the sample and is approximately equal to ~ 200 μm (Figure 4.48). Therefore, the strain rate is:

$$\dot{\gamma} = v/t = 7/(200*10\text{-}6) = 3.5*104\ s^{-1}$$

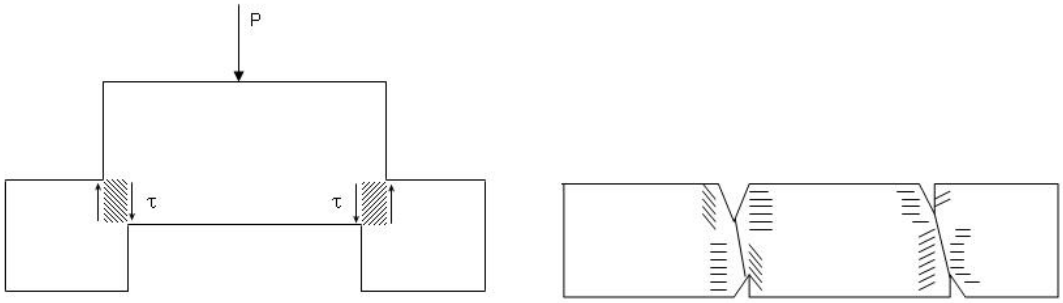

(a) (b)

Figure 4.47 (a) Schematic illustration of a hat-shaped sample undergoing Hopkinson bar test with shear zone shown by shaded areas, (b) Schematic illustration of plastic flow of material filed with fibers in the sheared zone after testing.

The stress state in the deformed region is fairly close to simple shear and the strain is approximately equal to the ratio between the critical shear displacement d (Figure 4.49) and the thickness of the deformed region, t (Figure 4.47):

$$\gamma = d/t = 0.15/0.2 = 0.75\,.$$

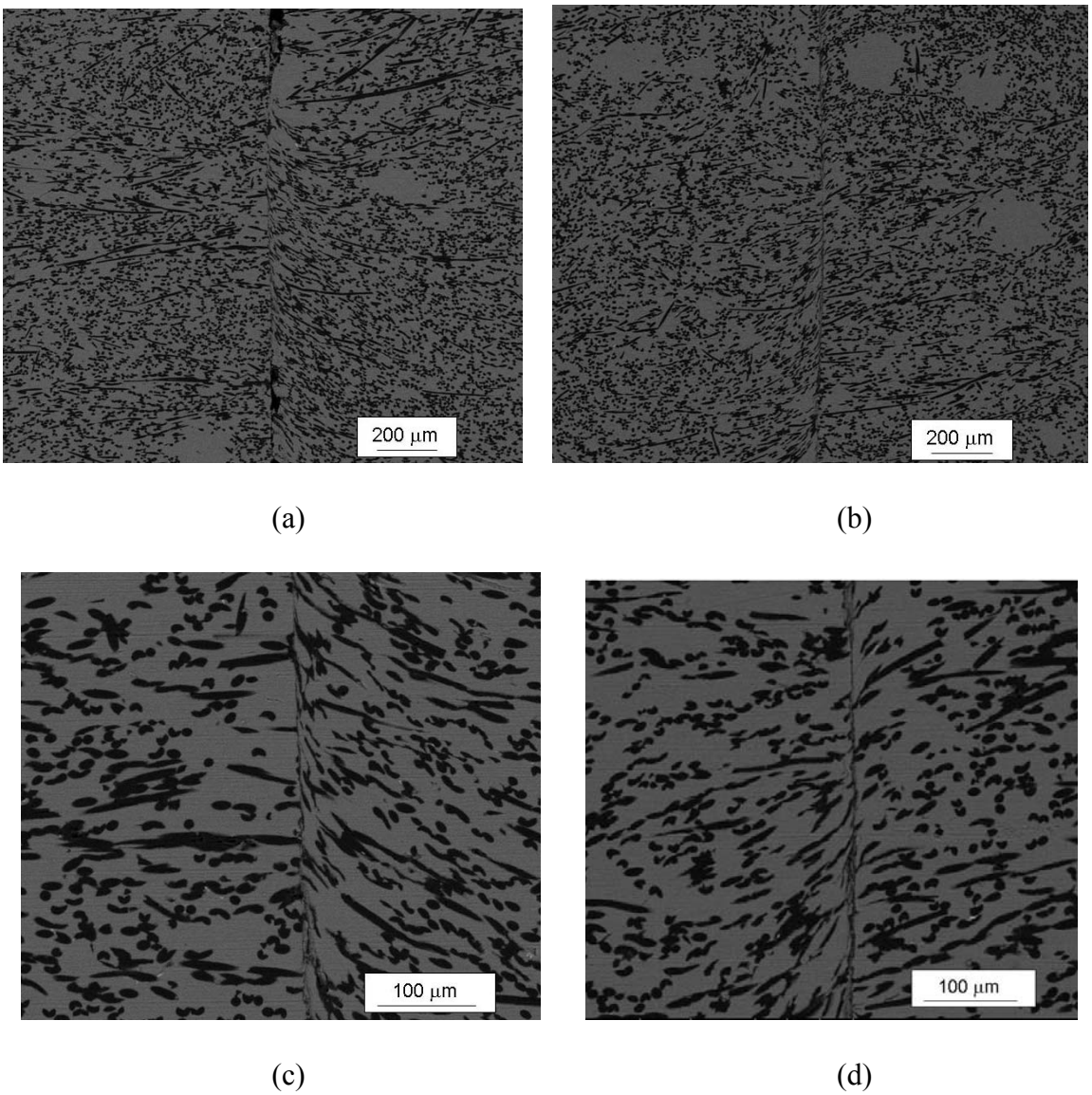

Figure 4.48 SEM micrographs exhibit the shear zone and plastic flow pattern in a C_{Pitch}/Al-Mg sample: (a) low magnification of shear zone (left hand side); (b) low magnification of shear zone (right hand side); (c) high magnification of shear zone (left hand side); (d) high magnification of shear zone (right hand side).

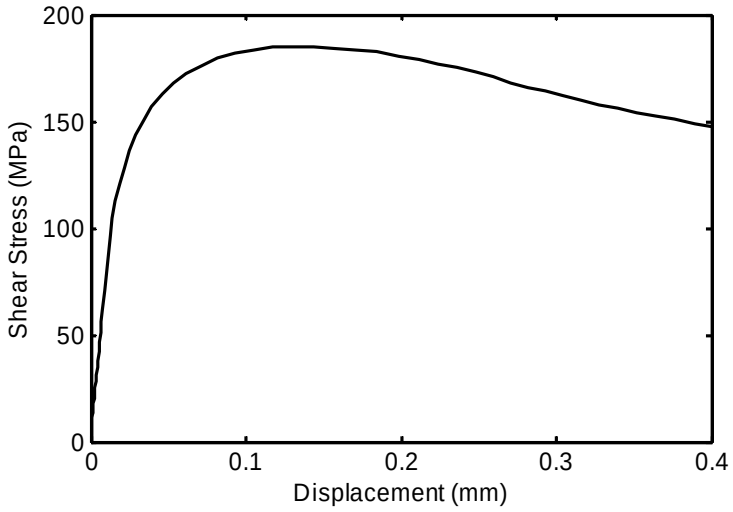

Figure 4.49 Shear stress-displacement curve of a hat-shaped C_{pitch}/Al-Mg sample.

Table 4.7 shows that the maximum average shear strength of composite samples did not depend significantly on fiber orientation (perpendicular and parallel to loading direction) for both the pitch-based carbon fibers and the PAN-based carbon fibers. The maximum average shear strength of C_{PAN}/Al-Mg (400 MPa) is almost twice that of C_{pitch}/Al-Mg (220 MPa) for both ($\perp$ or ||) orientations of the fibers. This phenomenon is consistent with the fact that PAN-based carbon fibers usually have a higher tensile strength than pitch-based carbon fibers. There is a tendency to higher critical displacements for samples filled with PAN-based carbon fibers probably because the PAN-based carbon fibers have a higher tensile strength than pitch-based carbon fibers. By contrast, the shear strength of the metal matrix is higher than those of C_{pitch}/Al-Mg but lower than those of C_{PAN}/Al-Mg. The critical displacement of the metal matrix samples is much larger than those of carbon fiber filled composites, because the carbon fibers are more brittle than the metal matrix. It means that Al based composites filled with fibers

may combine high shear strength and low critical shear strain, which may enhance bulk distributed fracture at impact.

Table 4.7 Maximum shear strength and critical displacements for dynamic hat-shaped sample tests.

Fiber type	Fiber Orientation to Loading Direction	Average Maximum Shear Strength (MPa)	Average Critical Displacement (μm)
pitch fiber filled	⊥	220	100
	||	220	200
PAN fiber filled	⊥	390	280
	||	400	320
No fiber (only metal matrix Al-Mg)		280	600

4.4.4 Microstructures

The microstructure of the hat-shaped samples of C_{pitch}/Al-Mg (fibers placed parallel to loading direction) is presented in Figure 4.50. It reveals that the failure mechanism of the sample includes both fracture and pull-out of fibers (arrows in the Figure 4.50 a). The characteristics of the fracture fibers in the present C_{pitch}/Al-Mg are similar to those in the high-modulus fiber/AM20-matrix composite [180], showing single-fiber fracture.

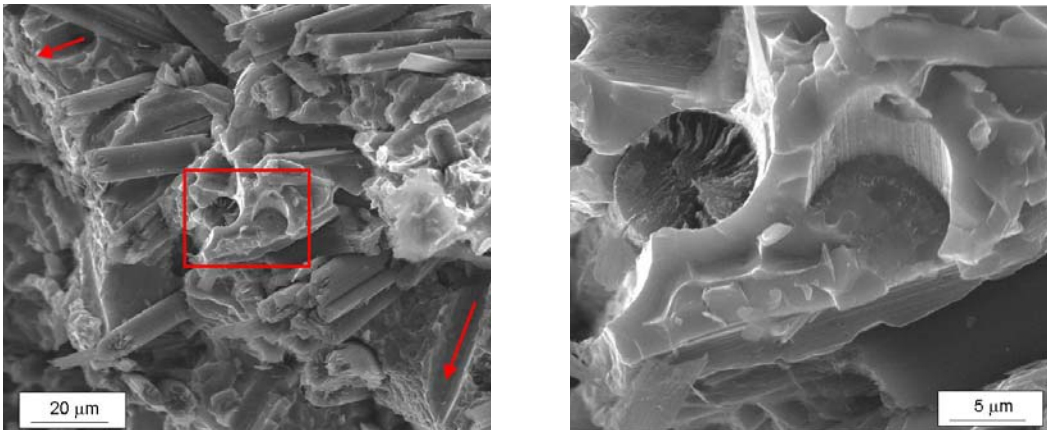

(a) (b)

Figure 4.50 Microstructure of a hat-shaped C_{pitch}/Al-Mg sample (fibers parallel to loading direction): (a) low magnification fracture and pullout (indicated by arrows) of fibers, (b) high magnification of the rectangular region in (a) shows fractured fibers.

The behavior of fibers placed perpendicular to loading direction inside the shear zone under high strain rate deformation is shown in Figure 4.51. Compared to the fibers parallel to loading direction, they were heavily bent. Fracture of the fibers related to the area of local tensile strains due to bending is noticeable (Figure 4.51 a). Fibers are also split or comminuted in the bending zone (Figure 4.51 b).

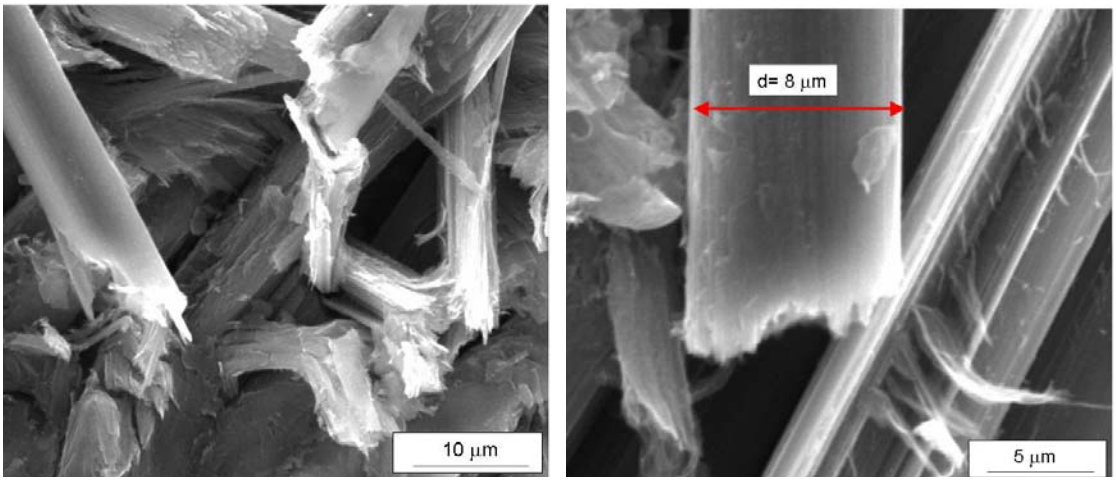

(a) (b)

Figure 4.51 SEM micrograph of a C_{pitch}/Al-Mg sample (fibers perpendicular to loading direction) showing (a) bent and fractured fibers, and (b) a split pitch-based carbon fiber.

Based on high resolution SEM imaging, Vezie and Adam [191] observed that high-compressive-strength PAN fibers usually had rough, granular textures and pitch fibers were with sheet-like structure which contributed to the low compressive strength of pitch fibers. SEM micrographs of PAN fibers in our samples (Figure 4.52 b) also display such texture. Compared to the failure mechanism of pitch fibers in the composite, the main reason attributed to the failure of PAN fibers is cracking (Figure 4.52 a). Figure 4.53 shows that cracks also propagated along the interface between the metal matrix and carbon fibers.

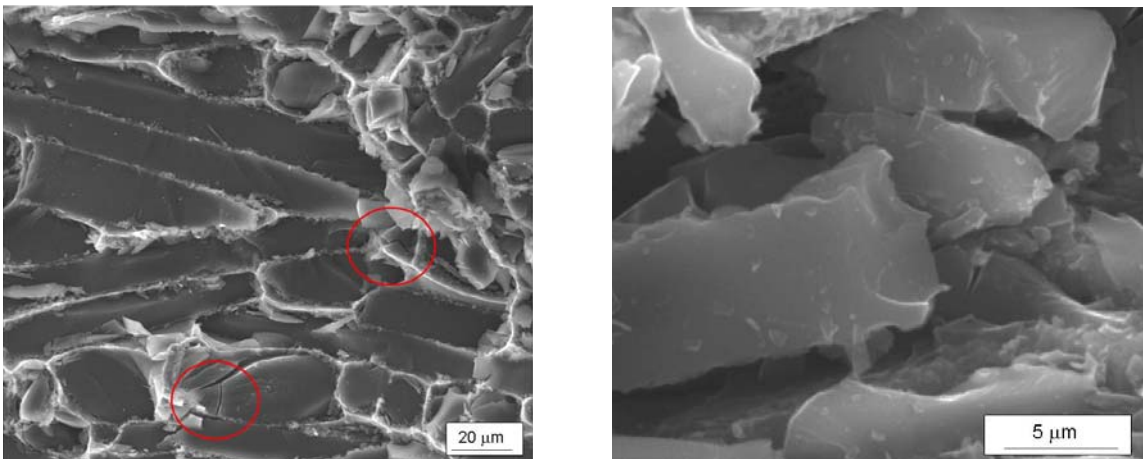

(a) (b)

Figure 4.52 Micrographs of fractured PAN-based carbon fibers in C_{PAN}/Al-Mg samples (fibers parallel to loading direction) show (a) cracks of fibers and (b) rough and granular texture of PAN fibers.

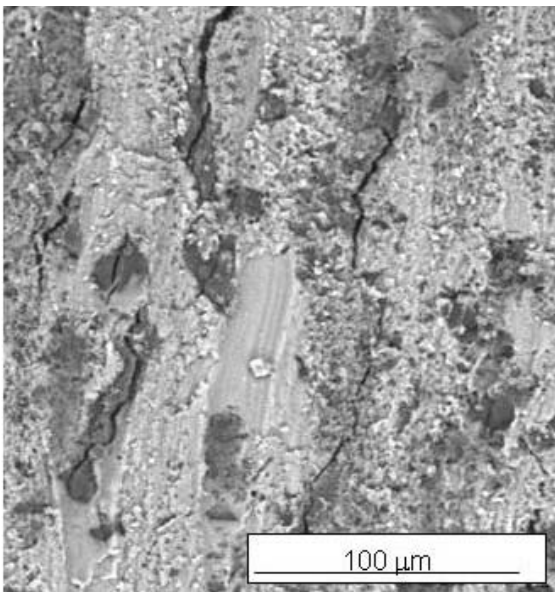

Figure 4.53 SEM micrograph showing cracks in the fracture surface of a C_{PAN}/Al-Mg sample (fibers perpendicular to loading direction).

Fibers seemed to be uniformly distributed in the undeformed part of a sample (Figure 4.54 a). However, a locally high concentration of fibers (Figure 4.54 b) in the ring part of the sample is shown. It can be speculated that the fracture of this part due to tensile stress tended to happen in the high concentration region of carbon fibers. It shows good agreement with one of research goals which is to use fibers to facilitate bulk distributed fracture (fragmentation) of the composites.

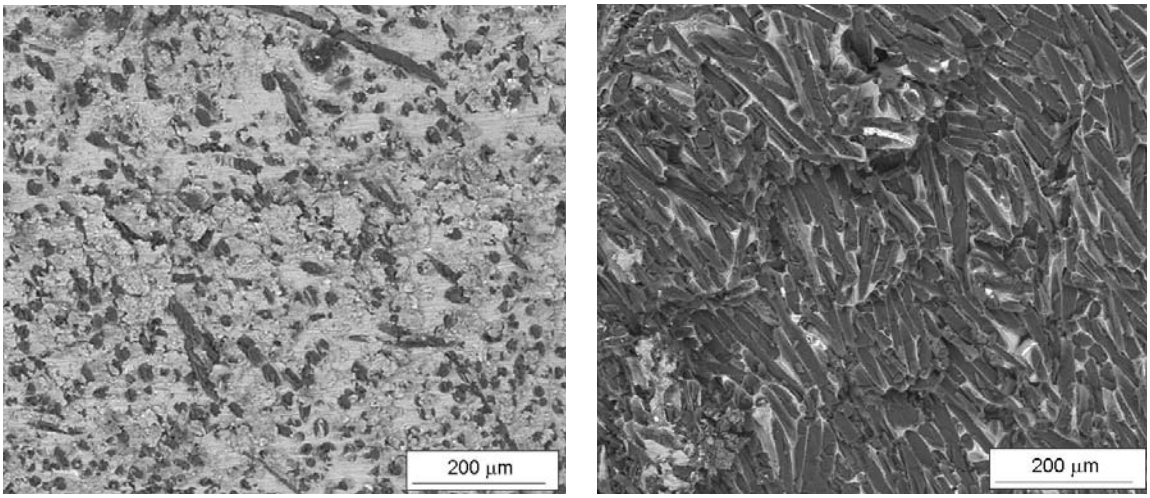

(a) (b)

Figure 4.54 SEM micrographs of the fractured ring part of a C_{PAN}/Al-Mg sample (fibers perpendicular to loading direction) shows: (a) low magnification of the external surface of undeformed sample showing fibers distributed uniformly; (b) fracture surface in region where the volume fraction of fibers (dark rods) is higher than 30%.

4.4.5 Fracture Characterization

We observed a broad distribution of values of critical strains which did not depend on strain rate, the nature of fibers or their orientation.

Samples were fractured mainly by macroshear in combination with bulk distributed damage. At high strain rates, the cylindrical samples were comminuted into a large number of small pieces. For the same strain rate, C_{pitch}/Al-Mg samples tended to be fragmented into more pieces than C_{PAN}/Al-Mg samples. This demonstrates that the fracture patterns are influenced by the nature of carbon fibers. The weaker pitch-based carbon fibers facilitate bulk distributed fracture, resulting in smaller size of fragments. This mode of fracture can be beneficial when this alloy is used as the metallic component in reactive materials.

Another interesting observation of the fragmented cylindrical samples after high-strain-rate deformation is the existence of some reddish fragmentation products (circles in Figure 4.55) among regular black pieces after tests. Such phenomenon was observed for samples at 5000 or 7000 s^{-1} deformation regardless of the type or the orientation of carbon fibers, but not for any samples under 3000 s^{-1} deformation. The difference in mechanical behavior for sample under different deformation condition may affect dissipated energy resulting in different input to their chemical transformation. It may conclude that these materials are insensitive to low-strain-rate deformation, but need a significant amount of mechanical work, for example under high-strain-rate plastic deformation, to drive the reaction [1]. It is obvious that further work is warranted in order

to determine the products of the possible reactions between Al and carbon fibers [197,198] and between magnesium and carbon fibers [199] are desirable.

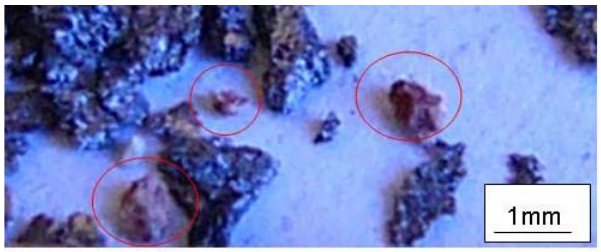

Figure 4.55 Reddish fragments observed among regular black scattered pieces after dynamic testing and comminution of C_{Pitch}/Al-Mg sample bulk damaged at high strain rate (5000 or 7000 s^{-1}).

The dynamic critical tensile strains for opening of macro-cracks can be estimated from the hat shaped samples based on the diameters of the hat part and of the hole. During the movement of the hat (with larger diameter: 7.65 mm) into the hole (smaller diameter: 7.34 mm) the maximum tensile (hoop) strains can be computed and are about 4%. The external ring fractured at this hoop strain. Thus, this value is an upper estimate for tensile strain for opening macro-cracks, because a crack could open at an intermediate stage of the penetration process of the hat part into the hole.

Metal matrix samples were deformed without developing shear macrocracking to the large values of compressive strains. This means that filling with fibers facilitates shear fracture at earlier stages of deformation irrespective of the strain rate. This can be beneficial for the initiation of the reaction between Al and carbon fibers and between Mg and carbon fibers, for example, to form Al_4C_3 [197,198] or Mg_2C_3 and MgC_2 [200] during fracture under dynamic compression.

4.4.6 Discussion and Conclusions

High-strain-rate testing was performed on carbon-fiber filled Al-Mg metal matrix composites. Experiments and analysis on the effect of the type and orientation of carbon fibers on the mechanical properties of the composites lead to the following conclusions:

(a) Quasistatic compression tests and dynamic Hopkinson Bar tests demonstrated that the compressive strength of composite samples depends significantly on strain rate regardless of fiber orientation (perpendicularly or parallel to the loading direction) both for C_{pitch}/Al-Mg and for C_{PAN}/Al-Mg. The compressive strength of composites increased with increasing strain rate mainly because of the strain-rate sensitivity of the metal matrix.

(b) Compressive strength and maximum average shear strength of C_{PAN}/Al-Mg samples are almost twice that of C_{pitch}/Al-Mg for both orientations of the fibers. This effect is consistent with the fact that PAN-based carbon fibers usually have higher compressive and tensile strength than pitch-based carbon fibers.

(c) The presence of fibers reduced the critical strain for fracture for both composites and enhanced bulk distributed fracture (fragmentation) under dynamic compressive and shear deformation.

(d) The microstructure of hat-shaped samples after high-strain-rate shear deformation reveals that fracture and pull-out of fibers were the major failure mechanisms of the C_{pitch}/Al-Mg with fibers parallel to loading direction. Bending and splitting of fibers were the major failure mechanisms of the C_{pitch}/Al-Mg with fibers

perpendicular to loading direction. Cracking of fibers and cracks along the interface between the metal matrix and carbon fibers were the major failure mechanism of the C_{PAN}/Al-Mg.

(e) A possible reaction of the metal matrix with carbon fibers led to the unusual reddish scattered pieces in the fragmented cylindrical samples under high-strain-rate compressive deformation (5000 or 7000 s^{-1}). Further investigation on it is necessary.

Chapter 4 incorporates results from the following publications: (1) "Effect of Strain Rate on the Compressive Mechanical Properties of Aluminum Alloy Matrix Composite Filled with Discontinuous Carbon Fibers", Jing Cai, Yuejian Chen, Vitali F. Nesterenko, Marc A. Meyers, Materials Science and Engineering A, accepted; (2) "High-Strain, High-Strain-Rate Flow and Failure in PTFE/Al/W Granular Composites", Jing Cai, Steve M. Walley, Richard J.A. Hunt, William G. Proud, Vitali F. Nesterenko, Marc A. Meyers, Materials Science and Engineering A, in press; (3) "Collapse of Hollow Cylinders of PTFE and Aluminum Particles Mixtures Using Hopkinson Bar", Jing Cai, Vitali F. Nesterenko, Proceedings of the Conference of the American Physical Society Topical Group on Shock Compression of Condensed Matter-2005, 2006, 793-796; (4) "Shear Localization and Patterning of Shear Bands In PTFE and Its Mixtures with Metals", Yabei Gu, Vitali F. Nesterenko, Jing Cai, Proceedings of the Conference of the American Physical Society Topical Group on Shock Compression of Condensed Matter-2003, 2004, 775-778. The author of the dissertation was the primary investigator and author of these papers.

CHAPTER 5

SUMMARY

The behavior of high density polymer/metal and carbon fibers filled Al alloy composite energetic materials under various high rate mechanical stimulus was investigated. The research provides new insights into the development of materials science of reactive materials.

Here is the summary of the dissertation.

In this research, a variety of heterogeneous energetic materials have been investigated. Their mechanical and dynamic properties and microstructure characteristics have been studied. In particular, special attention has been paid to the initiation of chemical reaction upon impact, the influence of filler on the properties of composites, and the dynamic behavior of thermites. The understanding of the background knowledge has been guiding me throughout the research.

A range of experimental techniques have been developed and applied in the investigation, including Hopkinson bar based small scale TWC testing and “soft” drop-weight testing. The majority of investigated materials were manufactured in house. They came from the powder state. To consolidate the mixture of powders, ball milling and Cold Isostatic Pressing were adopted to assemble high-density, high-accurate-dimension samples. Quasi-static, Hopkinson bar, and drop-weight tests were carried out to obtain

the compressive strengths of the composite materials. Conventional Thick-walled Cylinder (TWC) method and small-scale Hopkinson bar assisted TWC experiments were conducted to investigate shear bands and shear strengths. Recognizing the limit of applying conventional drop-weight approach for the soft material properties, a modified "soft" drop-weight method was proposed. The experimental results proved its validity. ECAP was employed to observe the materials' response to high-shear-strain. The microstructures and failure mechanisms of samples were examined using Scanning Electron Microscopy. Raman Spectroscopy was employed to detect the new products of chemical reaction of the materials.

The results of the study on the solid PTFE and PTFE-Sn composite showed that that strain softening was the main mechanism in initiation of shear bands in explosively driven TWC test of solid PTFE and PTFE-Sn samples were more stable than solid PTFE in terms of shear localization. The dynamic collapse of solid PTFE-Al samples with different particle sizes were accomplished with the shear localized bands and cracks. Microstrutural observation of the heavily deformed PTFE-Al-W samples revealed that most of the plastic strain is accommodated by a soft PTFE matrix with practically undeformed metal particles. It is found that force chains between the fine W particles contributed to the high strength of the porous PTFE-Al-W composite samples containing fine W particles. Formation of PTFE fibers due to probably locally adiabatic heating absorbed energy and blunted cracks. Comparing the mechanical properties of C_{pitch}/Al-Mg and C_{PAN}/Al-Mg with fibers placed along two orientations (parallel or perpendicular to loading direction) led to the conclusion that orientation of carbon fibers did not influence the strength and reaction of the composites. Compressive strength and

maximum average shear strength of C_{PAN}/Al-Mg specimens were almost twice that of C_{pitch}/Al-Mg for both orientations of the fibers. This fact was consistent with the fact that PAN-based carbon fibers usually have higher compressive and tensile strength than pitch-based carbon fibers. Studies also demonstrated that the presence of fibers reduced the critical strain for fracture for both composites and enhanced bulk distributed fracture under dynamic compressive and shear deformation.

REFERENCES

[1] R.G. Ames, Mater. Res. Soc. Symp. Proc. 896 (2006) 123-132.

[2] J.A. Joyce, P.J. Joyce, Eng. Fract. Mech. 71 (2004) 2513-2531.

[3] C.A. Sperati, H.W. Starkweather, Adv. Polym. Sci. 2 (1961) 465-495.

[4] J.M. Boteler, AIP Conference Proceedings 429 (1998) 537-540.

[5] B. Yang, V. Kozey, S. Adanur, S. Kumar, Composites Part B: Engineering 31 (2000) 715-721.

[6] M.Z. Shah Khan, G. Simpson, E.P. Gellert, Composites Part A: Applied Science and Manufacturing 31 (2000) 57-67.

[7] C. Thaumaturgo, Da Costa, A. M. Jr., J. Mater. Sci. Lett. 16 (1997) 1480-1482.

[8] I. Ikejima, R. Nomoto, J.F. McCabe, Dental Materials 19 (2003) 206-211.

[9] W. Bonfield, M.D. Grynpas, A.E. Tully, J. Bowman, J. Abram, Biomaterials 2 (1981) 185-186.

[10] K.E. Tanner, R.N. Downes, W. Bonfield, Br. Ceram. Trans. 93 (1994) 104-107.

[11] Y.C. Chen, H.C. Lin, Y.D. Lee, J. Polym. Res. 10 (2003) 247-258.

[12] Y. Nakamura, M. Yamaguchi, M. Okubo, T. Matsumoto, J Appl Polym Sci 45 (1992) 1281-1289.

[13] M.S. Korobov, G.Y. Yurkov, A.V. Kozinkin, Y.A. Koksharov, I.V. Pirog, S.V. Zubkov, V.V. Kitaev, D.A. Sarychev, V.M. Buznik, A.K. Tsvetnikov, S.P. Gubin, Inorganic Materials 40 (2004) 26-34.

[14] R.W. Johnson, P.W. Montgomery, D.L. O'Brien, Materials Engineering 66 (1967) 74-76.

[15] J. Jang, H.S. Kim, J Appl Polym Sci 60 (1996) 2297-2306.

[16] N.A. St John, J.R. Brown, Composites Part A-Applied Science and Manufacturing 29 (1998) 939-946.

[17] H. Hamada, K. Fujihara, A. Harada, Composites Part A-Applied Science and Manufacturing 31 (2000) 979-990.

[18] Y. Xue, X. Cheng, J. Mater. Sci. Lett. 20 (2001) 1729-1731.

[19] H. St. Germain, M.L. Swartz, R.W. Phillips, B.K. Moore, T.A. Roberts, J. Dent. Res. 64 (1985) 155-160.

[20] Y. Li, M.L. Swartz, R.W. Phillips, B.K. Moore, T.A. Roberts, J. Dent. Res. 64 (1985) 1396-1401.

[21] S. Suzuki, K.F. Leinfelder, K. Kawai, Y. Tsuchitani, Am. J. Dent. 8 (1995) 173-178.

[22] G. Landon, G. Lewis, G.F. Boden, J. Mater. Sci. 12 (1977) 1605-1613.

[23] W.M. Baldin, ACTA MECH 6 (1958) 141.

[24] F.F. Lange, Journal of the American Ceramic Society 54 (1971) 614.

[25] H. Hojo, M. Tamura, N. Kawamura, Polymer Engineering and Science 14 (1974) 604-609.

[26] F.F. Lange, K.C. Radford, J. Mater. Sci. 6 (1971) 1197-1203.

[27] S. Ahmed, F.R. Jones, J. Mater. Sci. 25 (1990) 4933-4942.

[28] A.G. Evans, Philosophical Magazine 26 (1972) 1327-&.

[29] L.J. Broutman, S. Sahu, Materials Science and Engineering 8 (1971) 98-&.

[30] M. Wang, R. Joseph, W. Bonfield, Biomaterials 19 (1998) 2357-2366.

[31] J. Spanoudakis, R.J. Young, J. Mater. Sci. 19 (1984) 473-486.

[32] L.L. Wang, Z.A. Munir, Y.M. Maximov, J. Mater. Sci. 28 (1993) 3693-3708.

[33] H. Goldschmidt, Iron Age 82 (1908) 232.

[34] A.G. Strunina, T.M. Martemyanova, V.V. Barzykin, V.I. Ermakov, Combustion Explosion and Shock Waves 10 (1974) 449-455.

[35] V.I. Ermakov, A.G. Strunina, V.V. Barzykin, Combustion Explosion and Shock Waves 14 (1978) 723-730.

[36] S.V. Kostin, A.G. Strunina, V.V. Barzykin, Combustion Explosion and Shock Waves 18 (1982) 524-529.

[37] S.M. Walley, J.E. Balzer, W.G. Proud, J.E. Field, Proceedings of the Royal Society of London Series A-Mathematical Physical and Engineering Sciences 456 (2000) 1483-1503.

[38] Y.X. Li, J.K. Yao, Y. Liu, Surf Coat Technol 172 (2003) 57-64.

[39] T.M. Yue, K.J. Huang, H.C. Man, Surf Coat Technol 194 (2005) 232-237.

[40] J.E. Field, G.M. Swallowe, S.N. Heavens, Proceedings of the Royal Society of London Series A 382 (1982) 231-&.

[41] J.E. Field, N.K. Bourne, S.J.P. Palmer, S.M. Walley, J.M. Smallwood, Philosophical Transactions of the Royal Society of London Series A 339 (1992) 269-283.

[42] C.M. Tarver, S.K. Chidester, A.L. Nichols, J. Phys. Chem. 100 (1996) 5794-5799.

[43] Bowden FP, Yoffe AD. Fast reactions in solids. London: Butterworths, 1958.

[44] F.P. Bowden, O.A. Gurton, Proc. R. Soc. Lond. A 198 (1949) 337-349.

[45] G.M. Swallowe, J.E. Field, Proc. R. Soc. Lond. A 379 (1982) 389-408.

[46] G.R. Kamat, C.K. Gupta, Metallurgical Transactions 2 (1971) 2817-&.

[47] O.K. Mehra, D.K. Bose, C.K. Gupta, Metallurgical Transactions 4 (1973) 691-694.

[48] R.A. Cutler, K.M. Rigtrup, A.V. Virkar, J Am Ceram Soc 75 (1992) 36-43.

[49] V. Sundaram, K.V. Logan, R.F. Speyer, J. Mater. Res. 12 (1997) 1681-1684.

[50] Swalin RA. Thermodynamics of solids. 2nd ed. USA: Wiley-Interscience, 1972.

[51] M. Jou, J. Mater. Process. Technol. 132 (2003) 102-113.

[52] T.A. Siewert, Welding Journal 67 (1988) 17-23.

[53] X.L. Zhe, C.A. Dioka, A. Hendry, Journal of the European Ceramic Society 25 (2005) 695-702.

[54] M. Maeda, T. Yahata, K. Mitugi, T. Ikeda, Materials Transactions Jim 34 (1993) 599-603.

[55] H.S. Ray, B. Sarangi, A. Sarangi, Scand J Metall 25 (1996) 256-264.

[56] A. Biswas, I.G. Sharma, G.B. Kale, D.K. Bose, Metallurgical and Materials Transactions B-Process Metallurgy and Materials Processing Science 29 (1998) 309-315.

[57] Odawara O. Method for providing ceramic lining to a hollow body by thermit reaction . US Patent No. 4363832, 1982.

[58] O. Odawara, J. Ikeuchi, J. Am. Ceram. Soc. 69 (1986) C80-C81.

[59] O. Odawara, J. Ikeuchi, J. Am. Ceram. Soc. 69 (1986) C85-C86.

[60] O. Odawara, in: Z.A. Munir, J.B. Holt (Eds.), Combustion and Plasma Synthesis of High-Temperature Materials, Wiley, New York, 1990, pp. 179-185.

[61] K. Choo, M.W. Baker, T.C.A. Molteno, S.W. Morris, Physical Review E 58 (1998) 6115-6123.

[62] J.M. Huntley, Philosophical Transactions of the Royal Society of London Series A-Mathematical Physical and Engineering Sciences 356 (1998) 2569-2590.

[63] X. Xu, N.N. Thadhani, J. Appl. Phys. 96 (2004) 2000-2009.

[64] N.N. Thadhani, J. Appl. Phys. 76 (1994) 2129-2138.

[65] M.A. Meyers, L. Yu, K.S. Vecchio, Acta Metallurgica et Materialia 42 (1994) 715-729.

[66] K.S. Vecchio, L. Yu, M.A. Meyers, Acta Metallurgica et Materialia 42 (1994) 701-714.

[67] D.E. Eakins, N.N. Thadhani, J. Appl. Phys. 101 (2007) 043508.

[68] N.K. Bourne, G.T. Gray, J. Appl. Phys. 98 (2005) 123503.

[69] J.C.F. Millett, N.K. Bourne, J. Appl. Phys. 89 (2001) 2576-2579.

[70] J.C.F. Millett, N.K. Bourne, J. Appl. Phys. 88 (2000) 7037-7040.

[71] N.K. Bourne, J.C.F. Millett, G.T. Gray III, P. Mort, in: M.D. Furnish, N.N. Thadhani, Y. Horie (Eds.), Shock Compression of Condensed Matter 2001, American Institute of Physics, Melville, NY, 2002, pp. 653-656.

[72] M.R. Baer, Journal of Applied Mechanics-Transactions of the Asme 55 (1988) 36-43.

[73] O.V. Roman, V.F. Nesterenko, I.M. Pikus, Combustion, Explosion, and Shock Waves (English Translation of Fizika Goreniya i Vzryva) 15 644-649.

[74] Nesterenko VF. Dynamics of heterogeneous materials. New York: Springer-Verlag, 2001.

[75] C.E. Weir, J. Res. Natl. Bur. Stand. 53 (1954) 245.

[76] C. Wu, M. Nicol, Chemical Physics Letters 21 (1973) 153-157.

[77] E.S. Clark, Polymer 40 (1999) 4659-4665.

[78] S.S. Hambir, J.P. Jog, V.M. Nadkarni, Polymer Engineering and Science 34 (1994) 1065-1069.

[79] R.G. Ames, S.S. Waggener, 32nd International Pyrotechnics Seminar (2005).

[80] W.J. Mock, W.H. Holt, Shock Compression of Condensed Matter-2005 (2006) 1097-1100.

[81] J.E. Field, S.M. Walley, W.G. Proud, H.T. Goldrein, C. Siviour, Int. J. Impact Eng. 30 (2004) 752-775.

[82] A. Bakhshai, V. Soika, M.A. Susol, L. Takacs, Journal of Solid State Chemistry 153 (2000) 371-380.

[83] R. Sundaresan, F.H. Froes, J. Met. 39 (1987) 22-27.

[84] T. Venugopal, K.P. Rao, B.S. Murty, Journal of Nanoscience and Nanotechnology 7 (2007) 2376-2381.

[85] K.C.B. Yeong, J. Wang, S.C. Ng, Biomaterials 22 (2001) 2705-2712.

[86] J.S. Benjamin, Sci. Am. 234 (1976) 40-49.

[87] J.S. Benjamin, Metallurgical Transactions 1 (1970) 2943-&.

[88] V.M. Segal, V.I. Reznikov, A.E. Drobyshevsky, V.I. Kopylov, Russian Metall. 1 (1981) 99.

[89] Y. Iwahashi, M. Furukawa, Z. Horita, M. Nemoto, T.G. Langdon, Metallurgical and Materials Transactions 29 (1998) 2245-2252.

[90] M. Furukawa, Z. Horita, M. Nemoto, T.G. Langdon, J. Mater. Sci. 36 (2001) 2835-2843.

[91] A. Mishra, B.K. Kad, F. Gregori, M.A. Meyers, Acta Materialia 55 (2007) 13-28.

[92] H.J. Bohm, Advanced Engineering Materials 6 (2004) 626-633.

[93] J. Njuguna, K. Pielichowski, Advanced Engineering Materials 6 (2004) 204-210.

[94] A. Mishra, (2007) 53-54.

[95] Y. Iwahashi, J. Wang, Z. Horita, M. Nemoto, G. Langdon, Scr. Mater. 35 (1996) 143-146.

[96] H. Kolsky, Proceedings of the Physical Society Section B 62 (1949) 676-700.

[97] Gray, G. T. III, in: H. Kuhn, D. Medlin (Eds.), ASM Handbook-- Volume 8 Mechnical Testing and Evaluation, ASM International, Materials Park, Ohio, 2000, pp. 462-487.

[98] E.D.H. Davies, S.C. Hunter, Journal of the Mechanics and Physics of Solids 11 (1963) 155-179.

[99] C.A. Ross, D.M. Jerome, J.W. Tedesco, M.L. Hughes, ACI Mater. J. 93 (1996) 293-300.

[100] W. Chen, G. Ravichandran, J. Mech. Phys. Solids 45 (1997) 1303-1328.

[101] L. Ninan, J. Tsai, C.T. Sun, Int. J. Impact Eng. 25 (2001) 291-313.

[102] B. Wang, S. Yi, J. Mater. Sci. Lett. 21 (2002) 697-698.

[103] K.C. Ong, V.B.C. Tan, C.T. Lim, E.H. Wong, X.W. Zhang, Electronic Components and Technology Conference, 2004. Proceedings. 54th (2004) 1075-1079.

[104] B. Hopkinson, Philos. Trans. Roy. Soc. A 213 (1914) 437-456.

[105] P.S. Follansbee, in: H. Kuhn, D. Medlin (Eds.), ASM Metals Handbook, Volume 8, 9th edtion: Mechanical Testing, American Society for Metals, Metals Park, OH, 1985, pp. 198-217.

[106] G. Ravichandran, G. Subhash, J. Am. Ceram. Soc. 77 (1994) 263-267.

[107] W. Chen, B. Zhang, M.J. Forrestal, Exp. Mech. 39 (1999) 81-85.

[108] O. Sawas, N.S. Brar, R.A. Brockman, Exp. Mech. 38 (1998) 204-210.

[109] J.M. Lifshitz, H. Leber, International Journal of Impact Engineering 15 (1994) 723-733.

[110] G. Gary, J.R. Klepaczko, H. Zhao, Proceedings of the International Symposium of Impact Engineering (1992) 73-78.

[111] B. Song, W. Chen, Journal of Engineering Materials and Technology 125 (2003) 294-301.

[112] W. Chen, F. Lu, B. Zhou, Exp. Mech. 40 (2000) 1-6.

[113] K.-. Hartmann, H.-. Kunze, L.W. Meyer, in: M.A. Meyers, L.E. Murr (Eds.), Shock-Wave and High-Strain-Rate Phenomena in Materials, Marcel Dekker, New York, 1981, pp. 325-335.

[114] L.W. Meyer, S. Manwaring, in: L.E. Murr, K.P. Staudhammer, M.A. Meyers (Eds.), Metallurgical Application of Shock-Wave and High-Strain-Rate Phenomena, Marcel Dekker, New York, 1986, pp. 657-674.

[115] M.A. Meyers, G. Subhash, B.K. Kad, L. Prasad, Mech. Mater. 17 (1994) 175-193.

[116] Y.-. Chen, M.A. Meyers, V.F. Nesterenko, Materials Science and Engineering A: Structural Materials: Properties, Microstructure and Processing A268 (1999) 70-82.

[117] M.A. Meyers, V.F. Nesterenko, J.C. LaSalvia, Q. Xue, Mater. Sci. Eng. A 317 (2001) 204-225.

[118] M.A. Meyers, H. Pak, Acta Metallurgica 34 (1986) 2493-2499.

[119] V.F. Nesterenko, M.A. Meyers, J.C. LaSalvia, M.P. Bondar, Y.J. Chen, Y.L. Lukyanov, Mater. Sci. Eng. A 229 (1997) 23-41.

[120] K.R. Coleman, in: H. Schardin, O. Helwich (Eds.), Proceedings of 4th Int. Kongress Kurzzeitphotographie,Darmstadt, Germany, 1959, pp. 32-39.

[121] S.N. Heavens, J.E. Field, Proceedings of the Royal Society of London Series A-Mathematical Physical and Engineering Sciences 338 (1974) 77-93.

[122] S.M. Walley, J.E. Field, P.H. Pope, N.A. Safford, Philos. Trans. Roy. Soc. A 328 (1989) 1-33.

[123] S.M. Walley, J.E. Field, P.H. Pope, N.A. Safford, Journal De Physique Iii 1 (1991) 1889-1925.

[124] J. Addiss, J. Cai, S. Walley, W. Proud, V.F. Nesterenko, Shock Compression of Condensed Matter-2007 in preparation.

[125] V.F. Nesterenko, A.N. Lazaridi, S.A. Pershin, Fiz Goreniya Vzryva 25 (1989) 154-155.

[126] V.F. Nesterenko, M.P. Bondar, I.V. Ershov, High Pressure Science and Technology-1993 (1994) 1172.

[127] V.F. Nesterenko, M.A. Meyers, H.C. Chen, J.C. LaSalvia, Appl. Phys. Lett. 65 (1994) 3069-3071.

[128] V.F. Nesterenko, M.A. Meyers, H.C. Chen, J.C. LaSalvia, Metallurgical and Materials Transactions A 26 (1995) 2511-2519.

[129] H.C. Chen, J.C. LaSalvia, V.F. Nesterenko, M.A. Meyers, Acta Materialia 46 (1998) 3033-3046.

[130] V.F. Nesterenko, M.A. Meyers, H.C. Chen, Acta Materialia 44 (1996) 2017-2026.

[131] Q. Xue, M.A. Meyers, V.F. Nesterenko, Acta Materialia 50 (2002) 575-596.

[132] V.F. Nesterenko, M.A. Meyers, T.W. Wright, Acta Materialia 46 (1997) 327-340.

[133] V.F. Nesterenko, Q. Xue, M.A. Meyers, Journal De Physique Iv 10 (2000) 269-274.

[134] Q. Xue, M.A. Meyers, V.F. Nesterenko, Materials Science and Engineering A-Structural Materials Properties Microstructure and Processing 384 (2004) 35-46.

[135] M.A. Meyers, B.Y. Cao, V.F. Nesterenko, D.J. Benson, Y.B. Xu, Metallurgical and Materials Transactions A 35 (2004) 2575-2586.

[136] Young HD, Freedman RA, Sandin TR, Ford AL. Sears and Zemansky’s university physics. 10th ed. : Addison-Wesley, 2000.

[137] Goldstein J, Newbury DE, Joy DC, Lyman CE, Echlin P, Lifshin E, Sawyer LC, Michael JR. Scanning electron microscopy and X-ray microanalysis. 3rd ed. New York: Springer-Verlag New York, LLC, 2003.

[138] Smith E, Dent G. Modern raman spectroscopy: A practical approach. West Sussex,, England: John Wiley and Sons, 2005.

[139] Brydson JA. Plastics materials. London-Boston: Butterworths, 1989.

[140] J.J. Davis, A.J. Lindfors, P.J. Miller, S. Finnegan, D.L. Woody, 11th International Detonation Symposium 33300-5 (1998) 1007-1013.

[141] W.H. Holt, W.J. Mock, F.J. Santiago, J. Applied. Physics 88 (2000) 5485-5486.

[142] L.J. Parker, H.D. Ladouceur, T.P. Russell, Shock Compression of Condensed Matter-1999 (2000) 941-944.

[143] J.J. Davis, A.J. Lindfors, Shock Compression of Condensed Matter-1997 (1998) 663-666.

[144] D.L. Woody, J.J. Davis, J.S. Deiter, Shock Compression of Condensed Matter-1997 (1998) 667.

[145] F.J. Zerilli, R.W. Armstrong, Shock Compression of Condensed Matter-2001 (2002) 657-664.

[146] A. Khan, H. Zhang, Int. Journal of Plasticity 17 (2001) 1167-1188.

[147] L.E. Fried, W.M. Howard, Shock Compression of Condensed Matter-1999 (2000) 57-60-60.

[148] H.D. Jones, F.J. Zerilli, W.H. Holt, W. Mock Jr., P.J. Miller, A.J. Lindfors, Shock Compression of Condensed Matter-1999 (2000) 137-140.

[149] Gray, G. T. III, Proc. Plasticity ’99-Seventh Int. Symp. On Plasticity and Its Current Applications (1998).

[150] G.I. Kerley, Shock Compression of Condensed Matter-1997 (1998) 671-674.

[151] Y. Gu, V.F. Nesterenko, J. Cai, Shock Compression of Condensed Matter-2003 (2004) 775.

[152] Y.L. Bai, J. Mech. Phys. Solid 30 (1972) 195-207.

[153] N.A. Fleck, W.J. Strong, J.H. Liu, Proc. R. Soc. Lond. A 429 (1990) 459-479.

[154] D.R.E. Lide, editor. 75th ed. : CRC Press, 1995.

[155] K.G. Nakamura, K. Wakabayashi, K. Kondo, AIP Conf. Proc. 20 (2001) 1259.

[156] J.K. Dienes, Mat. Res. Soc. Symp. Proc. 24 (1984) 373.

[157] J. Cai, E.B. Herbold, D.J. Benson, V.F. Nesterenko, Appl. Phys. Lett. in preparation.

[158] T. Sasuga, M. Takehisa, J. Polym. Sci. B 12 (1974) 1889-1898.

[159] M.E. Cates, J.P. Wittmer, J.P. Bouchaud, P. Claudin, Phys. Rev. Lett. 81 (1998) 1841-1844.

[160] K.M. Roessig, J.C. Foster Jr, in: A. Khan, H. Zhao, Y. Yuan (Eds.), Plastic and Viscoplastic Response of Materials and Metal Forming, NEAT Press, , 2000.

[161] J.C. Foster Jr, J.G. Glenn, M. Gunger, AIP Conference Proceedings 505 (2000) 703-706.

[162] K.M. Roessig, J.C. Foster, S.G. Bardenhagen, Exp. Mech. 42 (2002) 329-337.

[163] H.P. Rossmanith, A. Shukla, Acta Mech. 42 (1982) 211-225.

[164] K.M. Roessig, AIP Conference Proceedings 620 (2002) 973-978.

[165] S.G. Bardenhagen, J.U. Brackbill, J. Appl. Phys. 83 (1998) 5732-5740.

[166] X.X. Yao, S. Zajac, Scand J Metall 29 (2000) 101-107.

[167] R.C. Picu, G. Vincze, F. Ozturk, J.J. Gracio, F. Barlat, A.M. Maniatty, Mater. Sci. Eng. A 390 (2005) 334-343.

[168] M.F. Shi, D.J. Meuleman, Journal of Materials Engineering and Performance 4 (1995) 321-333.

[169] F.J. Zerilli, R.W. Armstrong, Journal De Physique. IV : JP 10 (2000) 3-8.

[170] F.J. Zerilli, R.W. Armstrong, J. Appl. Phys. 61 (1987) 1816-1825.

[171] F.J. Zerilli, R.W. Armstrong, J. Appl. Phys. 68 (1990) 1580-1591.

[172] E.N. Brown, P.J. Rae, E.B. Orler, G.T. Gray, D.M. Dattelbaum, Mater. Sci. Eng. C 26 (2006) 1338-1343.

[173] M. Jie, C.Y. Tang, Y.P. Li, C.C. Li, Theoretical and Applied Fracture Mechanics 28 (1998) 165-174.

[174] R. Marissen, Polymer 41 (2000) 1119-1129.

[175] B.N. Sun, C.C. Hsiao, J. Appl. Phys. 57 (1985) 170-174.

[176] I.W. Hall, Metallography 20 (1987) 237-246.

[177] J.W. Kaczmar, K. Pietrzak, W. Wlosinski, J. Mater. Process. Technol. 106 (2000) 58-67.

[178] T. Kuzumaki, O. Ujiie, H. Ichinose, K. Ito, Advanced Engineering Materials 2 (2000) 416-418.

[179] A. Mortensen, I. Jin, International Materials Reviews 37 (1992) 101-128.

[180] A. Feldhoff, E. Pippel, J. Woltersdorf, Advanced Engineering Materials 2 (2000) 471-480.

[181] M. Lancin, C. Marhic, Journal of the European Ceramic Society 20 (2000) 1493-1503.

[182] M.H. Vidal-Setif, M. Lancin, C. Marhic, R. Valle, J.-. Raviart, J.-. Daux, M. Rabinovitch, Mater. Sci. Eng. A 272 (1999) 321-333.

[183] J. Bijwe, R. Rattan, M. Fahim, Tribol. Int. 40 (2007) 844-854.

[184] Y.Z. Wan, Y.L. Wang, H.L. Luo, G.X. Cheng, K.D. Yao, J Appl Polym Sci 75 (2000) 987-993.

[185] P. Soroushian, M. Nagi, A. Okwuegbu, ACI Mater. J. 89 (1992) 491-494.

[186] C.C. Poteet, I.W. Hall, Mater. Sci. Eng. A A222 (1997) 35-44.

[187] Y. Zhou, Y. Wang, S. Jeelani, Y. Xia, Applied Composite Materials 14 (2007) 17-31.

[188] J.A. Cornie, S. Zhang, SPIE Proc. Ser. 5288 (2003) 310-315.

[189] A.Y. Dolgoborodov, M.N. Makhov, I.V. Kolbanev, A.N. Streletskii, V.E. Fortov, Jetp Letters 81 (2005) 311-314.

[190] A.A. Denisaev, A.S. Shteinberg, A.A. Berlin, Doklady Physical Chemistry 414 (2007) 139-142.

[191] D.L. Vezie, W.W. Adams, J. Mater. Sci. Lett. 9 (1990) 883-887.

[192] T. Ohsawa, M. Miwa, M. Kawade, E. Tsushima, J Appl Polym Sci 39 (1990) 1733-1743.

[193] R.L. Salganik, Izvestiya Akademii Nauk, S. S. S. R. , Mekhanika Tverdogo Tela 8 (1973) 149-158.

[194] R.J. O'Connell, B. Budiansky, J. Geophys. Res 79 (1974) 5412-5426.

[195] T. Li, F. Jiang, E.A. Olevsky, K.S. Vecchio, M.A. Meyers, Mater. Sci. Eng. A 443 (2007) 1-15.

[196] Y.X. Zhou, D.Z. Jiang, Y.M. Xia, J. Mater. Sci. 36 (2001) 919-922.

[197] R.T. Pepper, R.A. Penty, J. Composite Mater. 8 (1974) 29-37.

[198] P.W. Jackson, Met. Eng. Q. 9 (1969) 22-30.

[199] S.I. Dement'ev, A.A. Zabolotskii, I.V. Romanovich, S.A. Prokof'ev, S.E. Salibekov, Soviet Powder Metallurgy and Metal Ceramics 16 (1977) 197-200.

[200] Hansen M, Anderko KP. Constitution of binary alloys, Genium Publishing Co., 1989.